A Kinetic Approach to Anomalous Diffusion in Biological Trapping Regions

by

Thomas Matthew Holeva

A Dissertation Presented in Partial Fulfillment
of the Requirement for the Degree
Doctor of Philosophy

Approved November 2014 by the
Graduate Supervisory Committee:

Christian Ringhofer, Co-Chair
Steven Baer, Co-Chair
Sharon Crook
Jesse Taylor
Carl Gardner

ARIZONA STATE UNIVERSITY

December 2014

ABSTRACT

Advances in experimental techniques have allowed for investigation of molecular dynamics at ever smaller temporal and spatial scales. There is currently a varied and growing body of literature which demonstrates the phenomenon of *anomalous diffusion* in physics, engineering, and biology. In particular many diffusive type processes in the cell have been observed to follow a power law $\langle x^2 \rangle \propto t^\alpha$ scaling of the mean square displacement of a particle. This contrasts with the expected linear behavior of particles undergoing normal diffusion. *Anomalous sub-diffusion* ($\alpha < 1$) has been attributed to factors such as cytoplasmic crowding of macromolecules, and trap-like structures in the subcellular environment non-linearly slowing the diffusion of molecules. Compared to normal diffusion, signaling molecules in these constrained spaces can be more concentrated at the source, and more diffuse at longer distances, potentially effecting the signalling dynamics. As diffusion at the cellular scale is a fundamental mechanism of cellular signaling and additionally is an implicit underlying mathematical assumption of many canonical models, a closer look at models of anomalous diffusion is warranted. Approaches in the literature include derivations of fractional differential diffusion equations (FDE) and continuous time random walks (CTRW). However these approaches are typically based on *ad-hoc* assumptions on time- and space- jump distributions. We apply recent developments in asymptotic techniques on collisional kinetic equations to develop a FDE model of sub-diffusion due to trapping regions and investigate the nature of the space/time probability distributions assosiated with trapping regions. This approach both contrasts and compliments the stochastic CTRW approach by positing more physically realistic underlying assumptions on the motion of particles and their interactions with trapping regions, and additionally allowing varying assumptions to be applied individually to the traps and particle kinetics.

i

TABLE OF CONTENTS

LIST OF TABLES

v

LIST OF FIGURES

Chapter 1

INTRODUCTION

The past few decades have seen remarkable advances in imaging and recording technology used to gather biological data on ever more refined temporal and spatial scales. New developments for example in marker fluorescent marker proteins [3] and optical microscocopy techniques [4][5] which push the resolving power of microscopes beyond the classical defraction-limited optics have allowed for the unprecedented resolution of the fine subcellular structures and even dynamic processes that take place in living cells. Nanotechnology which is still in its infancy is certain to usher in still more remarkable experimental advancements in imaging and recording. A sampling of recent work shows the promise: coupling carbon nanotubes to the cell surface [29], 3D real-time, single particle tracking and spectroscopy [30] or 3D high resolution EM tomography [31]. These new technologies are giving us unprecedented views of cellular processes on multiple space-time scales. A recent (2014) tour-de-force of electron and super-resolution flourescent microscopy, mass spectrometry, and quantitative immunoblotting was used to produce the following 3D model of an "average" synapse [6] displaying 300,000 proteins at the level of atomic detail. We reproduce the stunning, daunting and inspirational resulting overview of the complexities of the synapse below with the captions from the paper.

It is evident from the picture that the microstructure of the synapse is highly complex and heterogeneous, interlaced with not only the functional proteins that control release and re-uptake of synaptic vessicles but also a complex network of actin filaments and other cytoskeletal structual proteins. However many of the current standard models and techniques used in mathematical biology are based on averaging
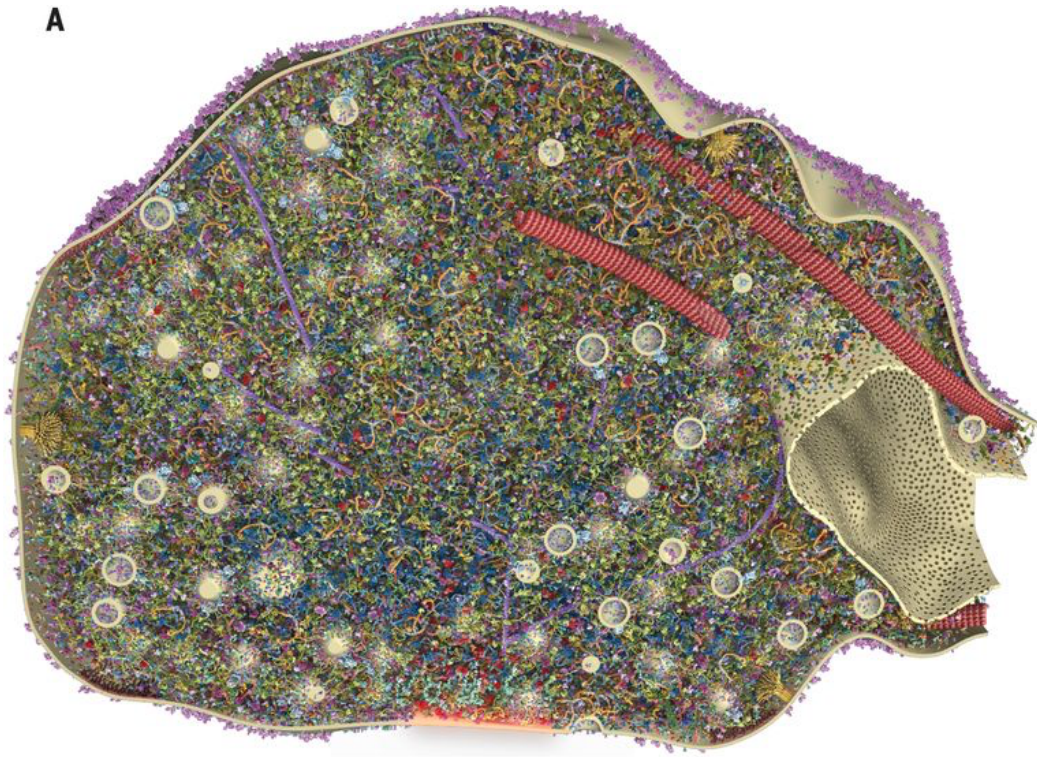
Figure 1.1: A section through the synaptic bouton, indicating 60 proteins.

rules-of-thumb like law of mass action kinetics or the standard diffusion equation which are inherent in the standard formulations of ODE and PDE models.

The new super-resolution data both spatial and temporal that is being generated by these new technologies suggest that many of these classical models may not merely be first-order approximations or reduced models of cellular complexity, but may actually fail to be valid over different space-time scales. This is clearly the case with the anomalous diffusion of molecules in the cell cytoplasm and within the plasm membrane (c.f.Motivations) and also with ultra-low in-vivo concentration (picomolar) kinetics where the concentration profiles may not reproduce the expected law of mass action mechanics which tacitly assumes the reaction rate is proportional to

reactant concentrations [1][2].

$$K = \frac{[S]^\sigma [T]^\tau}{[A]^\alpha [B]^\beta}$$

It is based on the assumption that the reaction rate r_f is proportional to reactant concentrations

$$r_f = k_f [A][B]$$

But this assumption is only true for a statistically large number of reactants and a relatively homogeneous environment, such as the dilute, buffered, aqueous environment of a test tube. Conditions in a living cell are generally far more dynamic, where reactants can become bound to intercellular structures, or the complex non-homogenous nature of the crowded cytoplasm can lead to subdiffusion. [7][8]. There is no current consensus on a suitable replacement for the law of mass action or detailed analysis of its usability and limits in modeling the sub-cellular environment. But recently some work has been done on overcoming the mathematical intractabilities in modeling the types of dynamics often found in biological networks using tools (stochastic Petri nets) developed in computer science: small absolute numbers of molecules which break down the law of mass action but which are simultaneously part of a large network of tens to hundreds of interacting species (which may additionally be operating at various time scales) which break the analyticity of coupled sets of stochastic equations beyond the trivial case of few interacting species. [12]

While it may be possible to salvage these classical workhorses for modeling outside their valid space and time domains such as by using *effective* diffusion constants tied to a particular time-scale in the case of the plasma membrane or introducing non-linear time-varying diffusion terms, we can also ask what other mathematical tools are available which directly address the multi-scale nature of the phenomena in question.

1.1 Motivations from Biology and Proposal of the Boltzmann Kinetic Trap Model

Biological diffusivity within the cytoplasm of cells both upon and across their membranes is an very active area of research in cell biology and biophysics. There have been stunning developments achieved within the last few years in microscopic imaging and recording techniques [35][30][36] allowing for ever increasing resolution and accuracy in both time and space of protein mobility measurements which in turn are leading to a new understanding of the behavior of molecules in structures such as the lipid bi-layer. [26][27][28]

The geometry of the cellular interior is extremely complex, heterogeneous and highly compartmentalized, filled with networks of microtubules, large and small organelles, and internal osmotic membranes which are in a state of constant dynamic rearrangement. Indeed structures such as the plasma membrane can be classified as quasi-liquid like structures comprised of numerous molecules with varying miscibility dynamically forming transient protein complexes. [37] Since the motion of a diffusing particle is highly dependent on the geometric complexity of its environment, and diffusion and molecular interactions often take place along the complex surfaces of the cellular membranes [38], a more careful look at the diffusion equations used in building models of these spaces is warranted. In particular the direct and early motivation for this current research was two papers. In [32] the authors measure the diffusion of a fluorescently labeled dextran tracer molecule through the cytoplasm of HeLa cells. The measured mean square displacements show the power law $\langle x^2 \rangle \propto t^\alpha$ with $\alpha < 1$ which is a hallmark of subdiffusion. The authors suggest that the rates of subdiffusion could be used as a means of gauging macromolecular crowding in the cytoplasmic environment.

In [33] fluorescence imaging within the heavily branched dendritic arbors of Purk-

inje cells showed a remarkable reduction in diffusion rates compared to smooth dendrites. The authors' Monte Carlo simulations suggest that the trapping regions of the spines cause the anomalous diffusion. IP_3, a synaptic second messenger molecule, was strongly influenced while the rapid removal of Ca^{2+} prevented trapping and limited its diffusion. The authors suggest that one regulatory function of dendritic spines may be to trap chemical messengers and thereby slow diffusion of messenger molecules in the dendrites.

1.1.1 Motivation for the Kinetic Trap Model

The literature on anomalous diffusion, even limiting the scope to examples found in biological sciences, is very wide incorporating approaches and techniques from various branches of mathematics and statistical physics. The models in the literature can usually be classified into three broad categories: continuous time random walk (CTRW) approaches, stochastic ODE approaches, and fractional DEs. Although we note that the literature is rapidly developing. The thrust of many of the theoretically oriented papers is to derive expressions for anomalous diffusion through one of the above means, connect the approaches, or expand the basic developments to more general cases. Common to all these approaches is an underlying assumption of the non-Gaussian or non-exponential nature of the space- and time- distributions that drive anomalous diffusion or the built-in assumption of power-law scalings of the fractional differential operators.

Instead we propose a method of obtaining anomalous diffusion that does not rely on ad-hoc assumptions of the underlying nature of the distributions but instead derives the subdiffusive behavior from a more principled statistical mechanical Boltzmann kinetic formulation.

The simple linear Boltzmann equation describes the evolution of the distribution

function of a particle which combines the free transport of the particle with the scattering off a background medium. We briefly outline the presentation in Mellet for the derivation of classical diffusion using the so-called Hilbert expansion method. The linear Boltzmann equation is given as

$$\partial_t f(t,x,v) + v \cdot \nabla_x f(t,x,v) = \int_{v_* \in V} \sigma(t,x,v,v_*)\left[f(v_*)F(v) - f(v)F(v_*)\right] dv_* \quad (1.1)$$

where $x, v \in \mathbb{R}^n$, σ is a bounded, continuous function which is symmetric with respect to v and v_*. The r.h.s. is a linear collision operator which describes a gain and loss term of particles exchanging velocities v_* to v. Assuming that the mean free path of the scattering particles is small compared to the time scale the equation can be rescaled as

$$\epsilon^2 \partial_t f(t,x,v) + \epsilon v \cdot \nabla_x f(t,x,v) = Q(f) \quad (1.2)$$

where ϵ is the ratio of the mean free path length to the macroscopic length and $x \to \epsilon x'$ and $t \to \epsilon^2 t'$

The classic derivation of the diffusion equation follows from the Hilbert expansion in terms of the asymptotic series

$$f = f^0 + \epsilon f^1 + \epsilon^2 f^2 + O(\epsilon^3)$$

Substituting into 1.2 and matching and collecting terms of ϵ we have

$$\epsilon^2 \partial_t(f^0 + \epsilon f^1 + \epsilon^2 f^2 + \ldots) + \epsilon v \cdot \nabla_x(f^0 + \epsilon f^1 + \epsilon^2 f^2 + \ldots) = Q(f^0 + \epsilon f^1 + \epsilon^2 f^2 + \ldots)$$

$$O(1) \qquad\qquad Q(f^0) = 0 \qquad\qquad (1.3)$$

$$O(\epsilon) \qquad\qquad v \cdot \nabla_x(f^0) = Q(f^1) \qquad\qquad (1.4)$$

$$O(\epsilon^2) \qquad\qquad \partial_t f^0 + v \cdot \nabla_x f^1 = Q(f^2) \qquad\qquad (1.5)$$

The first equation simplifies to

$$Q(f^0) = 0 \implies f^0 = \rho(x,t)F(v)$$

since $\ker Q = \rho F(v)$ by definition. Then formally

$$f^1 = Q^{-1}(v \cdot \nabla_x(\rho(x,t)F(v)))$$

Since Q is also a mass-preserving operator we have

$$\int_R Q(f) \, dv = 0$$

for all f. Then integrating out $O(\epsilon^2)$ terms with respect to v and performing the suitible vector gymnastics gives

$$\partial_t \rho + \nabla_x \cdot \int_R v \otimes Q^{-1}(vF(v)) dv \nabla_x \rho$$

where with

$$D = - \int_R v \otimes Q^{-1}(vF(v)) dv$$

we have

$$\partial_t \rho - \nabla_x \cdot D \nabla_x \rho = 0$$

which must have ρ as a solution for the terms f^0, f^1 and f^2 to exist. Also note we assume here that Q^{-1} exists. When $F(v)$ has an algebraic heavy tail such as $F(v) \sim \frac{1}{|v|^{n+\alpha}}$ with $0 < \alpha < 2$ then the diffusion matrix D blows up and this type of asymptotic expansion fails. More delicate expansion methods are needed to derive a diffusion equation from the distributions which lead to anomalous diffusion. We will present the trapping model and MonteCarlo simulations in a later chapter.

1.2   A Case Study

A practical example of how the improving resolution of experimental data is providing new understanding of biological complexity is provided by the paper of Kusumi,

et al. [28] on the diffusivity of molecules in plasma membrane. The plasma (or cell) membrane, the structure of which is essentially the same in all known organisms which have them, consists of a phospholipid bi-layer and embedded molecules such as carbohydrates, glycoproteins and cholesterol, which separate the inside of a cell from the outside environment. Proteins may be associated with either the external layer or internal layers, be integral to the entire bi-layer, or bridge the outside and inside environments such as with ion channels. These proteins may be associated with passive structural functions such as cell-to-cell adhesion or attachment to the internal cytoskeletal scaffolding of microtubules, or with active cell signaling and ion conductivity.

1.2.1   A Thirty Year Enigma

In 1972 S.J. Singer and G. Nicolson [9] proposed the idea of the *fluid mosaic model* where the plasma membrane was considered to be a quasi-liquid, two dimensional bilayer of oriented lipids and proteins, with molecules floating in the bilayer and freely diffusing laterally along the surface of the cell. As this structure is highly dynamic, the model predicts an essentially random distribution of membrane molecules, and consequently bulk properties, e.g. viscosity, for the lipid phase. However, decades of experiments, as summarized in Kusumi et al. on the diffusivity of both lipids and surface proteins in artificially reconstituted membranes and liposomes showed a 5 to 50 times *slower* diffusion constant in real cells compared to artificial membranes. Attempts to explain this by crowding of membrane proteins [39]or the effects of cholesterol on the viscosity of the lipid phase [40] could not account for the drastic reduction in the diffusion coefficient. Secondly it was observed that when receptor molecules and other signaling molecules form oligomers or other molecular complexes, their measured diffusion coefficients dramatically reduced or even became temporarily immobilized [41].

The model of Saffman and Delbrück [42], based on Singer and Nicolson, modeled a transmembrane protein as a cylinder floating in a two-dimensional fluid continuum. The model predicts that translational diffusion should be essentially unaffected by an increase in the size of the diffusant. For instance, assuming a 0.5 nm monomer radius of the transmembrane protein, a monomer-to-tetramer formation which has double the radius of a monomer, predicts a decrease in the diffusion rate by a factor of 1.1. Similarly the formation of a much larger complex such as a 100mer, which has 10 times the radius of a monomer, predicts a decrease in the diffusion rate only by a factor of 1.4. It was found, however [39] that the Saffman-Delbrück model held up well for reconstituted bacteriorhodopsin membranes. Therefore, the drastic drop in diffusion rate for receptors upon ligation could only be explained in the framework of the Singer model by the formation of very large molecular complexes for which there is upon the time of this writing no experimental evidence.

1.2.2   The Resolution of the Enigma with Improvements in Measurement

Early methods of tracking the diffusion rate of membrane proteins relied on FRAP, fluorescence recovery after photobleaching, an optical technique which measures the spread of a photo-bleached area. In the technique the lipid bi-layer is labeled with a fluorescent probe, and a small spot is permanently bleached with a laser. As the photobleached lipids diffuse out of the monitoring area, and non-bleached lipids diffuse into the monitoring area, the return of the intensity of fluorescence can be used to calculate the diffusion constant [43][44]. In the late 1980's it became possible to track *individual* molecules through the use of SPT (single particle tracking). Methods of SPT [45] include labeling individual membrane proteins with gold nanoparticles, polystyrene beads, or fluorescent probes. A series of experiments catalogued in Kusumi [28] SPT experiments on lipid molecules by Fujiwara and Murase showed
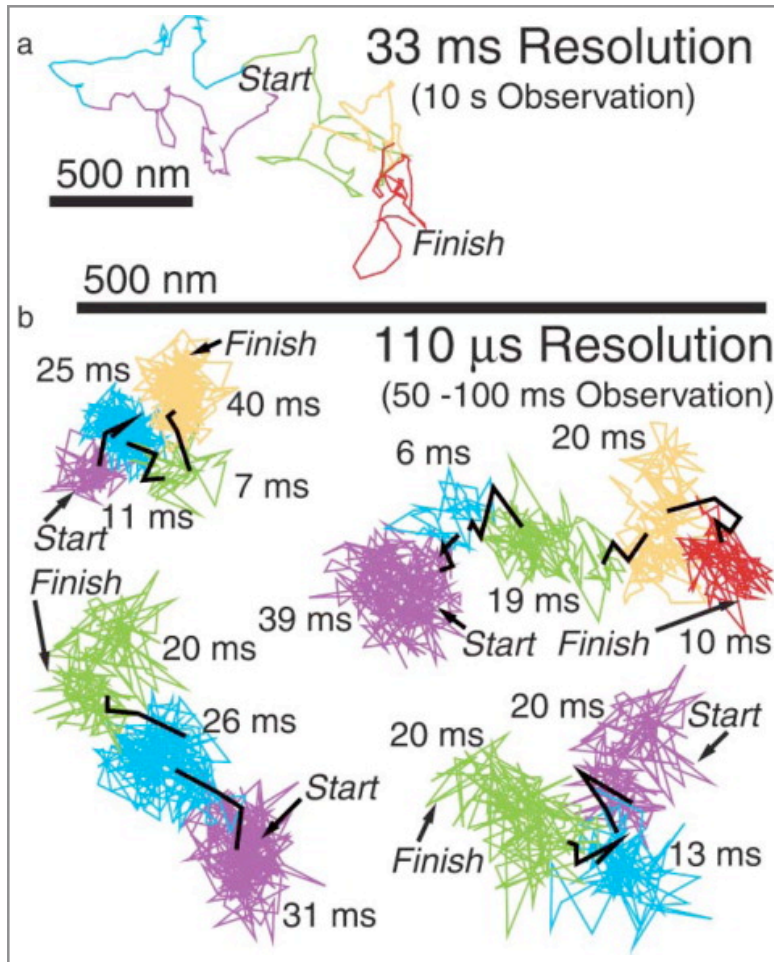
Figure 1.2: Diffusion of L-α-dioleoylphosphatidylethanolamine (DOPE) molecules on two different time scales. a) A protein undergoes apparent Brownian motion on the larger time-scale. However the measured diffusion coefficient disagrees with theory. b) A refined temporal resolution reveals two scales of diffusion, a microdiffusion within cytoskeletal compartments, and a macrodiffusion among the compartments.

that the trajectories of tagged L-α-dioleoylphosphatidylethanolamine(DOPE) lipids in the membrane, on time scales on the order of 30 ms, undergo an apparent unconfined random walk, from which a diffusion rate can be estimated (Fig. 1.2 and following reproduced from [28]). However, on the finer spatial and temporal scales made possible by SPT, on the order of 100 μs resolution, the motion of the particle was seen to undergo a locally confined random walk, followed by a 'hop' or 'jump' into an adjacent area. Analysis of the data suggested that proteins remained locally

trapped in cytoskeletal compartments on the order of 45 nm radius for a mean time of 25 ms. These experiments effectively explained the enigma of both the too slow overall diffusion constant and the slowing of proteins under oligomerization. In the first case, the microscopic (small time scale) diffusion rate of the protein or lipid in the cytoskeletal compartment corresponds to normal diffusion. But the overall 'hop' diffusion of the molecule is anomalous, and in fact sub-diffusive. The diffusion rate varies at different temporal and spatial scales, which contrasts with what is expected from classical diffusion, with its self-similar scales. Secondly, oligomerization reduces the macroscopic (large time scale) diffusion rate by a process called oligomer induced trapping. The effective diffusion rate of the complex is slowed compared to a monomer because all the molecules which form the molecular complex must simultaneously hop the cytoskeleton "fence", which requires larger and longer openings in the inter-compartmental boundaries. Moreover, complexes may become tethered to the cytoskeleton, temporality immobilizing the complex.
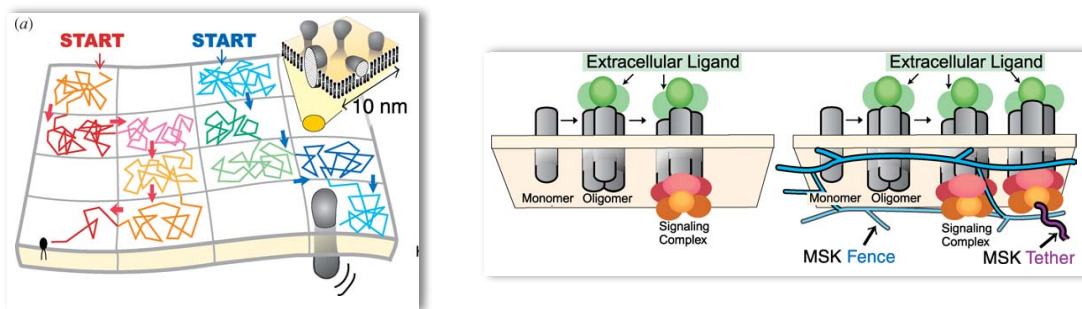
Figure 1.3: a) A schematic of the cytoskeletal compartments showing small scale (intra-compartmental) Brownian motion, and large scale hop-diffusion. b) The cytoskeleton traps oligomerized signaling complexes slowing down the effective diffusion coefficient of the complex.

The above cytoskeletal compartment "fence" model effectively explains a double paradox that puzzled biophysicists for thirty years: an observed 5-50 fold slowdown in the theoretical diffusion rate for the fluid mosaic model, and the reduced diffusion rate of oligomerized molecular complexes in the membrane. Naive extensions of the fluid
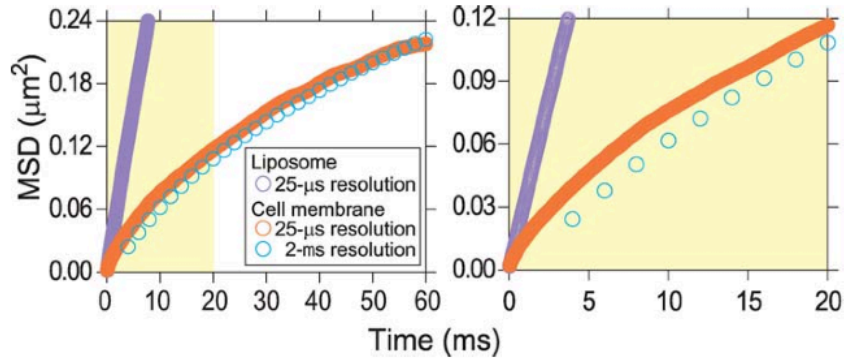
Figure 1.4: Mean squared displacement of the tracked molecule shows the linear mean square displacement $\langle X^2 \rangle \propto t$ of normal diffusion in the artificial membrane (purple) compared to subdiffusive behavior, $\langle X^2 \rangle \propto t^\alpha, \alpha < 1$ of molecules in the cell membrane, (orange, blue).

mosaic model beyond the original spatial scales of the model, approximately 10nm X 10nm, fail. Instead we see a scale-dependent diffusion coefficient which cannot be captured with simple diffusion models. An important closing note is that care must be taken in using previous published diffusion rates measured by techniques using larger time scales such as with video cameras. As molecules in the membrane do not undergo normal diffusion, published rates must be considered to be the *effective* diffusion rates, and membrane molecules undergo *effective* normal diffusion valid only within a certain space-time scale. Moreover, published diffusion rates may only be useful if the time window of the measurement is specified. [56] Needless the say the wrong diffusion rate (especially a 50x wrong rate) can significantly impact even the qualitative nature of solutions of some model if the diffusion rate is critical to some intrisic temporal scale in the model, the model does not make quasi-linear approximations in time scales or the model is trying to simulate and reproduce the details of experimental data. We next consider some of the mathematical tools which can incorporate in a natural way the power-law behavior of the M.S.D. shown in Fig. 1.4 which is indicative of anomalous subdiffusion.

Chapter 2

A BRIEF INTRODUCTION TO FRACTIONAL CALCULUS

2.1   Introduction

Fractional calculus is at once both a topic of research that has gained much at-
tention in recent decades and also a very old topic in the calculus. Already in 1695
Leibnitz considered the possibility of generalizing differentiation to non-integer order.
In an exchange of letters between L'Hôpital and Leibnitz, Leibnitz ponders the ex-
tention of differentiation to non-integer orders. L'Hôpital inquires about the meaning
of half-order differentiation. Leibnitz replies with the answer

$$d^{1/2}x = x\sqrt{\frac{dx}{x}}$$

and the quip

> "It will lead to a paradox, from which one day useful consequences will
>
> be drawn."

In 1823 N.H. Abel found the first useful consequence when he used fractional
calculus to solve a generalized version of the tautochrome problem which involves
solving the eponymous integral equation for $u(s)$ given by

$$\frac{1}{\Gamma(\alpha)} \int_0^t \frac{u(s)\,ds}{\sqrt{t-s}} = f(t)$$

Indeed this equation can be expressed compactly in terms of fractional integration

$$J^\alpha u(t) = f(t)$$

where

$$u(t) = D^{\alpha} f(t)$$

is the solution and J and D represent respectively the fractional-order integration and differentiation operators which will be properly defined in the next section.

The historical bibliography of fractional calculus in the 19th and early 20th century is extensive with major contributions by the likes of Liouville and Riemann. In more recent times fractional calculus has seen a blossoming of development in both pure and applied developments in a wide variety of fields from financial mathematics, biology, and quantum field theory.[15]

However one of the reasons which perhaps limits the wider adoption of fractional calculus is that fractional-order operators have no clear-cut geometric interpretation compared with the well-known interpretations of the integer order calculus: velocity, acceleration, area under the curve, etc. It has been suggested by Podlubny [16] that the fractional order operators could be interpreted as "shadows on the walls", where the fractional integral is interpreted as a Riemann Stieltjes integral

$$\int_a^b f(x) dg(x)$$

and projected onto coordinate systems involving x, $f(x)$, and $dg(x)$ respectively. In a similar manner fractional operators involving time can be thought of as "shadows of the past" (or future!). These notions capture in some sense the non-local nature of fractional differintegral operators.

2.2 Definitions

In this section we present some of the basic definitions of the fractional calculus. Three in particular seem to have more wide-spread use, the Riemann-Liouville definition which is used in many mathematical texts, the Caputo definition which has

14

applications in applied situations, and the Grünwald - Letnikov definititon which is a discrete form useful for numerical computation.

2.2.1 Naive Definitions

The earliest approaches to defining fractional operators involve generalizing composition of the interger operators to real-valued constructions. For instance Euler generalized the composition of the derivative of a monomial

$$D^a x^n = \frac{n!}{(n-a)!} x^{n-a}$$

where $n, a \in \mathbb{N}$. This definition can be continuously extended to the reals (and indeed to the complex numbers) by replacing the factorial with the gamma function.

$$D^\alpha x^n = \frac{\Gamma(n+1)}{\Gamma(n-\alpha+1)} x^{n-\alpha}$$

where the Gamma function is given by

$$\Gamma(z) = \int_0^\infty e^{-t} t^{z-1} \, dt, \, Re(z) > 0$$

This allows us to compute a fractional derivative of any function which admits a Taylor expansion.

As an example

$$D^{\frac{1}{2}} x = \frac{x^{\frac{1}{2}}}{\Gamma(\frac{1}{2})} = \frac{2\sqrt{x}}{\sqrt{\pi}}$$

and

$$D^{\frac{1}{2}} \sqrt{x} = \frac{\Gamma(\frac{1}{2}+1)}{\Gamma(1)} x^0 = \frac{\sqrt{\pi}}{2}$$

so that

$$D^{\frac{1}{2}} D^{\frac{1}{2}} x = 1$$

as we should hope to expect from the composition of the operators.

Note that in general this fractional derivative is not defined for $x \leq 0$ because of the poles of the gamma function. Similarly fractional derivatives introduce fractional powers of x which may not be defined on for $x \leq 0$ for $x \in \mathbb{R}$.

As a further example we can consider the semi-derivative of the power series expansion of $\sin(x)$.

$$D^{\frac{1}{2}} \sin(x) = D^{\frac{1}{2}} \sum_{k=0}^{\infty} \frac{(-1)^k x^{2k+1}}{(2k+1)!} = \sum_{k=0}^{\infty} \frac{(-1)^k x^{2k+\frac{1}{2}}}{\Gamma\left(2k+\frac{3}{2}\right)} = \frac{2}{\sqrt{\pi}} \sqrt{x} \,_1F_2\left(1; \frac{3}{4}, \frac{5}{4}; -\frac{x^2}{4}\right)$$

Note that this is a power series in terms of powers of $\sqrt{x}$ which quickly approaches $\sin(x + \pi/4)$ and represents a 45 degree phase shift compared to the 90 degree phase shift induced by the first derivative. The overshoot from $\sin(x + \pi/4)$ near zero is a consequence of this particular definition of D^α which is made more apparent in the non-local Riemann-Liousville definition of D^α in the next section which involves a lower-bound which may be taken at an arbitrary base point such as at 0 or $-\infty$.
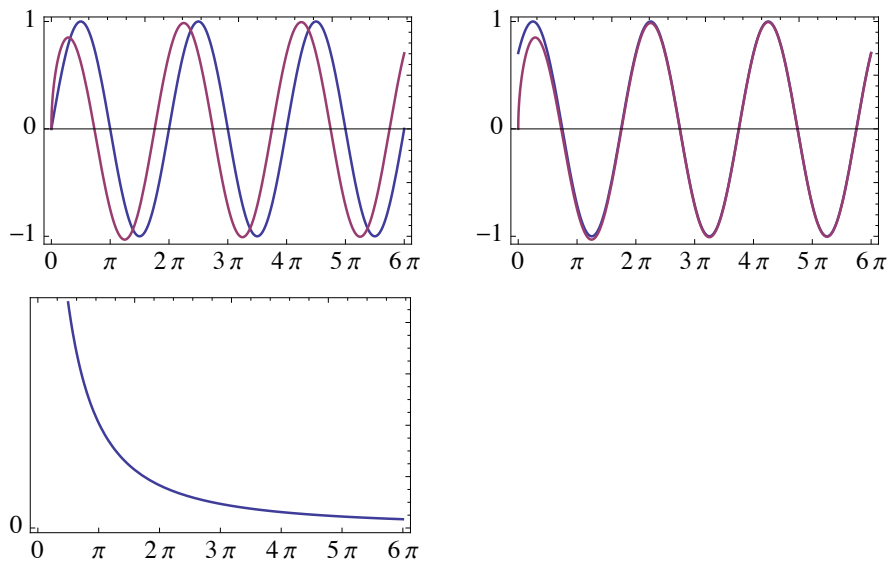
Figure 2.1: (top row):fractional derivative compared to $\sin(x)$ and $\sin(x + \pi/4)$. (bottom row): error: $D^{1/2} \sin(x) - \sin(x + \pi/4)$

A similar construction of the fractional derivative can be based off of repeated
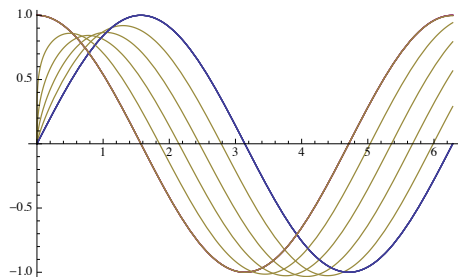
Figure 2.2: Fractional derivatives of $\sin(x)$ with $\alpha = 0.2, 0.4, 0.6, 0.8, 1.0$ where $\alpha = 1$ is $\cos(x)$. This shows the continuous transition from $D^0 \sin(x)$ into $D^1 \sin(x)$

differentiation of the exponential function. This was first done by Liouville.

$$D^\alpha e^{kx} = k^\alpha e^{kx}$$

This definition allows for computing fractional derivatives from any function which admits a Fourier series expansion.

$$D^\alpha f(x) = \sum_{n=0}^\infty c_n k_n^\alpha e^{k_n} x$$

In particular we have $D^\alpha e^{i\theta} = i^\alpha e^{i\theta}$ which can be seen to be a rotation in phase-space. For example for the semi-derivative ($\alpha = \frac{1}{2}$) we have

$$\sqrt{i} = \cos\left(\frac{\pi}{4}\right) + i\sin\left(\frac{\pi}{4}\right)$$

which represents a 45 degree rotation in phase space.

In particular

$$D^{\frac{1}{2}} \sin(x) = D^{\frac{1}{2}}(\frac{1}{2}ie^{-ix} - \frac{1}{2}ie^{ix}) = \frac{(1+i)e^{-ix}}{2\sqrt{2}} + \frac{(1-i)e^{ix}}{2\sqrt{2}} = \sin\left(x + \frac{\pi}{4}\right)$$

In figure 2.3 we compare the semi-derivative of x^3 by computation of terms of 40 terms of its Fourier series and Taylor Series.

2.2.2 Riemann-Liouville Definition

The contributions Riemann and Liouville to the definition of fractional integrals are combined in perhaps the most-used definition of the fraction integral.

17
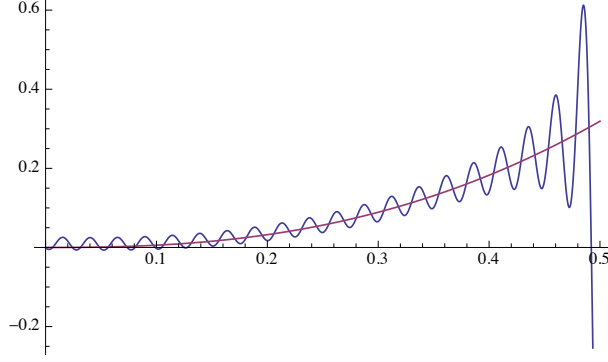
Figure 2.3: $D^{\frac{1}{2}}x^3$ by Fourier (40 terms) and Taylor series

$$_aD_t^{\alpha}f(t) = \frac{1}{\Gamma(n-\alpha)} \left(\frac{d}{dt}\right)^n \int_a^t \frac{f(s)ds}{(t-s)^{\alpha-n+1}} \tag{2.1}$$

where n is an integer chosen such that $n - 1 \leq \alpha < n$. Essentially for a given α the fractional part is calculated via integration and then "pulled back" with integer order derivates to the appropriate value. As an example consider the semi-derivative of $\sin(t)$ calulated with the base $a = 0$ and $a = -\infty$.

$$_0D_t^{\frac{1}{2}}sin(t) = \sqrt{2}\left(C\left(\sqrt{\frac{2}{\pi}}\sqrt{t}\right)\cos(t) + S\left(\sqrt{\frac{2}{\pi}}\sqrt{t}\right)\sin(t)\right) \tag{2.2}$$

$$_{-\infty}D_t^{\frac{1}{2}}sin(t) = \sin\left(t + \frac{\pi}{4}\right) \tag{2.3}$$

Here $C(t)$ and $S(t)$ are the Fresnel cosine and sine integral functions respectively defined as

$$C(t) = \int_0^z \frac{1}{2}dt\left(\left(\pi t^2\right)\cos\right)$$

$$S(t) = \int_0^z \frac{1}{2}dt\left(\left(\pi t^2\right)\sin\right)$$

These expressions are equivalent to the expressions derived in subsection 2.2.1 and demonstrate how the naive approaches based on Taylor expansions and Fourier expanions are tied together by varying the base-point of the RL definition.

18
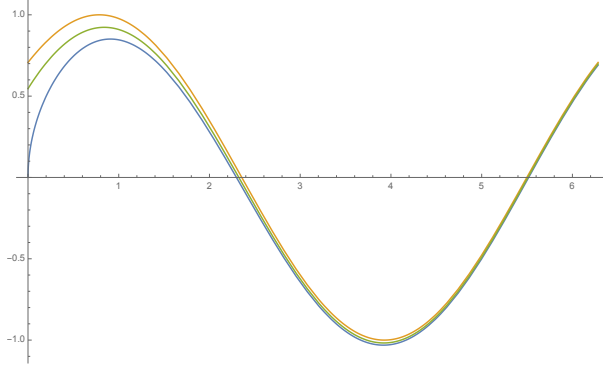
Figure 2.4: RL semi-derivative of $\sin(x)$ with base-point a $= 0$, -1, and $-\infty$

2.2.3 Caputo Definition

The Caputo derivative is a modification to the RL derivative which has the benefit of preserving the property that derivatives of constant functions go to zero. This is a useful property to keep when working with fractional differential equations (FDEs) as the boundary or initial conditions can be specified in terms of standard derivatives with their well-known physical interpretations. Generally speaking the boundary conditions on FDEs may require fractional boundary conditions.

$$
{}_a^C D_t^\alpha f(t) = \frac{1}{\Gamma(n-\alpha)} \int_a^t \frac{f^{(n)}(s)ds}{(t-s)^{\alpha-n+1}}, \qquad n-1 \leq \alpha < n \tag{2.4}
$$

It should be pointed out that because of the inexact inverse relationship between integration and differentiation the RL and Caputo fractional operators are not generally equivalent, but are identical for $\alpha < 0$ with $n = 0$.

2.2.4 Grünwald-Letnikov Definition

The Grünwalk-Letnikov approach starts with the notion of repeated integer-order differentiation and integration defined in the sense of the limit definitions of the derivative and in terms of Riemann sums.

$$\frac{d^n}{dx^n} f(x) = \lim_{h \to 0} \frac{1}{h^n} \sum_{k=0}^{n} (-1)^k \binom{n}{k} f(x - kh) \tag{2.5}$$

$$_a D^{-n} f(x) = \lim_{N \to \infty} \left(\frac{x - a}{N} \right)^n \sum_{k=0}^{N-1} \binom{n + k - 1}{k} f\left(x - k \left(\frac{x - a}{N} \right) \right) \tag{2.6}$$

These are generalized into a fractional-order differintegral operator where again the binomial is continuously extended with the gamma function.

$$_a D^{\alpha} f(x) = \lim_{N \to \infty} \left(\frac{x - a}{N} \right)^{-\alpha} \sum_{k=0}^{N-1} \frac{\Gamma(k - \alpha)}{\Gamma(k + 1)\Gamma(-\alpha)} f\left(x - k \left(\frac{x - a}{N} \right) \right) \tag{2.7}$$
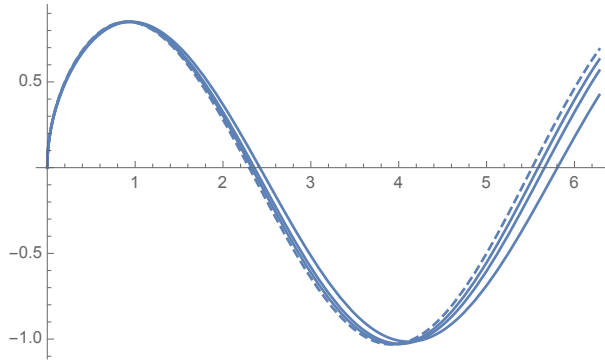
Figure 2.5: GL semi-derivative of $\sin(x)$ with base-point $a = 0$ computed with truncations at $N = 5, 10, 20$. The dashed curved is the RL derivative with base-point $a = 0$ for comparison.

2.2.5 Fractional Differential Equations

We conclude this brief overview of the fractional calculus with an example of a linear fractional differential equation

$$_0 D^{2\alpha} y(t) + k_1 \, _0 D^{\alpha} y(t) + k_2 y(t) = 0, \qquad 0 < \alpha < 1 \tag{2.8}$$

Using the techniques and tables of Laplace transforms found in [17] we proceed by taking the Laplace transform.

$$s^{2\alpha}Y(s) - D^{2\alpha-1}Y(0^+) + k_1 s^\alpha Y(s) - D^{\alpha-1}Y(0^+) + k_2 Y(s) = 0, \qquad 0 < \alpha < 1$$

$$(2.9)$$

Solving for $Y(s)$

$$Y(s)\left[s^{2\alpha} + k_1 s^\alpha Y(s) + k_2 Y(s)\right] = c_1 + a_1 c_2 \tag{2.10}$$

where we have renamed the constants $D^{2\alpha-1}Y(0^+) = c_1$ and $D^{\alpha-1}Y(0^+) = c_2$.

Finally

$$Y(S) = \frac{c_1 + a_1 c_2}{s^{2\alpha} + a_1 s^\alpha + a_2} = \frac{B}{(\lambda - \mu)(s^\alpha + \mu)} - \frac{B}{(\lambda - \mu)(s^\alpha + \lambda)} \tag{2.11}$$

where $B = c_1 + a_1 c_2$ and λ, μ are the roots of the associated polynomial $s^2 + a_1 s + a_2$.

Using the inverse Laplace transform

$$\mathcal{L}\left\{\frac{1}{s^\alpha + k}\right\} = t^{\alpha-1}E_{\alpha,\alpha}(-kt^\alpha)$$

we can write the general solution in terms of the generalized Mittag-Leffler function

$$E_{\alpha,\beta}(z) = \sum_{k=0}^{\infty} \frac{z^k}{\Gamma(k\alpha + \beta)} \tag{2.12}$$

$$y(s) = \left(\frac{B}{\lambda - \mu}\right)\left[t^{\alpha-1}E_{\alpha,\alpha}(-\mu t^\alpha) - t^{\alpha-1}E_{\alpha,\alpha}(-\lambda t^\alpha)\right] \tag{2.13}$$

Next we compute a few particular solutions as examples.

Ex. $a_1 = 0, a_2 = 1; \alpha = 1$

Using the given constants we reduce 2.8 to the ordinary DE

$$y''(t) + y(t) = 0$$

Then utilizing 2.13 we have

$$y(t) = \frac{B}{2i}(E_{1,1}(+it) - E_{1,1}(-it)) \tag{2.14}$$

$$= \frac{B}{2i}(e^{it} - e^{-it}) = B\sin(t) \tag{2.15}$$

as expected.

Ex. $a_1 = 0, a_2 = 1; \alpha = 1/2$

In this case we have the ODE

$$y'(t) + y(t) = 0 \tag{2.16}$$

which has solution

$$y(t) = Ce^{-t} \tag{2.17}$$

From 2.13 we compute

$$y(t) = \frac{i}{2}\left(\frac{E_{\frac{1}{2},\frac{1}{2}}\left(-i\sqrt{t}\right)}{\sqrt{t}} - \frac{E_{\frac{1}{2},\frac{1}{2}}\left(i\sqrt{t}\right)}{\sqrt{t}}\right) \tag{2.18}$$

where $E_{\frac{1}{2},\frac{1}{2}}\left(-i\sqrt{t}\right) - E_{\frac{1}{2},\frac{1}{2}}\left(i\sqrt{t}\right) = 2ie^{-t}\sqrt{t}$ by application of the definition of the Mittag-Leffler function in 2.2.5 and the solution follows.

Ex. $a_2 = 1; \alpha = 1/2$

Next we consider a similar case to the last but with a fractional order derivative which corresponds to

$$y'(t) + a_1 \, _0D^{\frac{1}{2}}y(t) + y(t) = 0 \tag{2.19}$$

which has solution

$$y(t) = \frac{i(a_1 + 1)\left(E_{\frac{1}{2},\frac{1}{2}}\left(\frac{1}{2}\left(a_1 - \sqrt{a_1{}^2 - 4}\right)\sqrt{t}\right) - E_{\frac{1}{2},\frac{1}{2}}\left(\frac{1}{2}\left(a_1 + \sqrt{a_1{}^2 - 4}\right)\sqrt{t}\right)\right)}{2\sqrt{t}}$$

$$\tag{2.20}$$

Notice for $a_1 = 0$ we again recover the solution $y(t) = e^{-t}$. We plot several other solutions for increasing values of a_1 which is the coefficient of the fractional-order derivative in Eq. 2.19
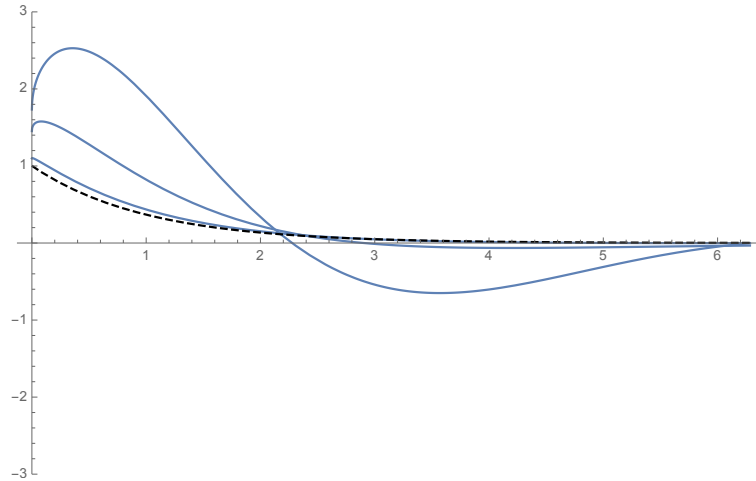
Figure 2.6: The solution of Eq. 2.19 with $a_1 = 0, 0.1, 0.5$ and 1.0

Ex. $a_1 = 0, a_2 = 1$

Lastly we consider the interesting case

$$D^{2\alpha}y(t) + y(t) = 0 \tag{2.21}$$

for general α. In this case when $\alpha = 1$ we recover the simple harmonic oscilator and when $\alpha = 1/2$ we recover the negative exponential. As α varies from $\alpha = 1/2$ to $\alpha = 1$ we have a smooth transition of the solution from $\sin(t)$ to e^{-t} on $(0, \infty)$.

23
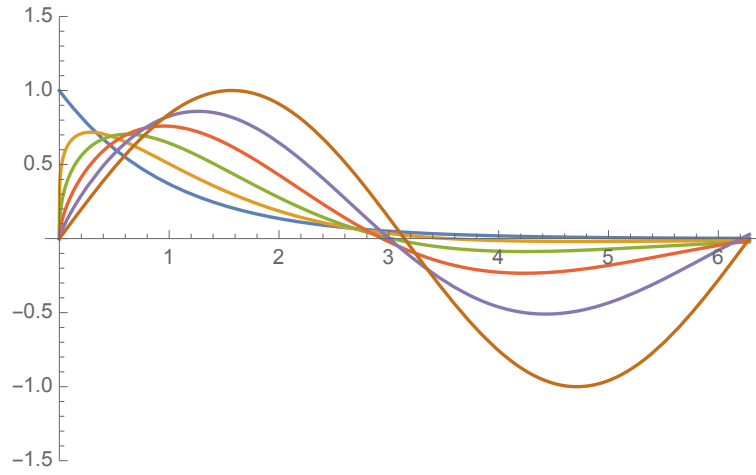
Figure 2.7: The solution of Eq. 2.21 with $\alpha = 0.5, 0.6, 0.7, 0.8, 0.9, 1.0$
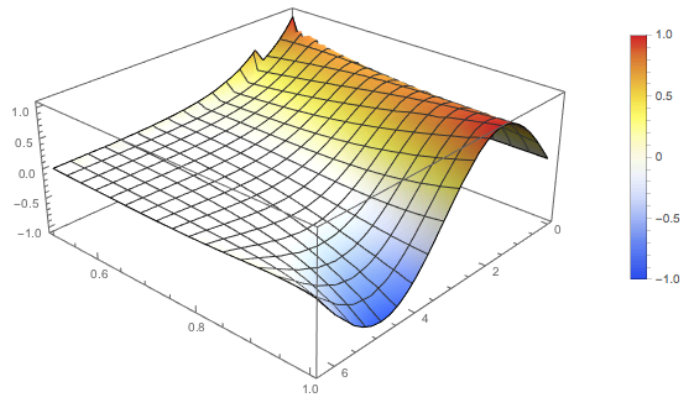
Figure 2.8: The solution of Eq. 2.21 with $0.5 < \alpha < 1.0$ and $0 < t < 2\pi$

Chapter 3

ANOMALOUS DIFFUSION

3.1   Diffusion

The diffusion equation as usually stated,

$$\partial_t U(\mathbf{x}, t) = D\nabla^2 U(\mathbf{x}, t) \tag{3.1}$$

has multiple interpretations stemming from different historical and physical perspectives. For instance we can consider $U(\mathbf{x}, t)$ to be a concentration and D the diffusion constant, or $U(\mathbf{x}, t)$ can be taken as temperature and D as the thermal conductivity. The notion of stochasticity, as we shall see, is also intrinsic in the diffusion equation as it describes the motion of an averaged ensemble of non-interacting particles moving in a fluctuating background. The diffusion equation then can be seen as the time evolution equation of a probability distribution governed by the initial states of the particles. The function $U(\mathbf{x}, t)$ then is a distribution that gives the probability of finding a particle in the neighborhood of $\mathbf{x}$ at time t.

In this section we will consider derivations of the diffusion equation from the macroscopic and microscopic perspectives.

3.1.1   The Phenomenological Perspective: Fick's Law

Diffusion models are an attempt to understand the movement of many individuals, be they bacteria, ions, particles of "heat" or even large objects such as herds or schools of animals, or the spread of epidemics. To that end we assume that the diffusing particles reside within some region $\Omega \in \mathbb{R}^n$ and that $\mathbf{U}(\mathbf{x}, \mathbf{t})$ is the concentration of

25

"particles" at (x, t) Generally speaking the density of particles has an associated scale. For example consider the density of the people in the state of Arizona, non uniformly clustered in the cities. In turn the individual cities have non uniform clustering on the neighborhood scale, and so on. For some point $x \in \Omega$, let $\{\Omega_n\}_{n=1}^{\infty}$ be a nested sequence of subregions containing x, where the Ω_n's are chosen in such a way such that their Lebesgue measure goes to zero. We can then define the concentration as

$$\mathbf{U}(\mathbf{x}, \mathbf{t}) = \lim_{n \to \infty} \frac{\text{count of particles in } \Omega_n}{|\Omega_n|}$$

We will assume that $\mathbf{U}(\mathbf{x}, \mathbf{t})$ is a "nice" function, continuous and differentiable which is not an unreasonable assumption for large collections of particles. The total amount of particles in any subregion Ω_n is given by

$$\int_{\Omega_n} \mathbf{U}(\mathbf{x}, \mathbf{t}) \, dx$$

and the change of particles with time in the same region is given by

$$\frac{d}{dt} \int_{\Omega_n} \mathbf{U}(\mathbf{x}, \mathbf{t}) \, dx$$

Fick's First Law is the phenomenological observation that the movement or flux of heat, ions, etc. goes from regions of high concentration to regions of low concentration, with the magnitude of the flux being proportional to the spatial concentration gradient.

$$\boldsymbol{J} = -D(x)\nabla_x U(x, t) \tag{3.2}$$

where $\boldsymbol{J}$ is the flux and $D(x)$ is the space-varying diffusion coefficient, or *diffusivity*. Although the proportionality function D can depend on such things as temperature, size and charge on the particles, and the viscosity of the medium, we will assume here that it is dependent only on space. Secondly, particles may be generated or annihilated from the region via mechanisms such as birth/death processes, harvesting

of resources, or one-way chemical reactions forming non-reactive species. Then the rate of change of $\mathbf{U}(\mathbf{x}, \mathbf{t})$ due to these mechanisms, called the *reaction rate*, is given by

$$\mathbf{f}(x, t; \mathbf{U})$$

with the total accumulation(or removal) of particles in the region then given by

$$\int_{\Omega_n} \mathbf{f}(x, t; \mathbf{U}) \, dx$$

and the flux across across the boundary of Ω_n

$$\int_{\partial \Omega_n} \boldsymbol{J} \cdot \mathbf{n}(\mathbf{x}) \, dS = \int_{\partial \Omega_n} \nabla \cdot \boldsymbol{J} \, dx$$

where $\mathbf{n}(x)$ is the outward unit normal vector at x and the R.H.S of the equality is by the divergence theorem. Since we assume the system is closed, the change in the population of particles in a region is the sum of the flux across the boundary plus the total change in particles due to the reaction rate.

$$\frac{d}{dt} \int_{\Omega_n} \mathbf{U}(x, t) \, dx = - \int_{\partial \Omega_n} \nabla \cdot \boldsymbol{J} \, dx + \int_{\Omega_n} \mathbf{f}(x, t; \mathbf{U}) \, dx \tag{3.3}$$

If we substitute in (3.2) for the flux term, then for any choice of Ω_n, the following differential equations holds for all values of (x, t).

$$\frac{\partial}{\partial t} \mathbf{U}(x, t) = \nabla \cdot D(x) \nabla_x U(x, t) + \mathbf{f}(x, t; \mathbf{U}) \tag{3.4}$$

which is a reaction-diffusion equation. If we take $D(x) \equiv D$ a constant, and assume that no particles are created or destroyed on Ω, i.e. $f \equiv 0$, the we have the simple *diffusion equation*.

$$\frac{\partial}{\partial t} \mathbf{U}(x, t) = D \nabla^2 \mathbf{U}(x, t) \tag{3.5}$$

This equation of course has been the subject of substantial research.[14] Countless analytical and numerical tools have been developed for the general solution and various classes of boundary value problems. Its well known solution is given by the

27

Gaussian distribution, here shown for one spatial dimension with a constant diffusion coefficient, and with an initial concentration at $x = x'$.

$$u_t(x,t) = Du_{xx}(x,t); \qquad u(x, t = 0) = \delta(x - x') \tag{3.6}$$

$$u(x,t) = \frac{1}{\sqrt{4\pi Dt}} \exp\left(\frac{-|x - x'|^2}{4Dt}\right) \tag{3.7}$$

We can use the solution (the Green's function) to study the statistical ensemble dynamical properties of a particle undergoing diffusion. The mean displacement of the particle is given by

$$\langle x \rangle (t) = \int_{-\infty}^{\infty} \frac{1}{\sqrt{4\pi Dt}} \exp\left(\frac{-|x - x'|^2}{4Dt}\right) x \, dx = x' \tag{3.8}$$

which means, on average, the particle remains at its origin. Computing the second moment, we have

$$\langle x^2 \rangle (t) = \int_{-\infty}^{\infty} \frac{1}{\sqrt{4\pi Dt}} \exp\left(\frac{-|x - x'|^2}{4Dt}\right) x^2 \, dx = 2Dt + |x'|^2 \tag{3.9}$$

with the mean squared displacement then given by

$$\langle x^2 \rangle - \langle x \rangle^2 = 2Dt \tag{3.10}$$

This demonstrates the important relationship which defines or characterizes normal diffusion, linear growth of the mean square displacement in time.

$$\langle x^2 \rangle - \langle x \rangle^2 \propto t \tag{3.11}$$

3.1.2   The Microscopic Perspective: Fokker-Planck

The macroscopic or continuum view of diffusion intuitively describes phenomenological observations such as Fick's Law, but sheds little light on how Gaussian distributions are generated from the underlying random microscopic movement of particles. Einstein, in one of his famous 1905 *Wunderjahr* papers [57], first demonstrated how

a general diffusion equation can be derived from microscopic movements. What follows is a 'master equation' approach based on that derivation. Suppose a particle a position x is impacted by other particles, with a certain energy distribution, such that in a small time increment, Δt, the particle is moved to a new position x' with the probability given as

$$\psi(x, x', \Delta t) \tag{3.12}$$

with

$$\int_\Omega \psi(x, x', \Delta t) \ dx' = 1 \tag{3.13}$$

over the space of all possible jumps Ω. Next consider the probability $p(x, t + \Delta t)$ which is the accumulation of probability density at a point x in time interval Δt.

$$p(x, t + \Delta t) = \int_\Omega p(x - x', t)\psi(x - x', x', \Delta t)dx' \tag{3.14}$$

That is, $p(x, t + \Delta t)$ is equal to the probability that a density at $x - x'$ and time t makes a jump to x in an interval Δt integrated over all possible jumps in Ω. Next, Taylor expanding the left hand side about Δt we have

$$p(x, t + \Delta t) = p(x, t) + \partial_t p(x, t)\Delta t + \mathcal{O}(\Delta t^2) \tag{3.15}$$

Taylor expanding the right hand side about the point $x = x + x'$ we have for the first two terms

$$\int_\Omega p(x - x', t)\psi(x - x', x', \Delta t)dx' \ |_{x=x+x'} = \int_\Omega p(x, t)\psi(x, x', \Delta t)dx' = p(x, t) \tag{3.16}$$

$$\int_\Omega (-x' \cdot \nabla) \left(p(x - x', t)\psi(x - x', x', \Delta t)dx' \right) |_{x=x+x'} = -\nabla \cdot \left(p(x, t) \int_\Omega x'\psi(x, x', \Delta t) \ dx' \right) \tag{3.17}$$

Similarly the third term is given by

$$\nabla \cdot \left[\nabla(p(x, t)) \frac{1}{2} \int_\Omega \psi(x, x', \Delta t)|x'|^2 \ dx' \right] \tag{3.18}$$

Equating the expansions and taking the continuum limit as $\Delta t \to 0$ we find

$$\frac{\partial}{\partial t}p(x,t) = -\nabla \left[p(x,t) \lim_{\Delta t \to 0} \frac{1}{\Delta t} \int_\Omega x' \psi(x,x',\Delta t) \, dx' \right] + \\ \nabla \cdot \left[\nabla p(x,t) \lim_{\Delta t \to 0} \frac{1}{2\Delta t} \int_\Omega |x'|^2 \psi(x,x',\Delta t) \, dx' \right] \tag{3.19}$$

Note this expression contains expressions for the first and second moments of the distribution $\psi(x,x',t)$. We can equate the expression to the mean displacement over a time interval, or the average velocity of the particles.

$$v(x) = \lim_{\Delta t \to 0} \frac{1}{\Delta t} \int_\Omega x' \psi(x,x',\Delta t) \, dx' \tag{3.20}$$

Similarly the second moment measures the variance of the movement of the particles and the following expression defines the diffusion constant

$$D = \lim_{\Delta t \to 0} \frac{1}{2\Delta t} \int_\Omega |x'|^2 \psi(x,x',\Delta t) \, dx' \tag{3.21}$$

The Fokker-Planck equation is then given by

$$\frac{\partial}{\partial t}p(x,t) = -\nabla \left[p(x,t)v(x) \right] + \nabla \cdot \left[D\nabla p(x,t) \right] \tag{3.22}$$

For the situation with zero drift velocity $v(x) = 0$ and a non-spatially varying diffusion coefficient, we recover the diffusion equation from the previous analysis.

$$\frac{\partial}{\partial t}p(x,t) = D\nabla^2 p(x,t) \tag{3.23}$$

3.1.3 Random Walk Approach

As a final approach from the random walk viewpoint we consider a simple one dimensional random walk as laid out in [18] Consider a walk on the discrete spatial steps $\{0, \pm\Delta x, \pm 2\Delta x, \cdots\}$ and similarly let $X(t)$ be a Markov chain on discrete time steps where $t \in \{0, \Delta t, 2\Delta t, \cdots\}$ We define $u(x,t) = Pr\{X(t) = x\}$. Next consider

the probability that a particle may jump either to the left with probability p or the right with probability q in time Δt, where $p + q = 1$.

$$u(x, t + \Delta t) = pu(x - \Delta x, t) + qu(x + \Delta x, t) \tag{3.24}$$

We next expand the right hand side in a Taylor series about Δx to find

$$
\begin{aligned}
u(x, t + \Delta t) = p \left[u(x, t) + \partial_x u(-\Delta x) + \partial_{xx} u(\frac{\Delta x}{2})^2 + O\left(\Delta x^3\right) \right] + \\
q \left[u(x, t) + \partial_x u(\Delta x) + \partial_{xx} u(\frac{\Delta x}{2})^2 + O\left(\Delta x^3\right) \right]
\end{aligned}
\tag{3.25}
$$

Rearranging the terms and dividing by Δt we have

$$\frac{u(x, t + \Delta t) - u(x, t)}{\Delta t} = \frac{(q - p)\partial_x u(x, t)(\Delta x) + (p + q)\partial_{xx} u(x, t)(\frac{\Delta x}{2})^2 + O(\Delta x^3)}{\Delta t} \tag{3.26}$$

For now we will make the following bold assumptions on the limits as $\Delta t \to 0$ and $\Delta x \to 0$.

$$
\begin{aligned}
\lim_{\Delta x, \Delta t \to 0} (q - p)\frac{\Delta x}{\Delta t} &= k \\
\lim_{\Delta x, \Delta t \to 0} \frac{\Delta x^2}{\Delta t} &= D \\
\lim_{\Delta x, \Delta t \to 0} \frac{\Delta x^3}{\Delta t} &= 0
\end{aligned}
\tag{3.27}
$$

The passing to the continuum limit we recover a diffusion equation with a drift term similar to the Smoluchowski equation.

$$\partial_t u(x, t) = k \, \partial_x u(x, t) + \frac{1}{2} D \partial_{xx} u(x, t) \tag{3.28}$$

Returning to the assumptions we made on the limits, consider that we make $\dfrac{t}{\Delta t}$ total time steps on the interval $[0, t]$. The mean displacement of a particle on that time period is then given by

$$\frac{t}{\Delta t} \left(p\Delta x + q(-\Delta x) \right) = t \, (p - q)\frac{\Delta x}{\Delta t} \tag{3.29}$$

31

Similarly the variance in a time period t is given by

$$\frac{t}{\Delta t}\left(p(\Delta x)^2 + q(-\Delta x)^2 - (p-q)^2(\Delta x)^2\right) = 4pqt\frac{(\Delta x)^2}{\Delta t} \qquad (3.30)$$

We see then that we must require the mean and variance to be defined and finite for the previous assumptions to hold. Moreover for $(p-q)\frac{\Delta x}{\Delta t}$ to be finite in the limit as $\Delta t \to 0$, we must require $(p-q)$ to be bounded as $\Delta x \to 0$.

$$\lim_{\Delta x, \Delta t \to 0}(p-q)\Delta x \leq M \lim_{\Delta x \to 0}\Delta x = 0 \qquad (3.31)$$

Finally if $\lim_{\Delta x, \Delta t \to 0}\frac{\Delta x^2}{\Delta t}$ is finite, then $\lim_{\Delta x, \Delta t \to 0}\frac{\Delta x^3}{\Delta t} = \lim_{\Delta x, \Delta t \to 0}\Delta x\left(\frac{\Delta x^2}{\Delta t}\right) = 0$ as required.

Example

As an example consider a symmetric random walk with $p = q = 1/2$. Applying equations (3.27), then the mean displacement μ of a particle is zero, and the variance is $Var(X) = \langle(X-\mu)^2\rangle = \langle X^2\rangle = Dt$. The mean squared displacement $\langle X^2\rangle$ is linear which is indicative of a normal diffusion process, as we saw in the diffusion data from the artificial cell membranes in Section 1.

3.2   Anomalous Diffusion

Normal diffusion as we have seen generally refers to simple Brownian motion and describes phenomena where the mean squared displacement of a diffusing particle is observed to grow linearly with time.

$$\langle x^2\rangle \propto t \qquad (3.32)$$

From the previous Markov chain view of diffusion, it can be seen in essence that this linear growth law depends on the Markov assumption of complete independence

between successive time displacements. Moreover, we also required the mean and variance of the spatial random variable to be defined and finite. *Anomalous* diffusion by comparison describes all other cases where the observed mean squared displacement of a particle, at least over some relevant and interesting time interval, deviates from linearity. An important class of anomalous diffusion is the power-law type growth case.

$$\langle x^2 \rangle \propto t^\alpha \qquad 0 < \alpha < 2 \tag{3.33}$$

Generally, a sub-linear diffusion process ($\alpha < 1$)is called *subdiffusive* while super-linear cases ($\alpha > 1$)are referred to as *super-diffusive*, with the $\alpha = 1$ case recovering normal diffusion. Both phenomenon have been widely observed in a large variety of physical and biological domains. [58] There are two general ways to produce anomalous diffusion, corresponding to relaxing the Markov assumption or the requirement of a defined mean and finite variance. Positive correlations in the temporal or spatial diffusion process, such as by particles being convected along streamlines in turbulent hydrodynamic flows[46] lead to super-diffusion, whereas trapping regions such as the cytoskeletal compartments seen in the introduction lead to anti-correlated motion before the particle escapes into an adjacent compartment, viewed from the perspective of the larger timescale. In contrast to the finite variance distributions of normal diffusion, *infinite* variance in the spatial variable yields wide distributions, or distributions with long tails, from which sudden long jumps may arise. These lead to Lévy flights, such as can be observed in the foraging patterns of bumble bees and deer. [58] (p.463) Similarly if the distribution of escape times from a trapping region has infinite variance, we can have unusually long trapping times leading to subdiffusive behavior. In a sense the particle's overall behavior is dominated by the longest time spent in a trap, in which there is no forward motion. In other words, the system has a 'memory' about the event.

3.3 Models of Anomalous Diffusion

There have been many approaches to anomalous diffusion in the literature [59] Classical non-linear extensions to the canonical diffusion equation lead to special-case analytic results, but these formulations lack generality and have not found wide applicability to physical experiments. In contrast extensions of the above three derivational methods above offer a more general approach which leads to several analytically distinct expressions of anomalous diffusion.

3.3.1 Fractional Diffusion Equations

Extensions of the definition of the derivative to non-integer order, in particular the so-called 'fractional' derivatives can generalize the diffusion equation to the *space-time fractional diffusion* equation

$$_tD_*^\beta u(x,t) = {_xD_\theta^\alpha}u(x,t) \tag{3.34}$$

with $x \in \mathbb{R}, t \in \mathbb{R}^+$ and the real parameters $0 < \alpha \leq 2, \quad 0 < \beta \leq 2, \quad |\theta| \leq \min{(\alpha, 2 - \alpha)}$ where the time-fractional derivative or order β here is given in the Cuputo sense and the space-fractional derivative is of Riesz-Feller type with order α and skewness θ [60]. The essential point of this approach is that we preserve a *linear* fractional differential equation which has a fundamental solution or Green's function for all parameter values. It has been shown in [61] by Mainardi et al. that for a Cauchy problem with $u(x, 0^+) = \delta(x)$, a general solution of the form is given by

$$G_{\alpha,\beta}^\theta(x,t) = t^{-\gamma}G_{\alpha,\beta}^\theta(x/t^\gamma, 1) \quad \gamma = \frac{\alpha}{\beta} \tag{3.35}$$

where G is a spatial probability density function certain parameter ranges of α and β. For instance, in the *time-fractional* symmetric case, as shown in Mainardi [61],

when the skew-parameter $\theta = 0$, $\alpha = 2$, and $0 < \beta \leq 1$ equation (3.35) reduces to

$$G_{2,\beta}^0(x,t) = G_{2,\beta}^0(|x|,t) = \frac{1}{2t^{\beta/2}}M_{\beta/2}(r), \qquad r = |x|/t^{\beta/2} \qquad (3.36)$$

where $M_{\beta/2}(r)$ is a Wright transcendental function given by

$$M_n(z) = \sum_{m=0}^{\infty} \frac{(-z)^m}{m!\Gamma(-nm + (1-n))}$$

For the special case with $\beta = 1$ we recover the normal diffusion equation

$$G_{2,1}^0(x,t) = t^{-\frac{1}{2}}G_{2,1}^0(x/\sqrt{t},1) = \frac{1}{2\sqrt{\pi}}t^{-\frac{1}{2}}\exp^{-x^2/(4t)} \qquad (3.37)$$

Metzler and Klafter [physica A 278] [9-11] analyze the fractional diffusion equation given by

$$\frac{\partial W}{\partial t} = {}_0D_t^{1-\gamma}K_\gamma\frac{\partial^2}{\partial x^2}W(x,t) \quad 0 < \gamma < 1 \qquad (3.38)$$

which describes a non-Markovian diffusion process with a memory. This subdiffusion equation corresponds to a random walk with finite jump length variance, but where the successive jumps in time are drawn from broad waiting time distribution with infinite variance. In this case the fractional derivative operator is the Riemann-Liouville type. The solution of (3.38) in Fourier-Laplace space, with boundary conditions $\lim_{|x|\to\infty} W(x,t) = 0$ and a point-source initial condition $W_0(x) = \delta(x)$ is shown to be

$$W(k,u) = u^{\gamma-1}\frac{1}{u^\gamma + K_\gamma k^2} \qquad (3.39)$$

Taking the limit $\lim_{k\to 0}(\partial^2/\partial k^2)W(k,u)$ and inverting the Laplace transform, the mean squared displacement is recovered, which shows the sub-linear power law dependance on time.

$$\langle x^2 \rangle = \frac{2K_\gamma}{\Gamma(1+\gamma)}t^\gamma \qquad (3.40)$$

Note again, for $\gamma = 1$ we recover the normal diffusion relationship

$$\langle x^2 \rangle = 2K_1 t \qquad (3.41)$$
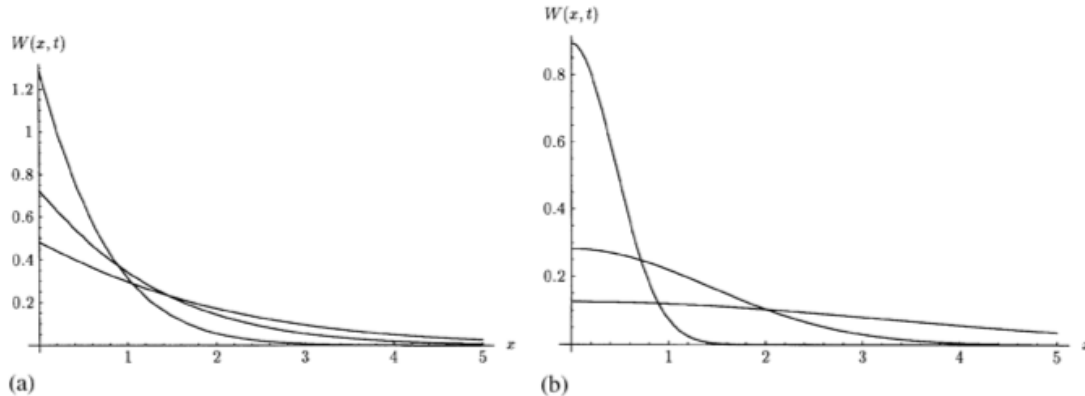
Figure 3.1: (Metzler and Klafter a) The density function $W(x, t)$ is plotted for time $t = 0.1, 1$ and 5. The subdiffusive case ($\gamma = 0.5$) is shown on the left, while the normal diffusive case ($\gamma = 1$) is on the right. Note the slower decay of the tails and the sharp cusp-like behavior near the origin.

where the generalized diffusion coefficient K_1 is a constant.

The fractional calculus is a powerful tool for analyzing the large class of anomalous diffusion phenomena which obey the power-law type scalings $\langle X^2 \rangle \propto t^\alpha$. These FDE equations and the related fractional Fokker-Planck equations can be shown to correspond to the class of α−stable Lévy distributions [47]. Further developments, generalizations and simplifications will undoubtedly lead to a new, practical tool-set in which to model non-Markovian processes with the power and simplicity of linear differential equations.

3.3.2   Generalized Master Equations and CTRW

Following on the discrete random walk approach outlined in Section 3.3, a continuous time random walk (CTRW) allows for the introduction of a waiting time distribution since we no longer restrict our derivation to discrete time steps. Additionally we can introduce more general non-Gaussian jump distributions with finite or even infinite moments. Given a waiting time distribution ψ and a spatial jump distribution η, the probability of locating a particle at (x, t) is given by the Montroll-Weiss

equation. [62]

$$P(x,t) = \delta(x) \int_t^\infty \psi(t')dt' + \int_0^t \psi(t-t') \left[\int_{-\infty}^\infty \eta(x-x')P(x',t')dx' \right] dt' \quad (3.42)$$

The first term of the right hand side describes the contribution to the density P of the number of particles that have *not* moved on the time interval $(0,t)$. The second term describes the contribution to P of the number of particles that have jumped from $x' \to x$ on the time interval $(0,t)$ over the entire space. Introducing Fourier-Laplace transform variables

$$\widehat{\eta}(k) = \int_{-\infty}^\infty e^{ixk}\eta(x)\, dx \qquad \widetilde{\psi}(s) = \int_0^\infty e^{st}\psi(t)\, dt \qquad (3.43)$$

equation (3.42) becomes

$$\widehat{\widetilde{P}}(k,s) = \frac{1 - \widetilde{\psi}(s)}{s} \frac{1}{1 - \widetilde{\psi}(s)\widehat{\eta}(k)} \qquad (3.44)$$

As in earlier analyses, we wish to move to a macroscopic description by passing to the continuum limit. In this case, the limit is taken in the leading order expansion of (3.44) in the large wave-mode limit as $k \to 0$ and in asymptotic time limit as $s \to 0$. The following simplified analysis follows the development in [58]. Taking

$$\psi(t) = \mu e^{-\mu t} \qquad \eta(x) = \frac{1}{\sqrt{2\pi}\sigma} e^{-x^2/(2\sigma^2)} \qquad (3.45)$$

for the waiting time and jump distributions where the mean waiting time is $\langle t \rangle = 1/\mu$ and the mean square jump length is $\langle x^2 \rangle = \sigma^2$, we can recover the standard diffusion equation using standard Fourier-Laplace transform techniques. Taking the small k, small s expansions for ψ and η, we have

$$\widetilde{\psi}(s) = \frac{1}{1 + \frac{s}{\mu}} \simeq 1 - \frac{s}{\mu} + \cdots$$

$$\widehat{\eta}(k) = e^{-\sigma^2 k^2/2} \simeq 1 - \frac{\sigma^2}{2}k^2 + \cdots \qquad (3.46)$$

Substituting into (3.44) we have

$$\widehat{\widetilde{P}}(k,s) = \frac{1}{\mu} \frac{1}{\frac{\sigma^2 k^2}{2}(1 + \frac{s}{\mu}) + \frac{s}{\mu}} \tag{3.47}$$

and then

$$s\widehat{\widetilde{P}}(k,s) - 1 = -\chi k^2 \widehat{\widetilde{P}}(k,s) \tag{3.48}$$

where $\chi \sim \frac{\sigma^2 \mu}{2}$. Inverting the Fourier-Laplace transforms using

$$\mathcal{L}\{\partial_t P\} = s\widetilde{P}(x,s) - P(x,0) \qquad \mathcal{L}\{\partial_{xx} P\} = -k^2 \widehat{P}(k,t) \tag{3.49}$$

we recover the normal diffusion equation for $P(x,0) = \delta(x)$ as claimed. Suppose now we take for ψ and η the following power-law type distributions instead of the previously exponentially decaying PDFs. Indeed as is shown in [47] the PDFs of Levy-stable distributions behave asymptotically as

$$p.d.f._{LS} \sim K|x|^{-(1+\alpha)}$$

where

$$K = \frac{1}{\pi} \sin \frac{\pi \alpha}{2} \Gamma(1 + \alpha)$$

$$\psi(t) \sim t^{-(\beta+1)} \qquad \eta(x) \sim |x|^{-(\alpha+1)} \tag{3.50}$$

Computing the expectations we find that

$$\langle t \rangle = \int_{-\infty}^{\infty} t\psi(t) \, dt = \int_{-\infty}^{\infty} t^{-\beta} \, dt \tag{3.51}$$

diverges for $0 < \beta < 1$ so there is no characteristic time scale for the waiting-times. Similarly for the variance,

$$\langle x^2 \rangle = \int_{-\infty}^{\infty} x^2 \, \eta(x) \, dx = \int_{-\infty}^{\infty} x^2 |x|^{-(\alpha+1)} \, dx \tag{3.52}$$

38

diverges for all $a < 2$. Hence there is no characteristic spatial transport scale. Taking the asymptotic expansions for $k \to 0$, $s \to 0$ we have

$$\widetilde{\psi}(s) \simeq 1 - s^\beta + \cdots$$
$$\widehat{\eta}(k) \simeq 1 - |k|^\alpha + \cdots$$
$$(3.53)$$

and again substituting into (3.44), we have to leading order in s and k^2

$$s^\beta \widehat{\widetilde{P}}(k,s) - 1 = -\chi |k|^\alpha \widehat{\widetilde{P}}(k,s) \tag{3.54}$$

Inverting this relationship with the fractional Fourier-Laplace transforms formally written as

$$\mathcal{L}\{_0D_t^\beta P\} = s^\beta \widetilde{P}(x,s) - s^{\beta-1} P(x,0) \qquad \mathcal{L}\{D_{|x|}^\alpha P\} = -|k|^\alpha \widehat{P}(k,t) \tag{3.55}$$

we may rewrite (3.54) formally as

$$_0D_t^\beta P = \chi D_{|x|}^\alpha P \qquad 0 < \beta < 1 \tag{3.56}$$

This expression is a natural generalization of (3.49) to non-integer order and suggests that the D operators written here formally can be interpreted as suitable integro-differential or the fractional differential operators or the previous section, which indeed can be shown to be the case.

Chapter 4

SIMULATIONS AND INVESTIGATIONS

4.1   Simple Random Walks

As we highlighted in section 3.1.3 we can derive fractional diffusion equations describing anomalous diffusion from random walks using non-Gaussian distributions for space jumps and/or non-exponential waiting time probabilities. In this section we give a method for computing such distributions and several examples of simulated random walks highlighting normal and anomalous diffusion in both one and two dimensions.

Given a sequence $X = (X_1, X_2, X_3, ..)$ of independent identically distributed (i.i.d.) discrete random variables each taking values of either $\{-1 , 1\}$ with probabilities p and $1 - p$ respectively where $0 \leq p \leq 1$, we define the partial sum of the sequence

$$S_n = \sum_{i=1}^{n} X_i \tag{4.1}$$

We call the series $S = \{S_n\}$ so defined a *simple random walk* on the integers in one dimension with parameter value p. Geometrically we can interpret this as a random walker which moves rightward one unit on the $x-$axis with probability p or leftward one unit with probability $1 - p$. It is easy to compute the mean and variance of the process.

$$E(S_n) = \sum_{j=1}^{n} E(X_j) \tag{4.2}$$

$$= \sum_{j=1}^{n} (1)(p) + (-1)(1-p) = 2p - 1 \tag{4.3}$$

$$= n(2p - 1) \tag{4.4}$$

Similarly we have

$$var(S_n) = \sum_{j=1}^{n} E(X_j^2) - E(X_j)^2 \tag{4.5}$$

$$= \sum_{j=1}^{n} nE(1) - n(2p - 1)^2 \tag{4.6}$$

$$= 4np(1 - p) \tag{4.7}$$

For a random walk with $p = 1/2$ which is to say an equal probability of a rightward or leftward step we have the well-known results[48]

$$E(S) = 0 \qquad var(S) = n$$

where $S = \lim_{n \to 0} S_n$ and which holds for the countable sum from the finite additivity property of the expected value. The mean square displacement, which is identical to the variance in this case shows the expected linear growth property proportional to the number of steps taken.

$$< |X|^2 >= n$$

For figure(4.1) we compute $< r^2 >= 1042.61$ where r is the radial distance of a walker to the origin and $< D >$ the mean distance travelled

$$\frac{2}{\sqrt{\pi}} \frac{\frac{\Gamma(n+1)}{2} + \frac{1}{2}}{\frac{\Gamma(n+1)}{2}} \approx 25.23$$

for $n = 1000$.
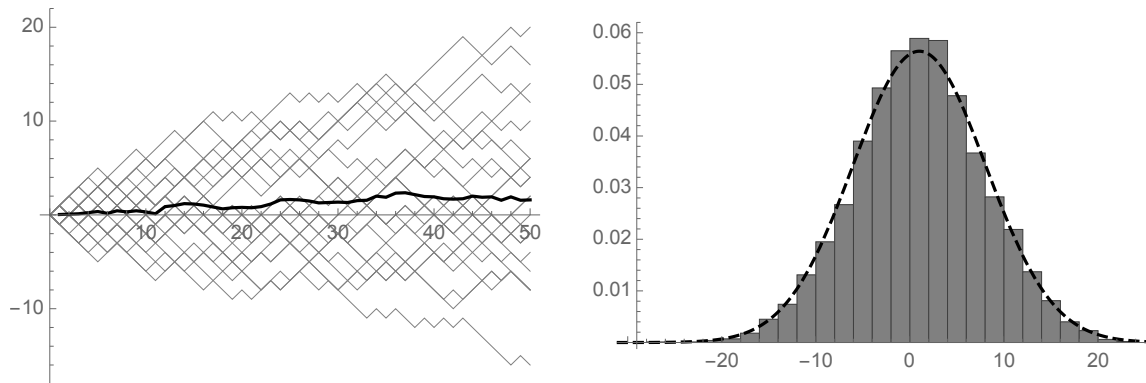
Figure 4.1: Left: 25 simple random walk simulations for $p = 1/2$ and $n = 50$ steps. Dark curve is the computed mean at each n. Right: Histogram of final position of walker after $n = 50$ steps computed from 10,000 simulations. Dashed curve is the theoretical PDF of a normal distribution with $\mu = 0$ and $\sigma = \sqrt{50}$.
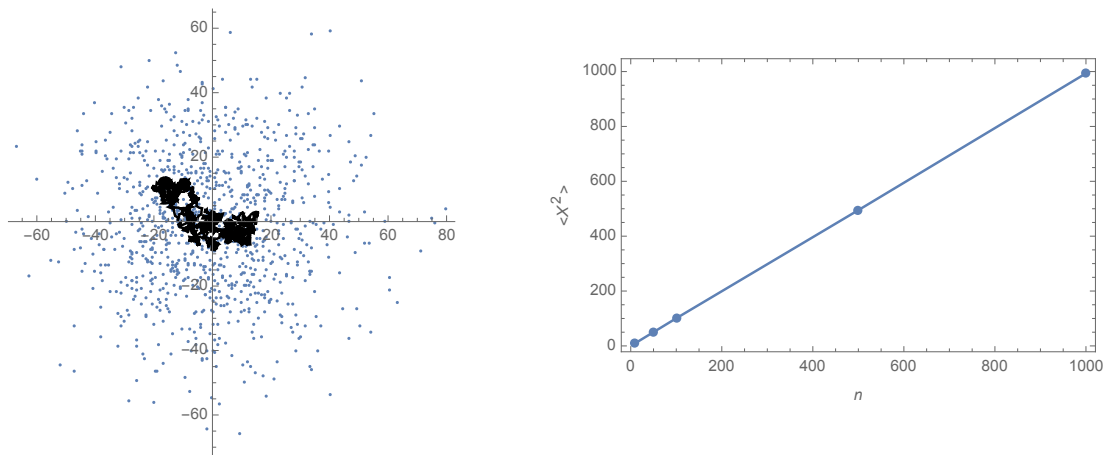
Figure 4.2: Left: The final positions of 1000 walkers after after $n = 1000$ steps. The black line is a typical trajectory of one walker. Each walker moves one unit-step in a uniformly chosen random direction for each step. Right: $< X^2 >$ for 10,000 walkers sampled at $n = 10, 50, 100, 500, 1000$ steps with the expected linear relationship for normal diffusion.

42

4.1.1   Continuous Time Random Walks

As we saw in section 3.3.2 replacing the spatial jump and waiting time distributions in the generalized Master Equation with α-stable Lévy distributions leads to random walks which have quite different characteristics from either discrete or continuous simple random walks previously presented. Instead we find long spatial jumps which give these random walks their characteristic Lévy flights or trapping events which lead to long streches of time where the walker stays at the same location. Similar to our earlier definition of the simple random walk in (4.1) for the continuous time random walk (CTRW), first intoduced by Montroll and Weiss in [49]

we again consider a sequence of independent identically distributed random spatial jumps X_j and additionally a sequence of i.i.d. waiting times T_j and a partial sum defined as,

$$t_n = \sum_{j=1}^{n} T_j, \qquad T_j > 0 \tag{4.8}$$

such that the position of a particle $x(t)$ at time t with $t_n \leq t < t_{n+1}$ is then specified by

$$x(t) = \sum_{j=1}^{n} X_j, \qquad X_j \in \mathbb{R} \tag{4.9}$$

The probability $p(x,t)$ that the process is in position x at time t is given by the Montroll-Weiss equation

$$p(x,t) = \delta(x) \int_t^\infty \psi(t')dt' + \int_0^t \psi(t-t') \left[\int_{-\infty}^\infty \eta(x-x')p(x',t')dx' \right] dt' \tag{4.10}$$

where ψ and η are the waiting time and jump distributions respectively.

One dimensional random walks can be realized by computing the pariticle position from Eq.(4.9) using appropriate distributions. In the case of anomalous diffusion it has been shown[50] that the CTRW leads to a to space-fractional diffusion with the jump probabilities given by the symmetric Lévy $\alpha - stable$ probability distribution often simply referred to as a *stable distribution*. While the stable distributions do not have analytical expressions except in certain special cases the general characteristic function can be expressed as

$$\phi(x; \mu, c, \alpha, \beta) = exp(ix\mu - |cx|^{\alpha}(1 - i\beta sng(x)\Phi)) \qquad (4.11)$$

where

$$\Phi = \tan(\pi\alpha/2) \qquad a \neq 1 \qquad (4.12)$$
$$= -\frac{2}{\pi} \log |t| \qquad a = 1 \qquad (4.13)$$

This distribution is conveniently built into Mathematica 9.0 as the command

$$\text{StableDistribution}[\text{type}, \alpha, \beta, \mu, \sigma]$$

and random samples can be generated with

$$RandomVariate[StableDistributio[\alpha]]$$

as shown in Fig.(4.1.1).

The waiting time probabilty densities can be given by

$$\phi_{\beta}(t) = -\frac{d}{dt}E_{\beta}(-(t/\gamma_t)^{\beta}) \qquad (4.14)$$

where E_{β} is the one-parameter Mittag-Leffler function given by

$$E_{\beta}(z) = \sum_{j=0}^{\infty} \frac{z^j}{\Gamma(\beta j + 1)}, \qquad z \in \mathbb{C}$$

Following the method follows a convenient transformation method given by Chambers[34] which gives the jumps by the following

$$X_\alpha = \left(\gamma_x \frac{-\log u \cos \phi}{\cos((1-\alpha)\phi)} \right)^{1-1/\alpha} \frac{\sin(\alpha\phi)}{\cos \phi} \tag{4.15}$$

where $\phi = \pi(v - 1/2)$ and u, v are independent uniformly distributed random reals on the interval $(0, 1)$ and γ_x is a scale parameter.

The waiting times are given by Kozubowski and Rachev [51]

$$T_\beta = -\gamma_t \log u \left(\frac{\sin(\beta\pi)}{\tan(\beta\pi v)} - \cos(\beta\pi) \right)^{1/\beta} \tag{4.16}$$

where again u, v, are independent uniformly distributed random reals on $(0, 1)$ and γ_t is a scale parameter. When $\beta = 1$ Eq.(4.16) reduces to $\tau_1 = -\gamma_t \log(u)$ which is the inverse CDF of the exponential distribution and hence generates exponential waiting times.

4.2   Subdiffusion

Using the formulations (4.15) and (4.16) we next compute the mean square displacement (MSD) for 1D anomalous diffusion. 1000 particles are simulated for $n = 200$ jumps. The locations of the particles $x(t)$ at time $t = 10, 20, 50, 100$ are found by linear interpolating on the interval $[x(t_n), x(t_{n+1})]$ where $t_n < t < t_{n+1}$. The mean-squared displacement is given by

$$< X^2(t) > = \int_0^\infty x^2 p(x, t) dx = 2dK_\alpha t^\alpha \sim \frac{2dK}{\Gamma(1+\beta)} t^\beta \tag{4.17}$$

where K is a generalized diffusion constant, which we set to $K = 1$ in the simulations.
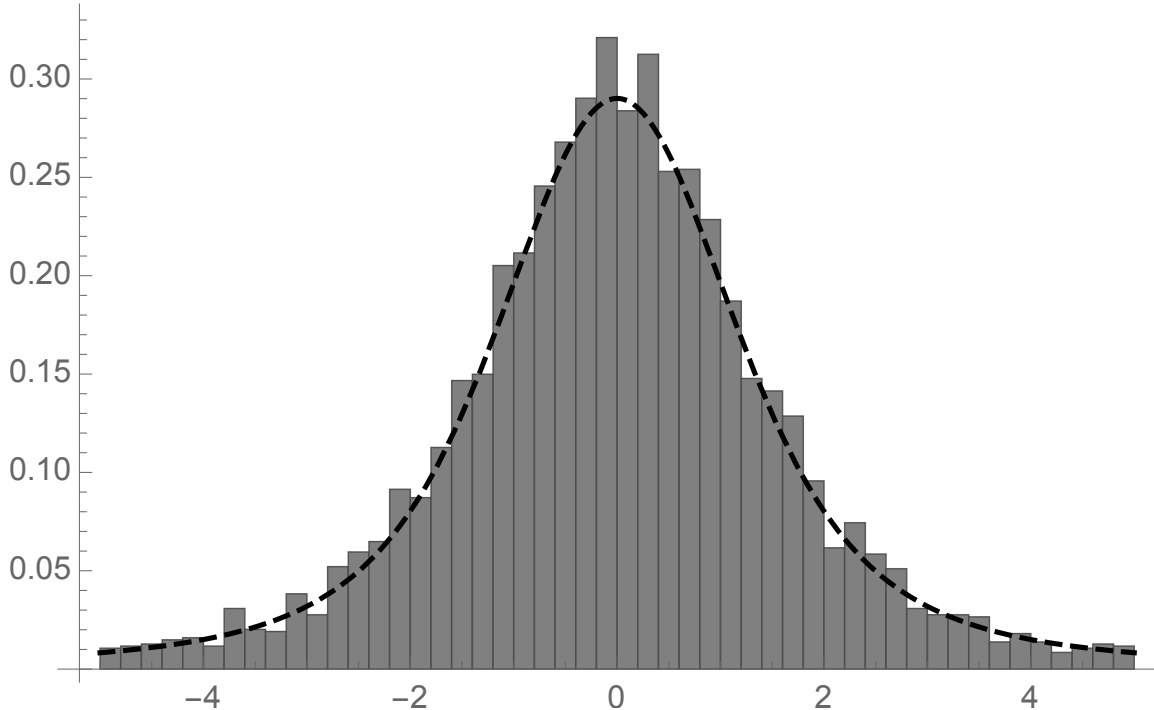
Figure 4.3: 5000 random samples are generated from the formulation given in Eq.(4.15) compared with Mathematica 9.0's built-in stable distribution, dashed line.

4.3   Analysis of Geometrically Simple Traps

As a first step towards building the formalism for a one-dimensional trapping model, let us first consider a (Fig. 4.7) a simple rectangular trap of length L and width W. A particle traveling deterministically enters the trap at location w_0 with incident angle $\alpha \in [-\frac{\pi}{2}, \frac{\pi}{2}]$, with initial velocity v_0, and follows a trajectory determined by simple specular reflection from the walls of the region. In this model the rectangle has three walls from which the particle reflects. When the particle returns to the wall where it entered the trap (w_0) we consider the particle to have then exited and finished its sojourn in the trapping region. We first consider the simple case of a single particle colliding elastically with the boundary. After a certain amount of time spent bouncing in the trap, which we indicate by the *flight time* T, the particle exits the trap with angle α'. It should be noted again in this simple model that the velocity of
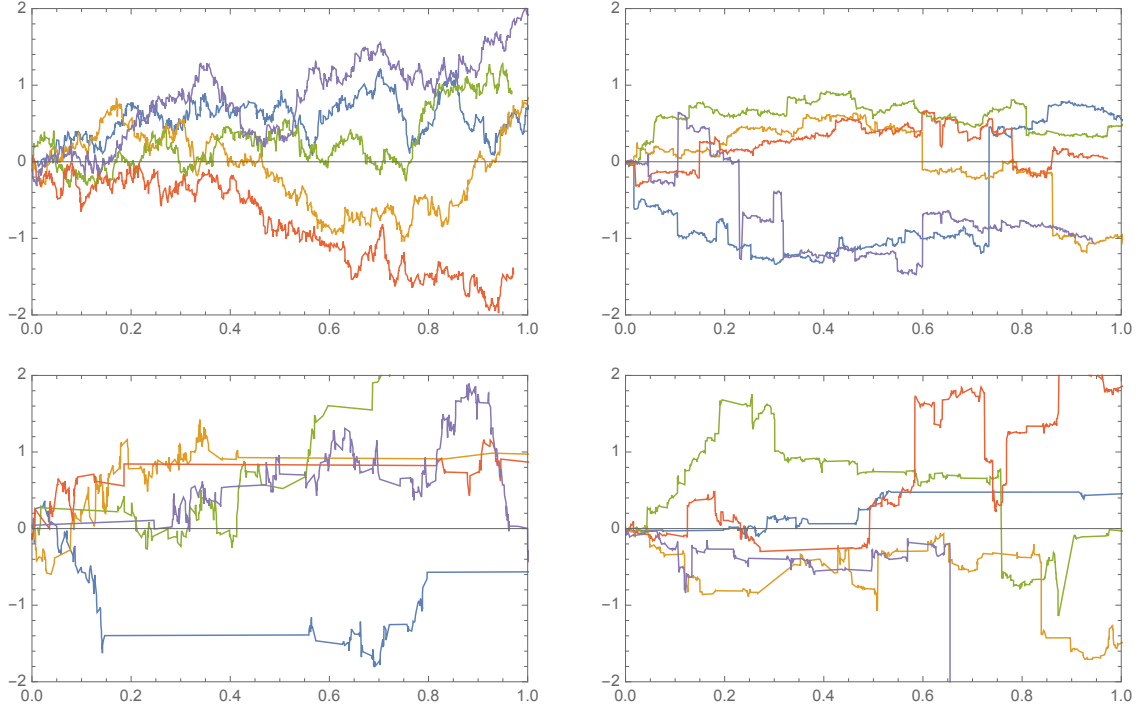
Figure 4.4: 1000 steps of a one-dimensional random walk with Stable Lévy distributions for jumps and waiting times with (clockwise from upper left) parameters (α, β)=(2,1),(1.3,1),(1.3,0.8)(2.0,0.8),. Note the large displacements in x when $\alpha < 2.0$ and the large "trapping" events when $\beta < 1$.

the particle is constant, and we have perfect specular reflection from the boundaries of the trapping region hence no resulting loss of energy to the walls, so we may equate the angles, α and α' with the corresponding velocity vector of the particle entering and exiting the trap. Since the walls of the rectangular trap are mutually orthogonal, it is easy to see from the Law of Reflection that the exit angle α' must equal either $\alpha + \pi$ or $-\alpha$. Moreover because the velocity of the particle is constant, the duration of the particle in the trap, T corresponds to the total distance travelled by the particle.

To analyze the ballistic trajectory of the particle it is helpful to "unfold" the geometry of the trajectory of the particle into a triangle as shown in (Fig. 4.8). It follows that the right triangle that the path of the particle to the far wall $P(\alpha)$ is
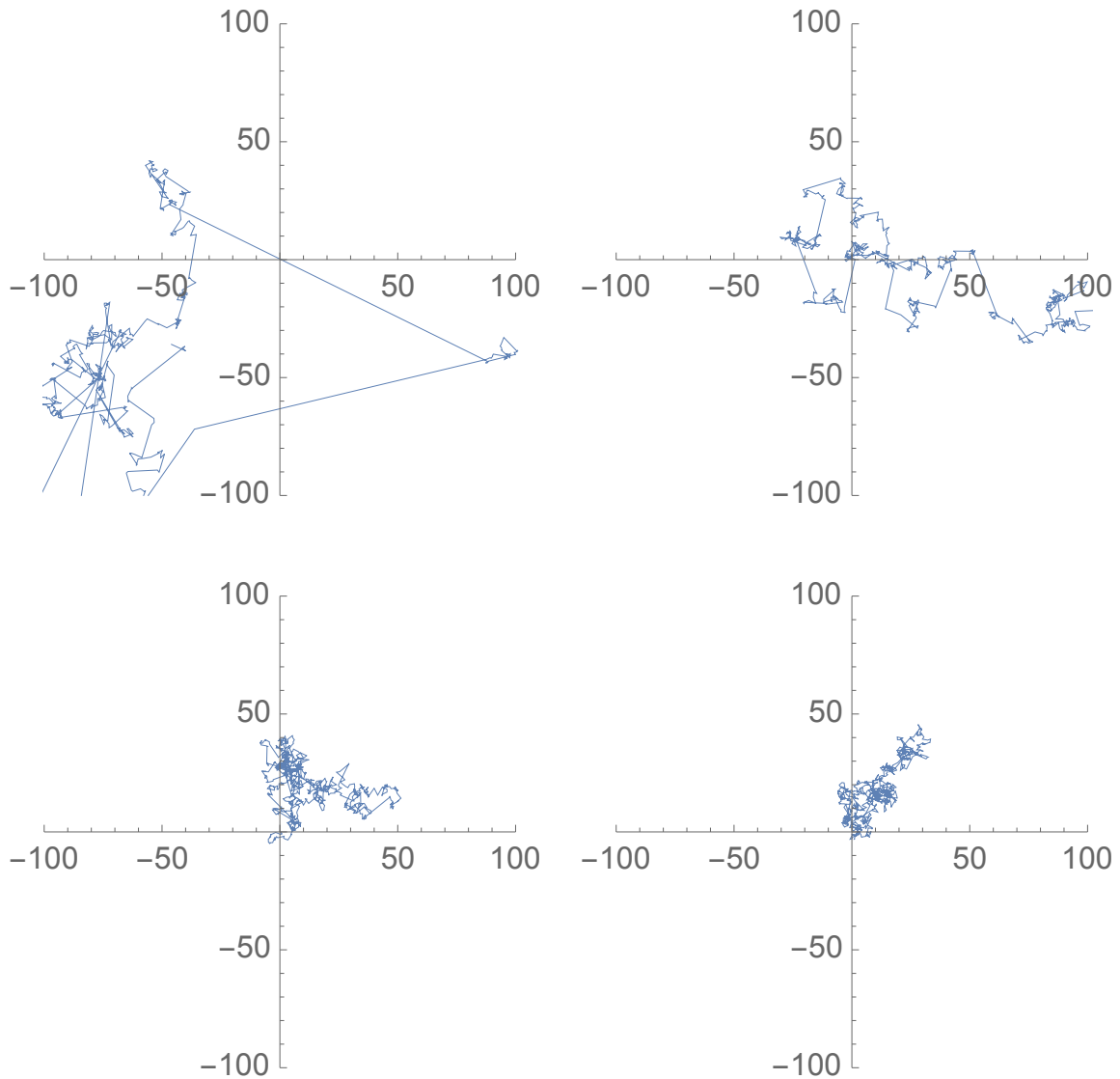
Figure 4.5: 1000 steps of a two dimensional random walk with jump α-stable Lévy distributions with parameter (clockwise)α=(1.3,1.5,1.7,1.9). The long soujourns are typical of superdiffusive Lévy flights. The scale of the graphs have been regularized to more effectively compare the jumps for different values of α.
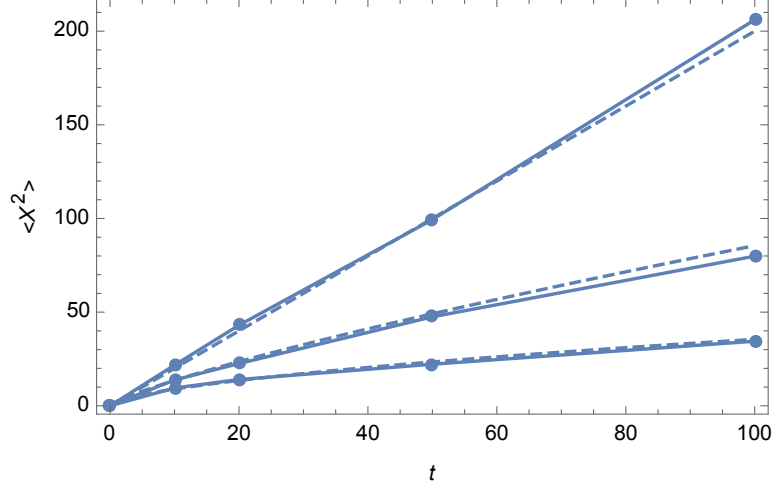
Figure 4.6: Simulations of anomalous subdiffusion with $\beta = 1.0$ (linear case), $\beta = 0.8$, and $\beta = 0.6$. Dashed lines are theothetical MSD for the given parameters.
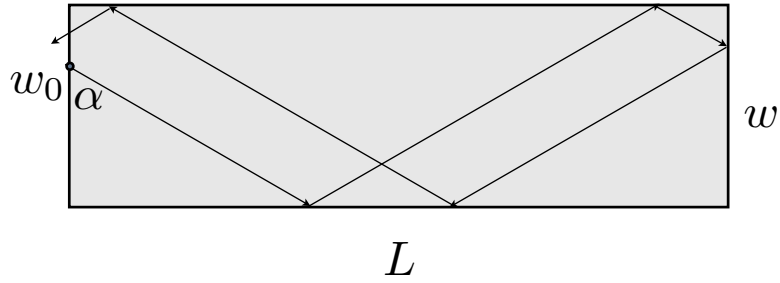
Figure 4.7: A Simple Rectangular Trap with Example Trajectory

given by

$$P(\alpha) = \frac{L}{\cos(\alpha)} \tag{4.18}$$

and the total time duration of the particle in the trap is given by

$$T(\alpha) = \frac{2L}{v_0 \cos(\alpha)} \tag{4.19}$$

where the factor of 2 in the numerator reflects the symmetric path the particle takes from the far wall back to the entrance.

49
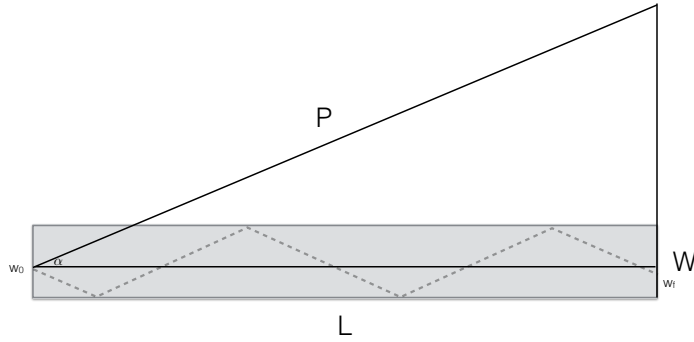
Figure 4.8: The path P corresponds of the trajectory of the particle in the trap.

4.3.1 Analysis of the Rectangular Trap

Because of the symmetry of the rectangle there are only two possible exit angles α' given the entrance angle α,namely the complementary and supplementary angles such that $\alpha + \alpha' = \frac{\pi}{2}$ or $\alpha + \alpha' = \pi$. In the case of the trap orientated horizontally as in (Fig. 4.8) the input angles are on the interval $\alpha = [-\frac{\pi}{2}, \frac{\pi}{2}]$ and the resulting output angles $\alpha' = [\frac{\pi}{2}, \frac{3\pi}{2}]$. A simulation of the simple rectangular trap shows that the input angles are perfectly correlated (Fig. 4.9) with the output angles as expected from the reflection law, although the function $f(\alpha) = \alpha'$ is highly discontinuous with many jump discontinuities arising when a small perturbation in the incident angle causes the trajectory to cross a vertex of the rectangle.

In the case that $\alpha \approx 0$, which corresponds to the particle entering the trap with a velocity primarily orientated in the horizontal direction (relative to the diagram), we see that the duration $T \approx 2L$ and indeed (Eq. 4.3) has a minimum at $\alpha = 0$. As is evident in (Fig. 4.10) for a wide range of α the most frequent times T are within approximately 50 units of time. However as $\alpha \to \pm \frac{\pi}{2}$, then $T(\alpha) \to \infty$ and the
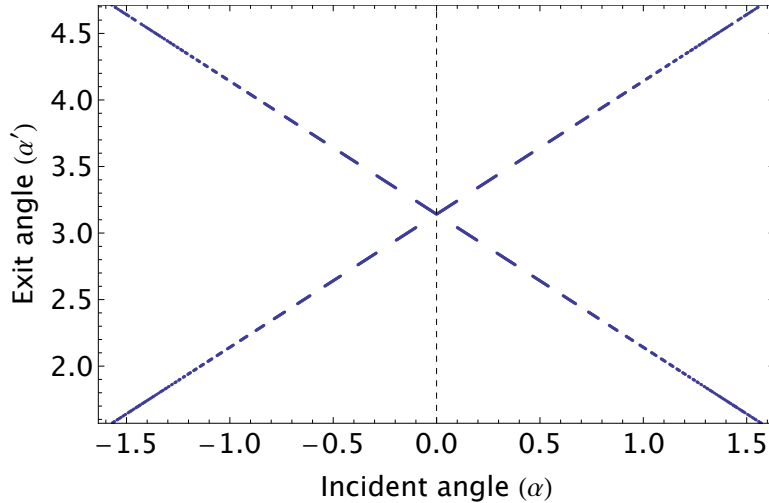
Figure 4.9: The incident angle (α) vs. exit angle (α') is highly correlated, but also highly discontinuous for $n = 1000$ particles.

particle spends a long time in the trap which corresponds geometrically to a particle entering the trap at a grazing angle and bouncing many times before it exits. As we have seen in Chapter Two, it is the behavior of these uncommon but significant long sojourns in the trap that leads to anomalous diffusion and the non-linear behavior of the mean square distance measurement of ensembles of particles.
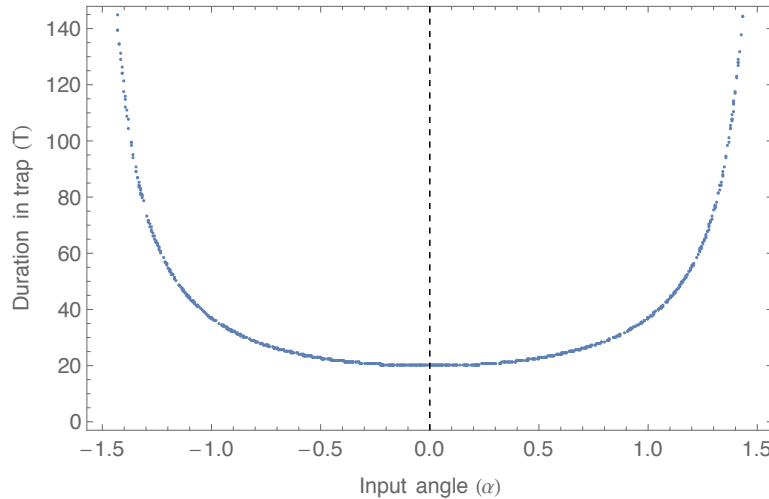
Figure 4.10: The duration of a particle (T) in the trap vs. incident angle (α) for $n = 1000$ particles, $L=10$, $v_0=1$.

4.3.2   Probabilistic Interpretation

Next we consider a probabilistic treatment of the simple rectangular trap. Consider a uniform distribution of the incident angles α with the p.d.f. given by

$$\phi(\alpha) = \begin{cases} \frac{1}{\pi} & \alpha \in [-\frac{\pi}{2}, \frac{\pi}{2}] \\ \\ 0 & \alpha \text{ elsewhere} \end{cases} \tag{4.20}$$

We wish to compute the probability density ψ for flight time of a particle in the trap with a duration of time T given a uniform distribution of angles on $\alpha \in [-\frac{\pi}{2}, \frac{\pi}{2}]$. Then the probability is given by the transformation of the distribution on the angles by

$$T(\alpha) = \frac{L}{v_0 \cos(\alpha)}$$

For a monotonically increasing function g we can compute the p.d.f of the transformed distribution f_Y via the chain rule as

$$f_Y(y) = f_X(g^{-1}(y)) \frac{d}{dy} g^{-1}(y)$$

where g is the transformation function and f_X is the p.d.f. of the distribution to be transformed. Then

$$\psi(T) = \frac{1}{\pi} \frac{d}{dT} \arccos(\frac{L}{Tv_0}) \tag{4.21}$$

$$= \frac{1}{\pi} \frac{1}{Tv_0} \frac{L}{\sqrt{T^2 - \frac{L^2}{v_0^2}}} \tag{4.22}$$

$$= \frac{1}{\pi} \frac{L}{T\sqrt{T^2 v^2 - L^2}}; \qquad T > \frac{L}{v_0} \tag{4.23}$$

In (Fig.4.11) we present a histogram of trap durations for the rectangular trap plotted against (Eq. 4.21). The minimum time in the trap time is $T = 2L/v_0 = 20$. The most striking feature of the distribution is the long tail. Indeed the tail is truncated in the displayed histogram in order to better highlight the shape. Next the CDF of

ψ was calculated and compared to the simulation.

$$CDF(\psi) = \int_{20}^{T} \frac{2 \times 20}{\pi t \sqrt{t^2 - 20^2}} \, dt$$

The results for several values of T are tabulated in (Table 1) along with the data from the simulation. The accumulated percentage is shown in the last column. The heavy-tailed nature of the distribution is made apparent in that 12.7 percent of the particles remained in the trap for longer than $T = 100$ time units.
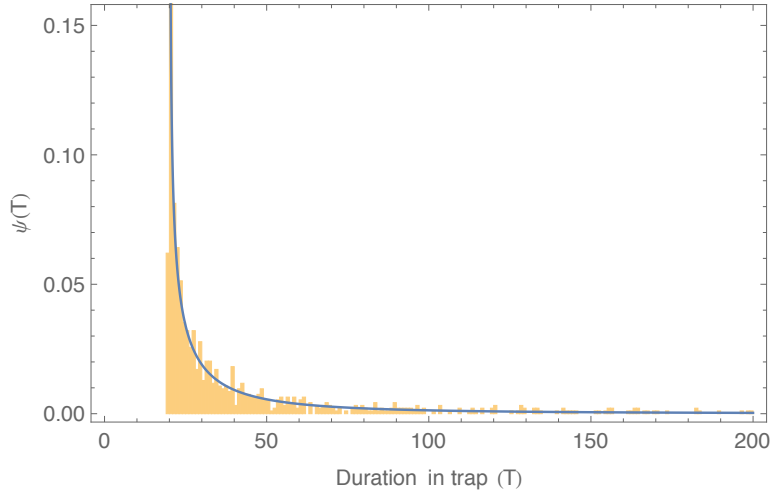
Figure 4.11: Distribution of trap times (T) for $n = 1000$ particles in a $L = 10, v_0 = 1$ trap. Solid curve is the calculated p.d.f $\psi(T)$.

A next reasonable question to ask is what is the mean time a particle with a uniformly random incident angle stays in the channel. Calculating the expected value of the p.d.f. we find

$$E[T] = \int_{L}^{\infty} t\psi(t) \, dt = \lim_{s \to \infty} \int_{L}^{s} \frac{2L}{\pi \sqrt{t^2 - L^2}} \, dt \tag{4.24}$$

$$= \lim_{s \to \infty} -\frac{2L}{\pi} \log\left(\frac{L}{s + \sqrt{-L^2 + s^2}}\right) \tag{4.25}$$

As $s \to \infty$ in (Eq.4.24) clearly the log term blows up and $E[T] \to \infty$. A similar calulation shows the variance is also unbounded which is an important result since

53

T	calculated	simulated	% accumulated
20	0.535441	0.492	49.2
30	0.131226	0.131	62.3
40	0.0713536	0.07	69.3
50	0.0456329	0.04	73.3
60	0.0318852	0.03	76.3
70	0.0236004	0.016	77.9
80	0.0181992	0.019	79.8
90	0.0144737	0.017	81.5
100	0.011792	0.007	82.2

Table 4.1: Percentage of particles remaining in trap for several intervals of T.

this is exactly the condition we require for anomalous diffusion.

$$E[T^2] = \int_L^\infty t^2 \psi(t) \, dt = \lim_{s \to \infty} \int_L^s \frac{2Lt}{\pi\sqrt{t^2 - L^2}} \, dt \tag{4.26}$$

$$= \lim_{T \to \infty} \frac{2L\sqrt{T^2 - L^2}}{\pi} \to \infty \tag{4.27}$$

4.3.3   Cauchy Distribution

The Cauchy distribution is famous for being a "pathological" example of a distribution with undefined moments. Similar to the distribution we calculated in (Eq.4.21) for the time spend in the simple trap, the Cauchy distribution also have infinite first and second moments. If fact we can show that the trap distribution is a transformation of the Cauchy distribution. Consider the Cauchy cumulative density function

$$F_X(x) = \frac{1}{2} + \frac{1}{\pi} \arctan(x) \tag{4.28}$$

and the trapping function

$$\Psi(T) = \frac{1}{\pi} \frac{L}{T\sqrt{T^2 v^2 - L^2}}; \qquad T > \frac{L}{v_0}$$

54

. Then the density functions are defined by

$$f_X(x) = \frac{\partial}{\partial x} F_X(x) = \frac{1}{\pi} \frac{1}{(1 + x^2)}$$

and

$$\psi_T(t) = \frac{\partial}{\partial t} \Psi_T(t) = \frac{1}{\pi} \frac{1}{(1 + s^2)} \frac{d}{dt} s(t); \qquad s = -\frac{1}{\sqrt{t^2 + -1}}$$

Then $\psi_T(t) = g(X)$ where X is the Cauchy distribution and $g(s) = \sqrt{\frac{1}{s^2} + 1}$ is the transformation function.

As a final calculation for the simple trap simulation we compute the numerical mean and variance of the total time in trap T for 10 runs to highlight the effect which the theoretical unbounded mean and variance has on the computer simulations.

run	mean	variance
1	103.845	46000.6
2	101.769	39552.7
3	61.5184	16213.9
4	75.8452	19334.5
5	76.0872	20354.3
6	53.0913	5627.
7	96.267	47157.2
8	53.4665	13444.
9	83.4209	32742.2
10	62.4442	10246.7

4.4   More General Traps

In the simple rectangular trap of the previous section we saw that even a very simple geometry is enough to generate probability distributions with unbounded vari-

ance in the trapping time. But we had the somewhat overly symmetric result that the incident angle α was highly correlated with the exit angle α'. Unfortunately for geometries more complex than one-dimenional dynamical maps, regular polygons and circles, the dynamics of the trapping region, although still deterministic, can become weakly chaotic and difficult to approach analytically. However simulations of arbitrary complex trapping regions may be carried out limited only by time constrains, computer power and of course the sophistication of the simulation. A more general simulation program was developed to carry out an investigation of more elaborate geometrical set-ups.

4.4.1   Rectangular Trap with Pore

First we consider a modification of the rectangular trap with a small hole or pore of width p placed symmetrically along the bottom wall. This increases the surfaces a particle in the trap may reflect from from 3 walls to 5. As we will see this complicates the possible trajectories and drastically effects the nature of the waiting time distribution from the simple u-shaped distribution in (Fig. 4.10). We "unfold" the geometry of the trap in a similar manner of the previous analysis so that trajectories in the trap follow straight lines. (Fig. 4.12).The trap walls are the solid dark lines in the lower left hand quandrant of the diagram, and a sample trajectory in the trap is shown in a dashed line. The unfolded trajectory is the long dashed line. The pore of the trap p is indicated by a dark line segment and the reflections of the pore are indicated on the diagram.

A particle in the trap will exit when the unfolded trajectory hits a reflection of the pore which are located at heights of $\pm 2Ln$, $n \in \mathbb{Z}^+$ in the unfolded geometry. We are interested first in knowning the critical angles for which an incident velocity vector will exit the trap. These are indicated on the diagram as thin gray lines. For instance

56
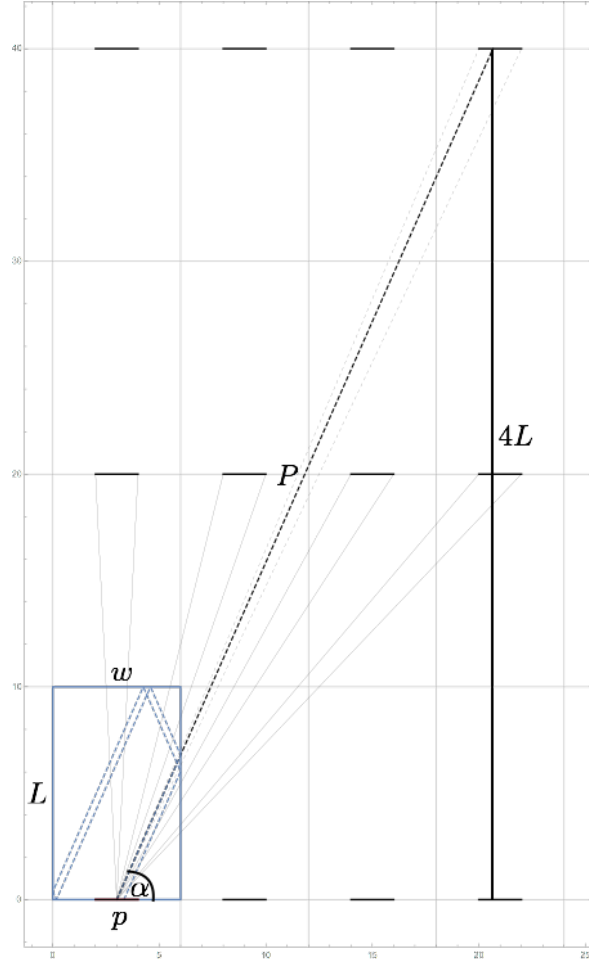
Figure 4.12: Pore Trap. A trajectory with incident angle α follows the dashed curve in the trap, and the straight dashed curve on the unfolded geometry. The particle exits the trap when the unfolded trajectory hits a reflection of the pore (dark segments).

the unfolded trajectory in the diagram hit a trap wall at a height of $4L$ and the time spent in the trap is therefore equal to the length of the path P over the velocity v. This is the geometric situation which causes the trap time function $\tau(\alpha)$ to be highly discontinuous. If the trajectory shown in the diagram were to shift out of the critical angles the particle would continue on to the next level of the schema. The critical angles are then effectively indexed by the vertical and horizontal reflections of the pore, namely the $2Lj$ heights of the trap with $j = 1, 2, 3, ...$ and also the horizontal shift of the width wi with $i \in \mathbb{Z}$. For a particle located at some fraction s of the pore

width p we can compute the critical angles from the right-triangle geometry of the unfolded path. Namely we have for $i \in \mathbb{Z}$ (the symmetric case for angles $\alpha > \pi/2$ is not shown) and $j = 1, 2, 3, \ldots$ the right and left bounds on the entrance angle.

$$\theta_{(i,j)} < \alpha < \Theta_{(i,j)}$$

$$\theta_{(i,j)} = \tan^{-1}\left(\frac{2Lj}{sp + iw}\right)$$

$$\Theta_{(i,j)} = \tan^{-1}\left(\frac{2Lj}{sp - p + iw}\right)$$
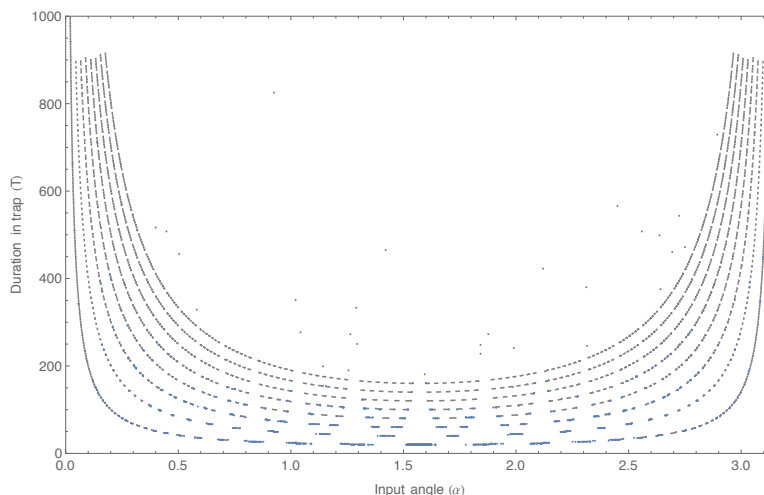
Figure 4.13: Pore Trap showing the discrete trapping times $2Ln$

Fig (4.13) shows the simulation data plotted again the theoretical possible waiting times calculated from:

$$T(\alpha) = \frac{L}{v_0 \cos(\alpha)}$$

In closing we note that not all indices of (i, j) represent a possible exit pore. For instance in the vertical strip $(0, j)$ the traps at heights $4L, 6L, \ldots$ cannot be reached because any angle in those critical angles such as $\alpha = \pi/2$ will always exit the trap at $2L$. For a particle entering the trap exactly in the center of the pore (the symmetric

58

case) this reduces to only the traps at index $i \mod j \neq 0$ being reachable. That is to say all traps are reachible on the $2L$ level, every second trap on the $4L$ is unreachable, every third trap is unreachable at $6L$, etc. This geometry then stratifies the trapping times into discrete quanta $2Ln$ for $n = 1, 2, 3, ...$ shown in (Fig. 4.13) and tends to remove the middle portion of the "U" from the actual trapping times. Since which traps are reachable is also a complicated function of the horizontal location the particle enters the trap (sp) we did not consider refining the possible trapping angle functions $\theta_{(i,j)}$ to account for the computed distributions exactly.

Finally we calculate the histogram for the pore trap in (Fig. 4.14) to demonstrate the presence of a long tail. Note the histogram bar on the far right of the simulation. Since this simple simulation had a short maximum step time trajectories that never exited the trap in under $T < 2000$ were counted as $T = 2000$. It turns out this was a useful way to easily notice the long-tails in testing various simulation scenarios because the presense of a relatively large histogram bar represents the accumulation of all trap times *over* a given threshold. That is to say it represents the sum of the long tail. Finally we plotted $T(\alpha)$ for various pore sizes in (Fig. 4.15). As expected the smaller pore size makes it more difficult for a particle to escape so the density of $2L$ waiting times at the bottom of the "U" are less possible. Notice that density of high T times represented by the sides of "U" are fairly dense across all pore sizes so incident angles at the extremes, the horizontal grazers entering the trap, will almost certainly tend to stay in the trap for a long time.

4.4.2   T-Shaped Trap

Perhaps the next most complex trap to consider is a T-shaped trap consisting of two overlapping rectangles. Several example trajectories are highlighted in in (Fig. 4.16) and data is collected from a run of $n = 10,000$ particles. It is immedi-
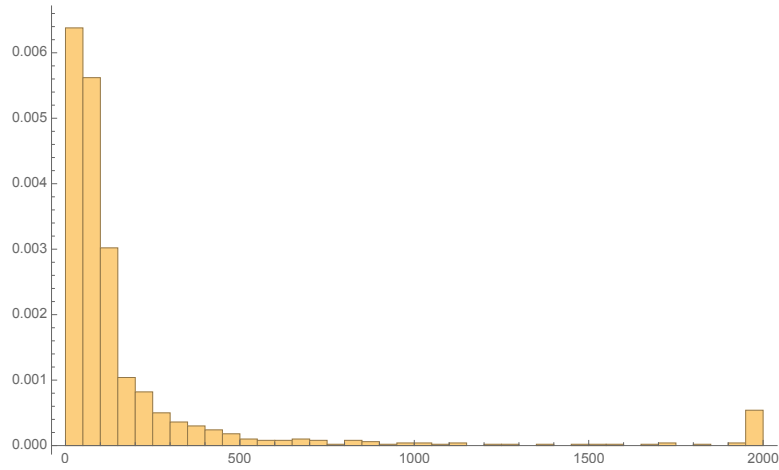
Figure 4.14: Pore Trap histogram showing a long tail distribution for a pore size of 1/10 the width of the trap.
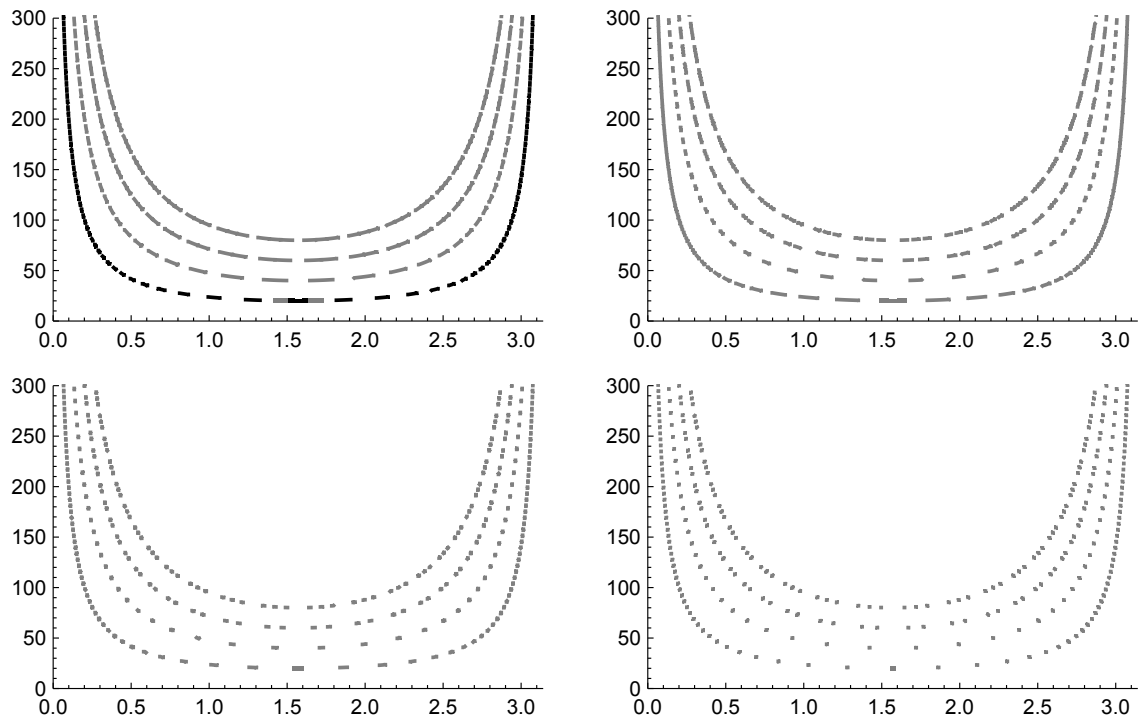
Figure 4.15: Comparison of possible trapping times for pore sizes. $p = 6, 3, 1, 0.1$, clockwise for a trap of width w. The upper-left is equivalent to the simple rectangular trap. The dark black line represents the *actual* trapping time since the pore covers the entire the bottom wall.

ately apparent from examing the traps that the trajectories have similar geometric characteristics to the pore trap with the sequence of discrete trapping times.
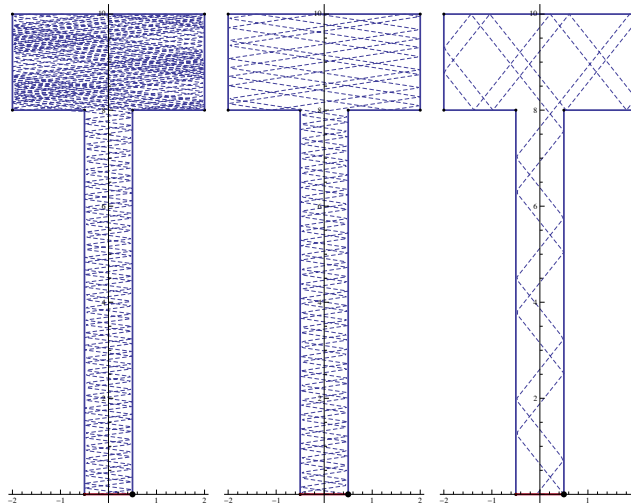
Figure 4.16: Example trajectories in T-shaped traps.

Since the geometry of the traps consists of rectangular regions only, we have the same relationship between input and output angles as with the simple rectangular trap, namely the angles are again perfectly correlated as shown in (Fig. 4.17). However the function $T(\alpha)$ has already become much more complicated as shown in (Fig. 4.17). The simple addition of another rectangle to the trap has scattered and complexified the correlation betweeen α and T. Notice the large segment of angles that enter and exit the trap in minimum time when $\alpha \sim \pi/2$. The long neck of the trap ensures that a wider range of input angles entering in the vertical direction stay vertical because they have more opportunities to preserve their angle on the trajectory of the long neck. Similarly grazing angles *stay* grazing angles in the neck and contribute heavily to the long tail of (Fig. 4.18). We again see that the preponderance of particles exit the trap in $T < 100$ however there are significant numbers of particles in the long tail. A numerical calculation of the c.d.f for the

61

histogram data in (Fig. 4.18) shows 79% of particles have left the trap in time $T < 100$.
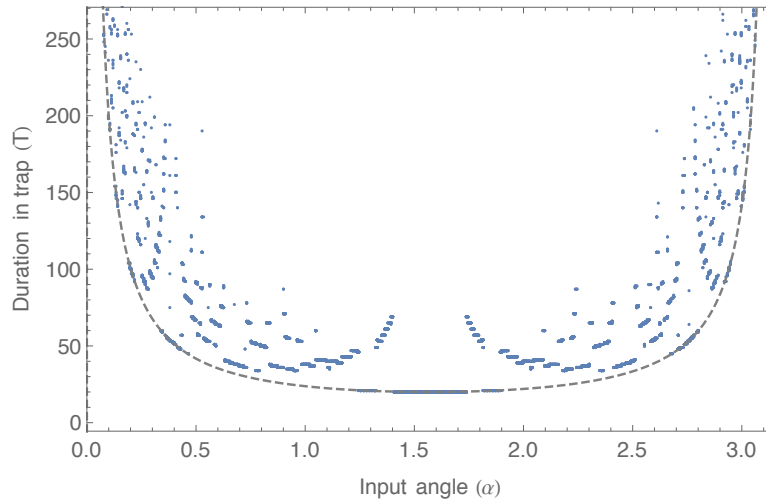
Figure 4.17: Duration T in the rectangular trap sorted by input angle α. The dashed line is the theoretical curve for the simple rectangular trap which ostensibly acts as a lower limit for the T-shaped trap.
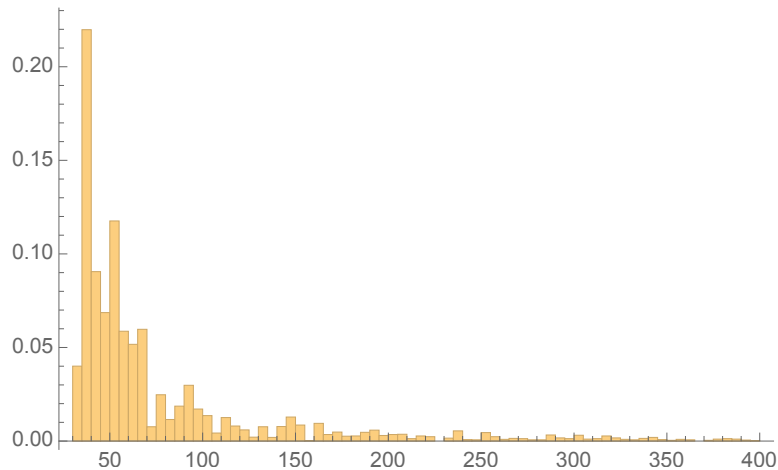
Figure 4.18: The probability histogram of the trapping times T for the T-shaped trap.

Figure 4.19 shows a quantile plot comparison of the distribution of output angles α' compared to a uniform distribution of input angles. We can see that the exit angles also form a uniform distribution. This is to be expected since the rectangular walls of the trap are only capable of reflecting the input angle like $\alpha \mapsto \pm\alpha$. This will be
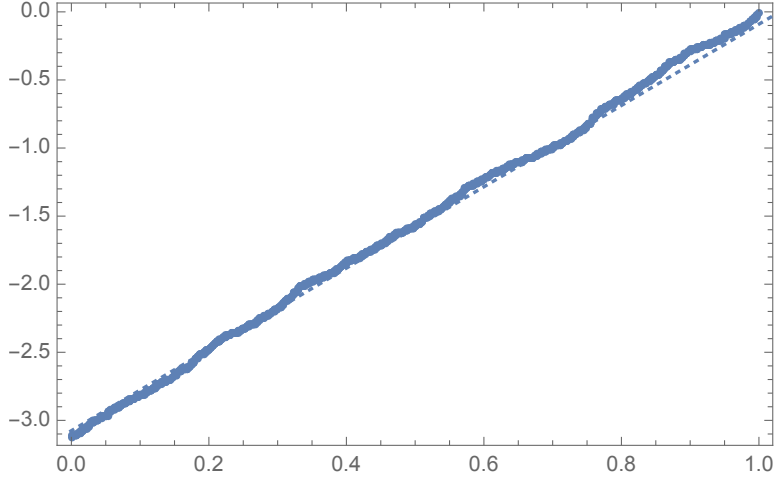
Figure 4.19: Quantile plot of the exit angles α' compared to a uniform distribution (dashed line).

the case for all traps that consist of sections of rectangles since specular reflection

$$\alpha' = 2(n \cdot \alpha)n - \alpha$$

where α is the incident vector and n is the surface normal will only generate new angles from the dot product of the angle with the surface normal. Indeed for any geometry consisting of a regular polygons with s total number of distinct normal vectors the s-fold symmetry will produce s-copies of a uniform distribution of input angles which again is a uniform distribution. For a trap with no symmetry the distribution of output angles will depend on the distribution of normal vectors of all surfaces in the trap.

4.4.3   Irregular Spine-Shaped Traps

Next we simulated traps with less geometrically regular, more biologically-inspired geometry and in particular we took inspiration from the research done on anomalous diffusion in dendritic spines. Dendritic spines are small protrusions from the dendrite of a neuron. They stereotypically have "mushroom", "stubby", or "thin" shaped appearance typically with with a bulbuous head attached to the dendrite by a thin

63

neck. The spine heads can form a synapses with adjacent axons to typically receive input from other nerve cells. They are well known to be pleomorphic with a dynamic morphology, changing their shape and number on the time scale of seconds to minutes and forming and degrading synapses with adjacent neurons to facilitate the formation of memories and learned behaviors.[54] More relevant to anomalous diffusion, dendritic spines have been implicated in causing anomalous diffusion in Purkinje cells [55] and have been modeled with the "spiny" fractional cable equation.[53]
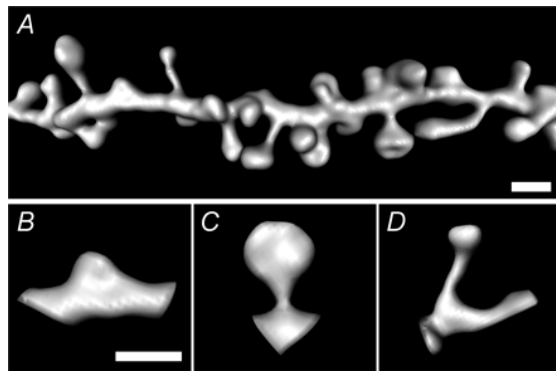
Figure 4.20: Figure 1.Diversity of spine shape A, three-dimensional tertiary portion of the dendritic tree of a CA1 pyramidal cell from a green fluorescent protein-expressing mouse brain. Dendritic spines are classified into three main types: short, stubby spines (< 0.5 m in length) (B), mushroom-type spines, consisting of a short neck and mushroom-shaped head (C), or thin, long spines with an elongated neck and small head (D). Scale bar, 1 m. reproduced from Harris, J Physiol. 2010 Jan 1;588(Pt 1):107-16.
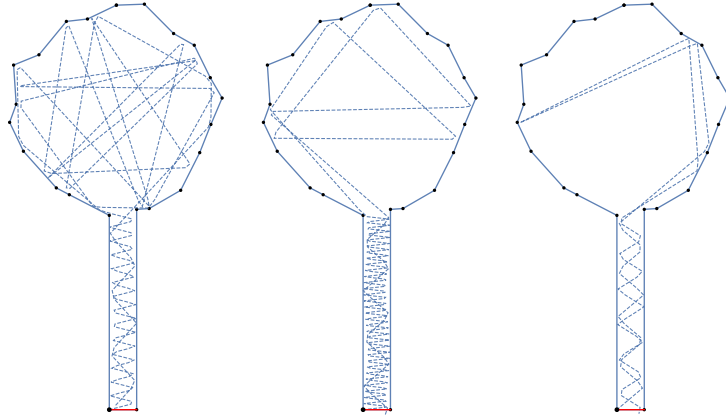
Figure 4.21: Some typical trajectories in the test "spine".

We implemented spine shapes with a thin neck and a spacious head as a test case. A cursory examination of the example runs in Fig. 4.21 shows an immediately apparent dichotomy in the behavior of the trajectories going through the neck compared to the spine head. As we learned with the simple trap, particles that enter the spines in a grazing trajectory stay in the neck for extended times because

$$T(\alpha) \propto \frac{1}{\cos(\alpha)}$$

of the unbounded behavior of the trapping time function. When the grazing angle exits the neck into the comparatively larger, irregular spine head the less regular structure of the boundary walls quickly scatters the angle of the velocity vector of the particle. Eventually the particle re-enters the neck where it may again be subject to a long flight time before it exits the trap.

The addition of the irregular spine head to the simulation has effectively decoupled the entrance angle α from the exit angle α'.(Fig 4.22)

4.4.4 Traps with Inclusions
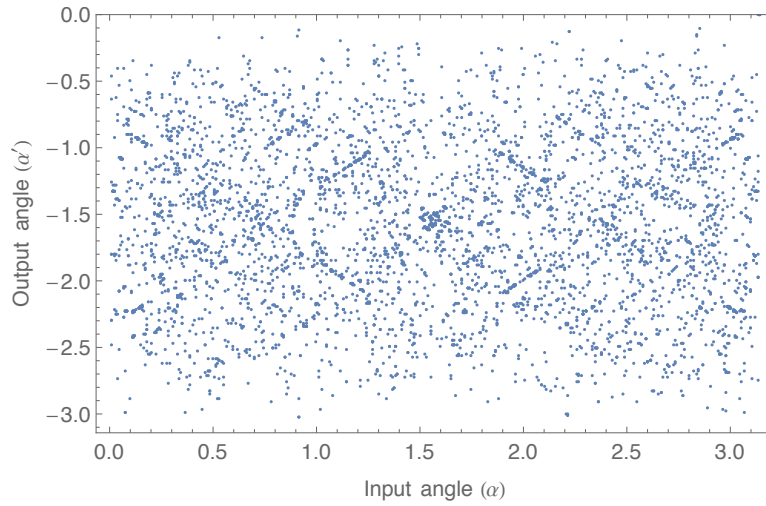
Figure 4.22: α and α' angles have become highly uncorrelated. However the faint presence of the diamond-like pattern of correlated pairs is a reflection of the shape of the spine head which is approximately a regular polygon.
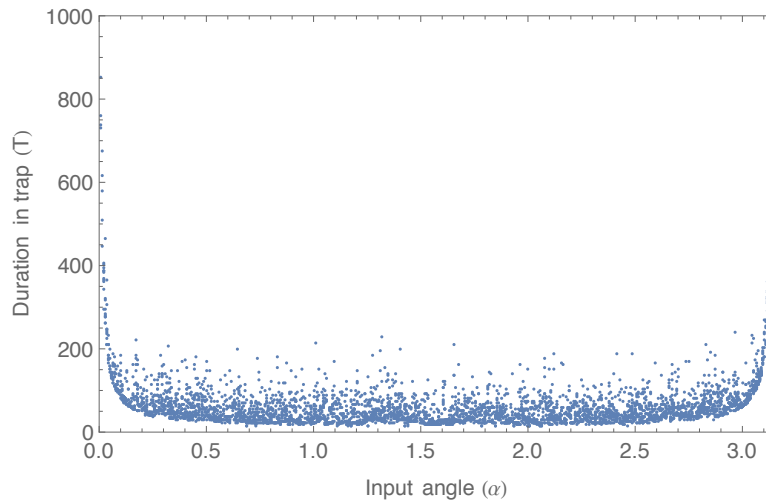
Figure 4.23: The duration time $T(\alpha)$ maintains the spread out "U" shaped appearance which comes from the pore in the spine head. Notice in particular the presense of the long tails for the grazing angles which is indicitive of the long neck.
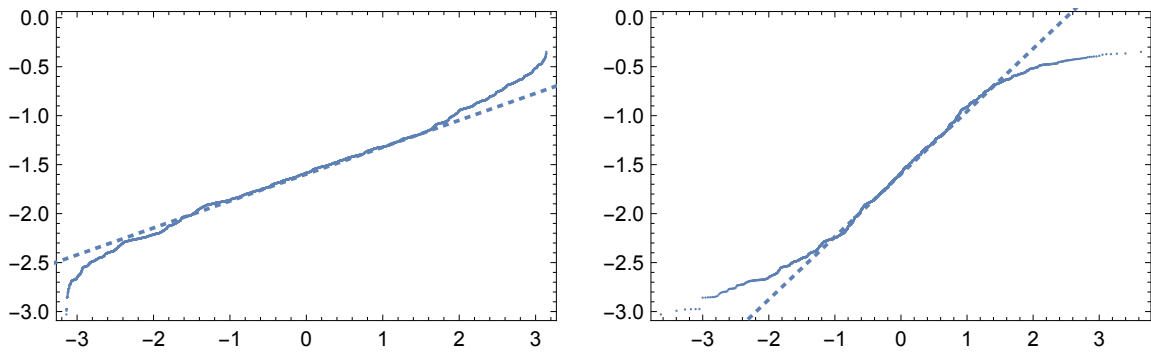
Figure 4.24: Left: quantile plot of exit angles against the uniform input distribution. The presence of the deviations at the extremes of the plot indicate there is a lessened frequency of grazer angles re-entering the trap from the spine head. Right: Quantile plot of exit angles against a standard normal distribution suggest a heavy-tailed distribution with respect of exit angles.
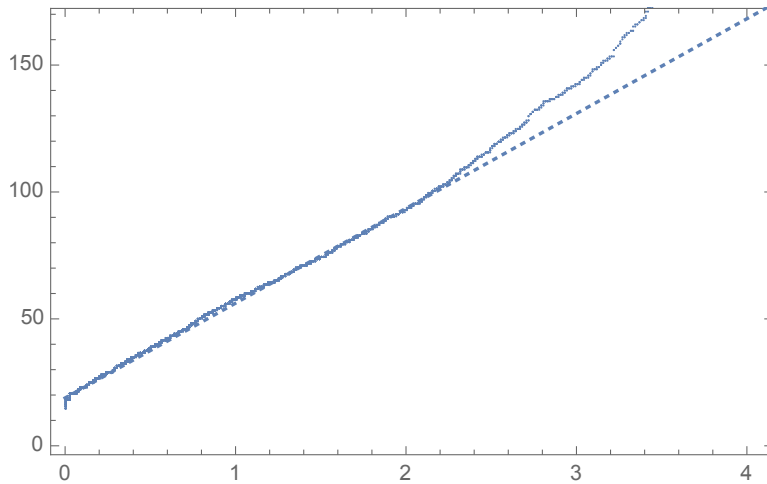
Figure 4.25: Left: quantile plot of trap times against the exponential distribution. The presence of the deviations at the longer times indicate there is an increased frequency of long trap times compared to an exponential distribution. Right: Histogram of the trap times T.
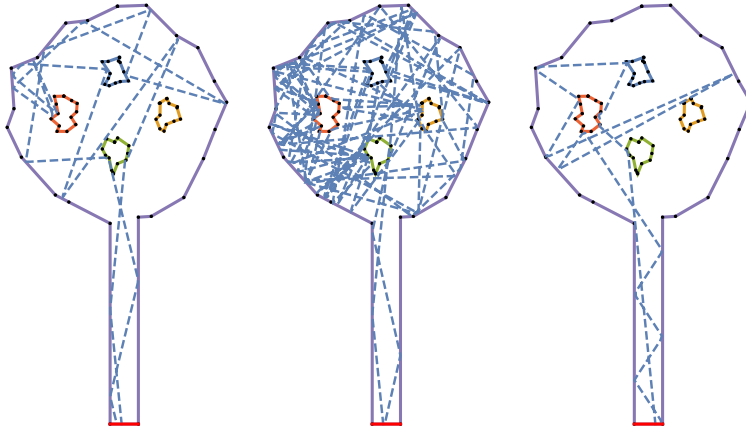
Figure 4.26: Spine heads with internal inclusions.
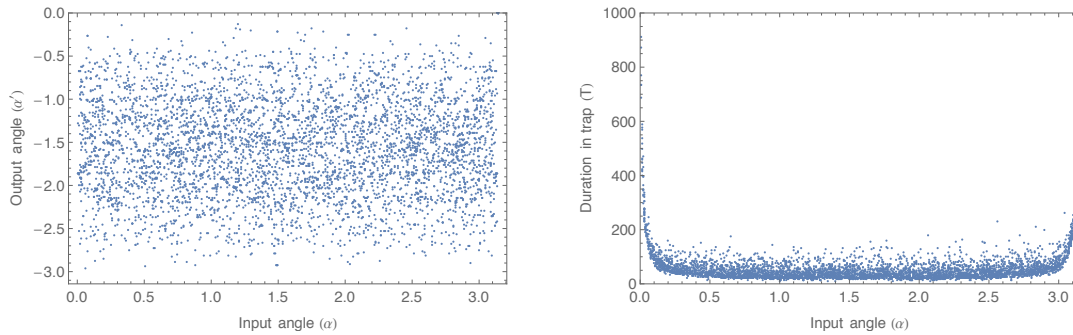
Figure 4.27: $n = 10k$ runs. The inclusions spines demonstrate an equally scattered distribution of output angles and trap times.

4.4.5   Conclusions

The various trapping regions in the previous section were simulated to provide some motivation and justification for using various spatial and temporal distributions in the kinetic model, especially the long-tailed distributions for the trapping times. We saw that the long rectangular necks alone lead to a transformed Cauchy distribution with infinite variance. It is exactly these types of distributions which lead to a blow of up the diffusion matrix in the expansion of the linear Boltzmann equation and the subsequent need for a new method to handle the diffusion limit for the anomalous case.

Irregular heads or walls generate an effective scattering of the input angles from the uniform distribution. The various simulations have usually exhibited long tails in the exiting velocity vectors as well. The means that the simulated traps have tended to damp out the large grazer angles exiting the trap which would have a slowing effect on the effective velocity in the ensembles of particles in the channel. Additionally this would make it less likely that grazers would enter the next encountered trap. However the complex nature of the irregular trap geometry makes it difficult to analyze even in simulations given the multitudinous ways that the geometry can be varied. A possible future direction would be to look at sequences of rectangular traps made up of self-similar copies on smaller spatial scales...fractal like rectangular traps within traps. Since the distribution of angles will always be uniform from orthogonal walls it would be interesting to see if some type of limiting behavior could be deduced from the nested rectangles.

Another interesting problem not considered here would be how a branching angle could effect the trapping distributions. In the cases studied the necks made a right angle with the heads (and indeed in the next set of simulations the neck makes a right angle with the channel). This type of geometry basically converts grazing angles which have the higest effective forward velocity in the channel and traps them for a long time in the narrow channel neck. Similarly the orthogonal angle leaves particles travelling mostly in the vertical direction essentially unscathed as they bounce to the trap ceiling and back down the neck. An angular neck would tend to also trap this class of particles in the neck.

Using what we've learned of the distributions inherent in these simple simulations of 2D trapping geometries we next build a more formal Monte Carlo which reflects the Kinematic Boltzmann model.

Chapter 5

KINEMATIC MODEL AND MONTE CARLO

Next we build on the analysis of trapping regions considered in the previous section and now consider the kinematics of particles flying ballistically in a long channel with trapping regions along the walls (Fig. 5.1). Similar to the trap simulations of the previous chapter we assume the particles collide elastically with the channel boundaries and trap walls and also do not interact with each other. Therefore the speed of the particles remains constant for their sojourn in the channel. In this one-dimensional case however we are only interested in keeping track of the motion of the particle along $x-$axis. It follows from the equations of motion that for a particle moving in the channel with velocity vector v we have

$$\dot{x} = v_x \qquad x \in \mathbb{R}, v \in \mathbb{R}^2 \tag{5.1}$$

$$= ||v|| \cos(\alpha), \qquad \alpha \in [0, \pi] \tag{5.2}$$

where $x(t)$ is the location of the particle on the x-axis at time t. Although the velocity of the particle remains constant we use the two-dimensional velocity vector to determine the angle at which the particle enters the trap (or not) and hence its probability of entering the trap. A particle consequently travels down the channel with constant speed $||v||$ until it reaches the trapping zone shown between the dashed lines in (Fig. 5.1).

5.0.6 *Probability of Entering the Trap*

A particle will enter the trap in some finite time t (which is bound by the time it would take the particle to cross the width of the channel) if the angle α which is
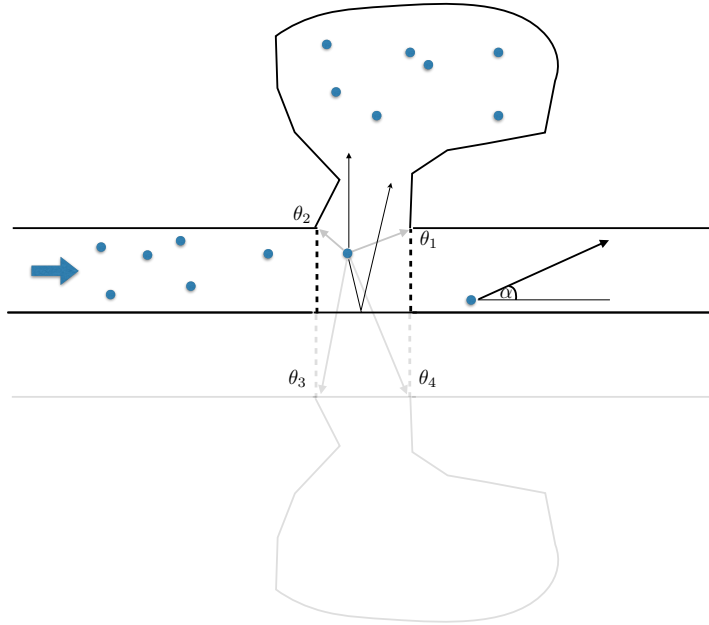
Figure 5.1: Particles flow with constant velocity rightward down the channel. The trapping zone is denoted by dashed lines. A particle (dot) can enter the channel directly or via bouncing on the far wall.

measured from the standard horizontal polar direction lies inside one of two critical angular regions associated with the location of the entrance to the trap. If $\theta_2 > \alpha > \theta_1$ then the particle will enter the trapping region directly. If $\theta_3 > \alpha > \theta_4$ on the other hand the particle will bounce (in the two dimensional sense) against the opposite channel wall and enter the trap in finite time. The mirror-image geometry of the channel is shown in (Fig. 5.1) to aid in visualizing the bounce trajectory and the bottom set of critical angles. The critical angles θ_j depend on the location of the particle in the trapping zone of the channel (Fig. 5.2) whose width is determined by the size of the opening of the trap, or the trap pore, and also the angle α which corresponds to the velocity vecotr v. The y-location of the particle is specified as a fraction of the channel width rw where w is the channel width and $r \in [0, 1]$. Similarly the x-position is a fraction sp of the pore width p where $s \in [0, 1]$. It follows from
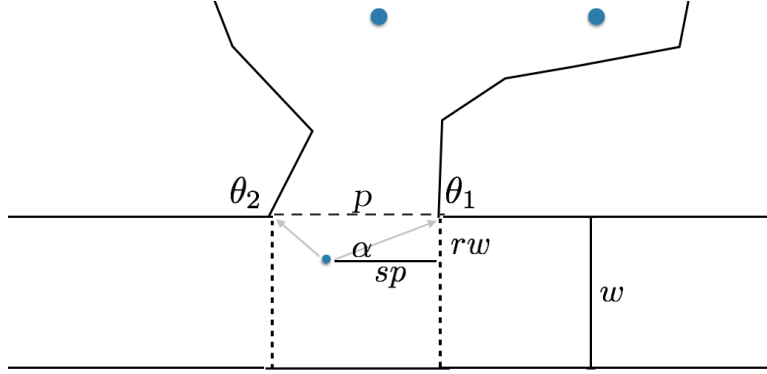
Figure 5.2: The trapping zone: rw is the y-location of the particle specified in fraction of width of the channel, and similarly for the x-location specified in terms of fraction of the pore size of the trap.

the definition of tangent that

$$\tan(\theta_1) = \frac{rw}{sp} \implies \theta_1 = \tan^{-1}(\frac{rw}{sp}) = \tan^{-1}(\lambda\frac{r}{s}) \tag{5.3}$$

where we define $\lambda = \frac{w}{p}$ as the aspect-ratio of the channel trapping region, namely the channel width to the width of the trap pore. Similarly we can compute the other critical angles:

$$\theta_2 = \pi - \tan^{-1}(\lambda\frac{r}{1-s}) \tag{5.4}$$

$$\theta_3 = \pi + \tan^{-1}(\lambda\frac{2-r}{1-s}) \tag{5.5}$$

$$\theta_4 = 2\pi - \tan^{-1}(\lambda\frac{2-r}{s}) \tag{5.6}$$

Note if $\lambda << 1$ then $w << p$ and we have wide trap mouths compared to the channel width, so we would expect a high probability of trapping events occuring. Similarly for $\lambda >> 1$ we have $p << w$ and consequently the trap pores are small compared to the channel width. We simulate the probability histogram for a trapping event in

73

(Fig. 5.3) for a "trappy" channel ($\lambda = 0.2$), a square channel ($\lambda = 1$) and a channel with small pores ($\lambda = 5$).
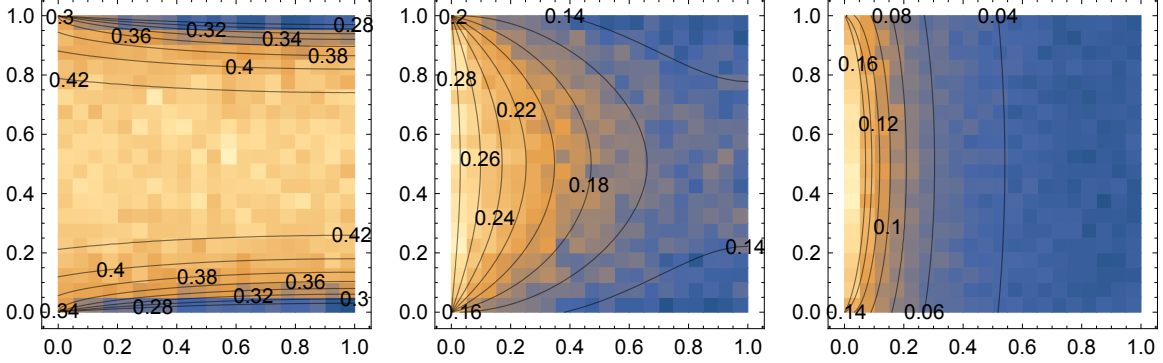
Figure 5.3: Densitiy histograms for $\lambda = 0.2, 1.0$, and 5.0. Darker colors indicate a lower probability to enter the trap for an angle α uniformly chosen on $[0, 2\pi]$. Contours are calculated from the theoretical distribution with level curves representing the probability of a particle at (r, s) entering the trap.

We can also directly compute the probability of entering the trap according to the aspect-ratio λ. Consider the portion of the critical trapping angle traced out between angles θ_1 and $\frac{\pi}{2}$. Then the probability that a particle at location (rw, sp) in the trapping zone with angle α will enter the trap is given by

$$\psi_1(\lambda) = Pr(\theta_1 < \alpha < \frac{\pi}{2}) \tag{5.7}$$

$$= \int_0^1 \int_0^1 \int_0^{\frac{\pi}{2}} \frac{2}{\pi} \left(\arctan(\lambda \frac{r}{s}) < \alpha \right)_\chi \, d\alpha \, dr \, ds. \tag{5.8}$$

$$= \int_0^1 \int_0^1 \frac{\pi - 2 \tan^{-1}(\frac{\lambda r}{s})}{\pi} \, dr \, ds. \tag{5.9}$$

$$= \frac{2\lambda \left(\lambda \log(\lambda) - 2 \tan^{-1}(\lambda) + \pi \right) - (\lambda^2 - 1) \log \left(\lambda^2 + 1 \right)}{2\pi\lambda} \tag{5.10}$$

where χ is the indicator function equal to 1 when the condition is true and 0 otherwise.

We can see that $\psi(\lambda)$ is a monotonically decreasing function of λ. Consider

$$\phi_1'(\lambda) = \frac{\lambda^2 \log \left(\lambda^2 \right) - (\lambda^2 + 1) \log \left(\lambda^2 + 1 \right)}{2\pi\lambda^2} \tag{5.11}$$

$$\phi'(\lambda) < 0 \implies \lambda^2 \log\left(\lambda^2\right) < \left(\lambda^2 + 1\right) \log\left(\lambda^2 + 1\right) \tag{5.12}$$

$$\implies \log\left(\frac{\lambda^2}{\lambda^2 + 1}\right) < \frac{1}{\lambda^2} + 1 \tag{5.13}$$

Where the right-hand side of the equality is always > 0 on $\lambda \in [0, \infty)$ and the left-hand side is always < 0 thus proving the assertion that ψ is monotonically decreasing and supporting our earlier intuition that a small aspect-ratio leads to more "trappy" traps. Similar calulations for the other four angles lead to the following similar results with the final total probability function over the whole range of angles $\psi(\lambda)$ given last.

$$(2\pi\lambda)\psi_{bottom}(\lambda) = -\log\left(\lambda^2 + 1\right) + \log\left(4\lambda^2 + 1\right) +$$
$$\lambda\left(\lambda\left(\log\left(\lambda^2 + 1\right) - 4\log\left(\lambda^2 + \frac{1}{4}\right) + 6\log(\lambda)\right) + 4\tan^{-1}(\lambda) - 8\tan^{-1}(2\lambda)\right) + 2\pi\lambda \tag{5.14}$$

$$\psi_{total}(\lambda) = \frac{(1 - 4\lambda^2)\log\left(4\lambda^2 + 1\right) + 4\lambda\left(\lambda\log(4) + 2\lambda\log(\lambda) - 2\tan^{-1}(2\lambda) + \pi\right)}{4\pi\lambda} \tag{5.15}$$

We calculate a few values of $\psi(\lambda)$ in (Table 5.0.7). For the case of the square aspect ratio approximately 35% of the particles flowing in the channel past the trap will enter the trapping region. We also compare the values of ψ and values computed from the trap Monte-Carlo simulation with 300,000 test particles, and list the resulting relative percent error.

5.0.7   Implications for Spiny Dendrites

Since our model can serve as an approximate model for diffusion between the dendrite and dendrite spines it is interesting to consider some speculations of how

the aspect ratio l of the model could influence spine diffusion dynamics by looking at the trapping probabilities. It is also interesting to note that $\psi(\lambda)$ is most sensitive to change for small λ suggesting that certain spine types may be more sensitive to changes in their morphology with respect to diffusion of sequestered molecules. In fact one of the primary functions of dendritic spines is the compartmentilization of biochemical messengers such as Ca^{2+}. [?] Narrowing of the spine neck diameter could immediately serve to restrict diffusion to and from the spine head volume. Harris reports (Table 5.0.7)the following data for adult rat hippocampus neurons for stubby, mushroom and thin spines. We compute the value of λ from the means which suggest an approximately 2-fold difference in the amount of influx to the spine from stubby to thin spines and mushroom spines. In a similar manner we can estimate the probability of a particle being released from the spine head by considering the rectangular "release zone" to be located inside the spine head and the particle being released into the neck. If we take the length of the spine head to correspond to w and the width of the spine neck to correspond to p and $\mu = \frac{w}{p}$ then $\psi(\mu)$ gives the probability of a particle being released from the release zone inside the spine head. The data in Harris gives the total surface area of the spine head. We can compute the proportion of area of the rectangular trapping zone wp to the reported surface area of the spine head as an estimation of the relative probability that a particle will be in the trapping zone of the spine head. Multiplying these ratios by the release probabilities gives us an approximation of the relative probabilty of a particle inside the spine head being released into the neck and hence into the dendrite. We report the relative probability of efflux into the dendrite as $\phi(\mu)$ in Table (5.0.7). It is interesting to note the release dynamics of the mushroom and thin shaped spine are similar in our model which is to say they have approximately equally likely possibilities of a particle being released from the spine head. The stubby shaped spine has a roughly ten-times

76

greater likelihood of emmitting a particle. This suggests that the functional difference between the mushroom and thin spine concerning compartmentilization of molecules like Ca^{2+} is the length of the neck.

λ	$\psi(\lambda)$	simulation	rel. % err
0.1	0.801837	0.8037	0.232404
0.2	0.690702	0.689833	0.125779
1.	0.352213	0.348867	0.950211
2.	0.230093	0.2302	0.0463269
5.	0.121067	0.122167	0.908716
10.	0.0715551	0.0703	1.75405

Table 5.1: Values of $\psi(\lambda)$.

	Stubby	Mushroom	Thin
$\frac{d_n}{s_n}$ (mean$\pm$DS)	$\frac{0.78\pm0.36}{0.32\pm0.13}$	$\frac{0.81\pm0.24}{0.2\pm0.07}$	$\frac{0.62\pm0.26}{0.1\pm0.03}$
λ	2.44	4.05	6.2
$\psi(\lambda)$	0.2	0.14	0.1
μ	1.38	5.35	4.7
$\psi(\mu)$	0.29	0.12	0.13
$\phi(\mu)$	0.09	0.01	0.02

Table 5.2: Ratios of dendrite diameter (d_n) to spine neck diameter (s_n) and calculated values of $\lambda, \psi(\lambda)$.

5.1 The Trap Monte-Carlo

Next we outline the schematic of the Monte-Carlo simulation for kinematic motion in a channel with traps.

1. A particle travels with velocity v along the x-direction with time step Δt until

it encounters a trapping region X_j which spans some small interval of the x-axis corresponding to the *pore size p* of the trap. That is the particle is in the trapping region when $X_j < x < X_{j+p}$ for some index value j.

2. Trapping regions are specified by a probability density in the model, that is traps occur with some distribution along the channel length L.

3. A particle enters the trap with probability $\psi(\alpha; w; p)$ which depends primarily upon the angle α with the channel width w and the pore size p being optional considerations.

4. The particle stays in the trap for a total duration given by $\tau(\alpha)$ which again primarily depends on the entrance angle and also the trap geometry.

5. The particle is released from the trap with a new velocity α' which depends on the trap geometry.

6. An ensemble of particles is sampled at time t with $t_n \leq t < t_{n+1}$ after running the simulation for sufficiently many time steps. The M.S.D. of the ensemble is calculated for several discrete times by t by linearly interpolating between the points $(t_n, x(t_n))$ and $(t_{n+1}, x(t_{n+1}))$

5.1.1   The Ballistic Limit

First we consider the case with no traps. Then a particle with initial angle α moves ballistically with position $x(t)$ given by

$$x(t) = \int_0^t ||v|| \cos(\alpha) \, du \tag{5.16}$$

The mean square displacement (M.S.D.) of an ensemble of particles with initial angles chosen from a uniform distribution on $[0, \pi]$ is then given by

$$\langle x(t)^2 \rangle = \frac{1}{\pi} \int_0^\pi (||v|| \cos(\alpha) t)^2 \, d\alpha \tag{5.17}$$

$$= \frac{(vt)^2}{2} \tag{5.18}$$
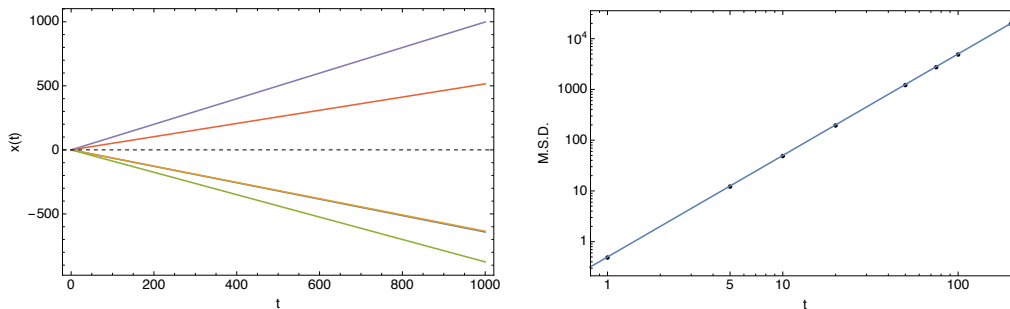
Figure 5.4: Simulation of the model with $v = 1$ and no traps showing ballistic motion only. Right: several typical trajectories. Left: MSD of $n = 5000$ particles for sampled times showing the expected *(solid line)* $\langle x^2 \rangle = \frac{1}{2} t^2$ behavior in a log-log plot.

5.1.2   The Diffusion Limit

Next we consider the case where the density of traps is sufficiently high such that the particle is trapped at every-time step Δt. Since the speed of a particle in the trap is constant the maximum distance it can travel is the direction parallel with the x-axis or $\Delta x_{max} = \pm ||v|| \Delta t$. Therefore it is sufficient in the simulation to set the trapping region to a width of $||v|| \Delta t$ and set the probability of trapping $\psi \equiv 1$. That is particle is trapped for every time step of the simulation. Secondly we set the trap soujourn travel time $\tau \equiv \Delta t$. This means that although the particle is captured by the trap it is only held for one time-step of the simulation. The exit angle α' is chosen from a uniform distributions on $[\pi, 2\pi]$. All together the picture we have is of a particle entering a trap at each time step and being randomly scattered along a new velocity vector at the next time step. This reduces the Kinematic Model to the

79

random walk of (Section 3.1.3). Indeed let $u(x, t)$ be the probability density that the particle is at x at time t. Then

$$u(x, t + \Delta t) = \frac{1}{2\pi} \int_0^{2\pi} u(x + ||v|| \cos(\alpha)\Delta x, t) \, d\alpha \quad (5.19)$$

$$(5.20)$$

is the sum over the probabilities that the particle jumps a distance $||v|| \cos(\alpha)$ in the next time-step. Expanding the r.h.s. in a Taylor series w.r.t. Δx we have

$$= \frac{1}{2\pi} \int_0^{2\pi} u(x) + \cos(a)u'(x)\Delta x + \frac{1}{2}\cos^2(a)u''(x)\Delta x^2 + \frac{1}{6}\cos^3(a)u^{(3)}(x)\Delta x^3 + O\left(\Delta x^4\right) \, d\Delta x$$

$$(5.21)$$

$$= u(x, t) + \frac{1}{4}v^2 u''(x, t)\Delta x^2 + O\left(\Delta x^4\right) \quad (5.22)$$

where the odd powers of $\cos(\alpha)$ integrate to zero. Then

$$\frac{u(x, t + \Delta t) - u(x, t)}{\Delta t} = \frac{1}{4} \frac{u''(x)||v||^2 \Delta x^2 + O(\Delta x)^4}{\Delta t} \quad (5.23)$$

The mean displacement of the particles in one time-step is given by

$$\int_0^{2\pi} ||v|| \cos(\alpha)\Delta x \, d\alpha = 0 \quad (5.24)$$

and the variance of the displacement is

$$\int_0^{2\pi} \frac{||v||(\cos\alpha)\Delta x^2}{2\pi} \, d\alpha = \frac{\Delta x^2 ||v||^2}{2} \quad (5.25)$$

In the interval $[0, t]$ where we make $\frac{t}{\Delta t}$ time-steps, the variance of the displacement is

$$\frac{\Delta x^2 ||v||^2}{2} \frac{t}{\Delta t} = \frac{||v||^2 t}{2} \frac{\Delta x^2}{\Delta t} \quad (5.26)$$

Since $\Delta x^2 \le ||v||^2 \Delta t^2 \le \infty$ the variance of the process is bounded. Taking the limits $\Delta x, \Delta t \to 0$ we recover the diffusion equation from Eq. 5.23.

$$\frac{\partial u(x,t)}{\partial t} = D u_{xx}(u,t) \tag{5.27}$$

where $D = \frac{||v||^2}{4} \frac{\Delta x^2}{\Delta t}$ in the limits and the variance of the random process is then $\langle x^2 \rangle = 2Dt$ as expected. We also recover the Einstein diffusion relationship between D and velocity, $\langle x^2 \rangle = \frac{1}{2}||v||^2 t$.
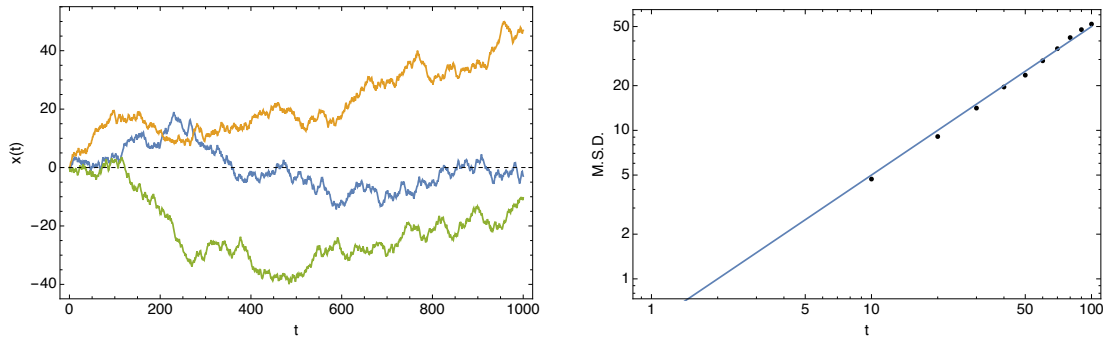
Figure 5.5: Simulation of the model with full traps showing normal diffusion. Right: typical trajectories. Left: MSD of $n = 5000$ particles showing the expected *(solid line)* $\langle x^2 \rangle = \frac{1}{2}t$ behavior in a log-log plot.

5.1.3 Anomalous Sub-Diffusion

For the next case we consider what happens when the particle stays in the trap for a time $t \geq \Delta t$. Considering the results of Chapter Three we know that for a trap with sufficiently irregular geometry or indeed for a trap with a spine-like shape the entrance angle α is effectively decoupled from the exit angle α' and that the duration a particle spends in the trap $\tau(\alpha)$ has a heavy-tailed distribution which can be approximated by the Mittag-Leffler waiting time distribution (4.14) which is the generalization of the exponential waiting time distribution. We used the algortihm given in (4.16) to generate a histogram of 1,000,000 waiting times from which to sample in the simulation. In particular sets were generated for values of $\alpha = 1.0, 0.7, 0.5$ in particular. Recall that the Fourier- and Laplace- transforms of the spatial jump and

waiting time distributions in CTRW master-equation formulation of normal diffusion have the form

$$\psi(k) = 1 - \sigma^2 k^2 + O(k^4) \tag{5.28}$$

$$\tau(u) = 1 - su + O(u^2) \tag{5.29}$$

$$\tag{5.30}$$

where σ^2 and s are constants.

For anomalous sub-diffusion we consider the same ordinary spatial steps but replace the waiting times with a distribution that exhibits asymptotic power-law decay with respect to the time-step.

$$\tau(\Delta t) \sim \frac{1}{\Delta t^{\alpha+1}}, \qquad \alpha \in (0,1) \tag{5.31}$$

$$\tag{5.32}$$

Then using the following distributions in the master equation and inverting the Fourier-Laplace transforms (3.3.2)

$$\psi(k) = 1 - \sigma^2 k^2 + O(k^4) \tag{5.33}$$

$$\tau(u) = 1 - d_\alpha u^\alpha, \qquad \sigma, d_\alpha const. \tag{5.34}$$

$$\tag{5.35}$$

we find the density

$$W(x,t) = \frac{1}{2\pi} \int e^{-ikx} E_\alpha(-d_\alpha k^2 t^\alpha)\, dk \tag{5.36}$$

$$\sim \frac{1}{t^{\alpha/2}} G_\alpha(x/t^{\alpha/2}) \tag{5.37}$$

82

where E is the Mittag-Leffler function and G plays an analogous role to the normal distribution in the heat-kernal of the standard diffusion equation, but here is of course not a normal distribution. However we can read off the scaling relation of the M.S.D. as

$$< X^2 > \sim (t^{(\alpha/2)})^2 \sim t^\alpha$$

For the distributions used in the simulation we computed the minimum and maximum value along with the mean and variance (Tab. 5.1.3) and percentage of values that are under 10 which was used to gauge the appropriate scale size given the time step and velocity parameters in the simulations. For $\alpha = 1$ the distribution is equivalent to the standard exponential distribution. For $a > 1$ the mean and variance of the distributions become quite large reflecting the unbounded nature of the p.d.f. for those values. However although the distributions include waiting times millions of time as big as Δt the bulk of the waiting times are $< 10\Delta t$. This is to say that the tabulated distributions exhibit the heavy-tails we require.

α	min	max	mean	variance	$\% < 10$
1	1.24673×10^{-6}	13.5146	1.00046	0.998059	0.99996
0.7	3.60581×10^{-9}	2.50228×10^7	281.122	6.268×10^9	0.9223
0.5	2.74617×10^{-10}	7.47845×10^8	13020.3	5.75286×10^{12}	0.87774
0.3	1.60783×10^{-20}	1.15×10^{15}	3.27761×10^{10}	2.4219×10^{25}	0.71012

Table 5.3: Min, max, mean and variance of the waiting time distributions used in the simulation. $\% < 10$ is computed from a tally of the distribution.

5.1.4   Infinite Trap Density Limit, Varying α

We first examine the case of infinite trapping density (a trapping event at every time-step) with values of $\alpha = 1.0, 0.7, 0.5$ in the waiting time distribution $\tau(\alpha)$. We

compute $\alpha = 1.0$ as a test case because this is again equivalent to normal diffusion where we scatter with a finite variance at each step of the simulation. In this particular case we choose for simplicity an exit angle from the trap to be drawn from a uniform distribution on $[\pi, 2\pi]$ which is to say the velocity vector may point along the positive or negative x-direction when exiting the trap. We plot the M.S.D. for several values in Fig.(5.6) and compare it to the theorhetical M.S.D. for the ballistic ($\alpha = 2$), diffusive ($\alpha = 1$) and semi-subdiffusive ($\alpha = 1/2$) cases. In particular since we have a constant speed for the particles we can make three interesting computations. Since

$$< X^2(t) > = \frac{1}{2}v^2 t \tag{5.38}$$

$$= 2Dt \tag{5.39}$$

we can compute an *effective* velocity, diffusion and α with respect to the normal diffusive scaling $O(\Delta t)$. That is to say while v, D, α are constants in the diffusion equation we can calculate an effective velocity function for the time scale t^α.

$$v_{eff} = \sqrt{\frac{2\langle X^2 \rangle}{t}} \tag{5.40}$$

$$D_{eff} = \frac{\langle X^2 \rangle}{2t} \tag{5.41}$$

$$\alpha_{eff} = \frac{\log(2\langle X^2 \rangle)}{\log(t)} \tag{5.42}$$

In the test case of normal diffusion we expect $D_{eff} = D, v_{eff} = v, \alpha_{eff} = \alpha$. Indeed we can see from Fig.(5.7) that the computed effective functions are constant.

Next we run the simulation with $\alpha = 0.7$ to demonstrate subdiffusion. Again we have an infinite trap density so the particle is trapped at every time-step. Since the time-step p.d.f exhibits algebraically long tails for $\alpha = 0.7$ and infinite variance we recover anomalous sub-diffusion. Fig.(5.10) and Fig.(5.11). Since the M.S.D. is a power-law of the form $\langle X^2 \rangle \sim t^\alpha$ ploting on a log-log plot allows us to compare the
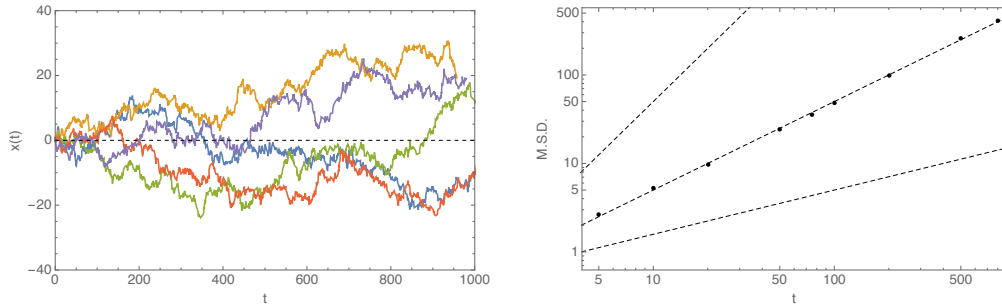
Figure 5.6: Simulation with $v = 1$, $\alpha = 1.0$, $n = 10,000$. left: examples of simulated walks. right: the M.S.D. of the simulation (points). Gray dashed lines are the theoretical plots for the (top to bottom) ballistic case, the diffusive case, and the semi-subdiffusive case ($\alpha = 1/2$).
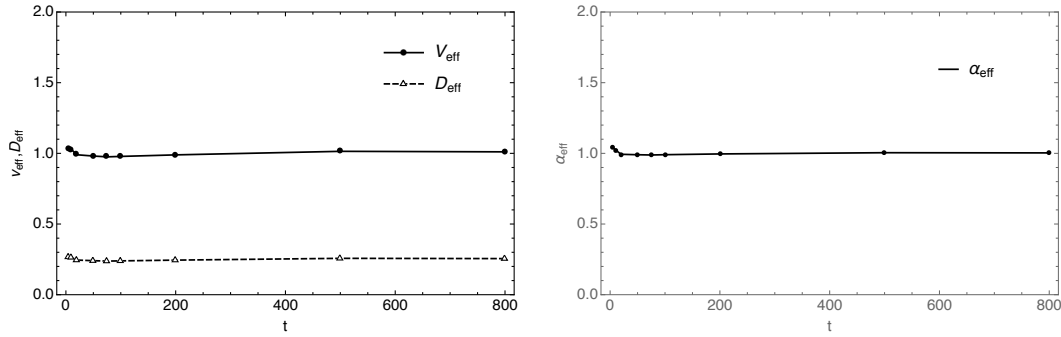
Figure 5.7: Left:The effective diffusion and velocity profiles for the normal diffusive case.Right: The effective α. The mean for $D_{eff} = 0.250, v_{eff} = 1.00, \alpha = 1.00$ as expected.

various cases of *alpha* as lines with slope=α. In the series of figures that follows we plot the ballistic, diffusive, and semi-subdiffusive cases $\frac{1}{2}t^2, \frac{1}{2}t, \frac{1}{2}t^{1/2}$ as a set of dashed gray curves to acts as a guide.

<div align="center">mcr2</div>

Figure 5.8: Simulation with $v = 1$, $\alpha = 0.7$, $n = 10,000$. left: subdiffusive walks with characteristic temporal "flights". right: the M.S.D. of the simulation (points). Gray dashed lines for (top to bottom) ballistic case, diffusive case, and semi-subdiffusive case ($\alpha = 1/2$). Black line is theoretical curve for $\alpha = 0.7$.

Figure 5.9: Case $\alpha = 0.7$. Left: The effective parameters vary with respect to the diffusive time scale. The effective velocity starts at $v_{eff} = 1$ but slows down as the simulation runs. The mean for $D_{eff} = 0.08, v_{eff} = 0.54, \alpha = 0.72$

Finally we present a simulation for $\alpha = 0.5$ which matches the predicted M.S.D. given by $\langle X^2 \rangle = \frac{1}{2}t^{1/2}$.

5.1.5   Discussion

One of the themes that motivates this thesis is to highlight the usefulness of fractional differential equations in modeling biological systems. Figure (5.11) highlights an important observation about the ways we can characterize the flow of particles across various time scales of a modeled system or in an experimental set-up. In the
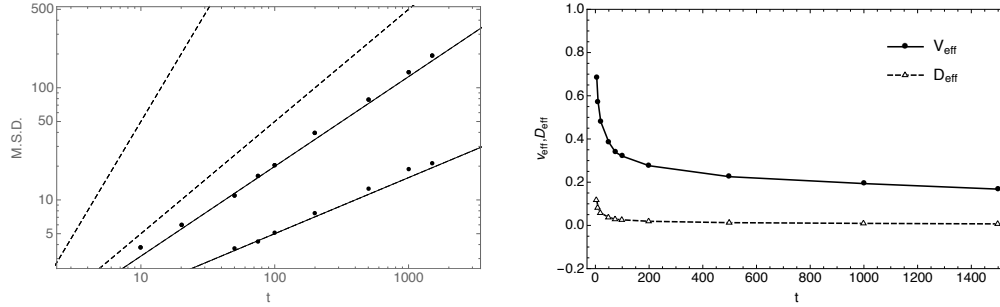
Figure 5.10: Simulation with $v = 1$, $\alpha = 0.5$ and 0.7,$n = 10,000$.Right: effective measurements $\alpha = 0.5$: mean for $D_{eff} = 0.364$, $v_{eff} = 0.04$

case of $\alpha = 1$ we saw that the velocity v and the diffusion parameter D were constants with respect to the diffusive time-scale t, but for the sub-diffusive case we have an effective *slowing* of the velocity (and diffusion) parameters as a function of time. Indeed on the short time scale of the simulation ($t < 100$) the effective velocity (and diffusion parameter) decreases quite rapidly. This highlights some of the difficulties in *measuring* anomalous diffusion in a laboratory setting as we saw in the introduction of the Biological Paradox. Measuring the diffusion "constant" of a process that is undergoing anomalous diffusion can under- or over- estimate the effective diffusion of the system depending on the time frame under which one takes measurements. If the time frame of measurement is too large it will under-estimate the diffusion "constant" on the short time scale and over-estimate the "constant" on the long time scale. As numerical example for the simulation of Fig. (5.11) the average effective diffusion across $0 < t < 2000 = 0.08$ but $D_{eff}(0) = 0.2$ and $D_{eff}(2000) = 0.03$. It is clear how this can be problematic when using diffusion parameters from the literature which are mismatched to the time-scale of a model we may be considering. Given that the effective diffusion decays slowly on large time scales this may be less of a problem for a model mainly interested in steady-state behavior. However considering that diffusion of a signalling species like Ca^{2++} may be happening simultaneously on different time scales such as diffusing into and out of trappy spine heads but also logitudinally

across the dendrite it warrants careful consideration of the parameters we choose for our models.
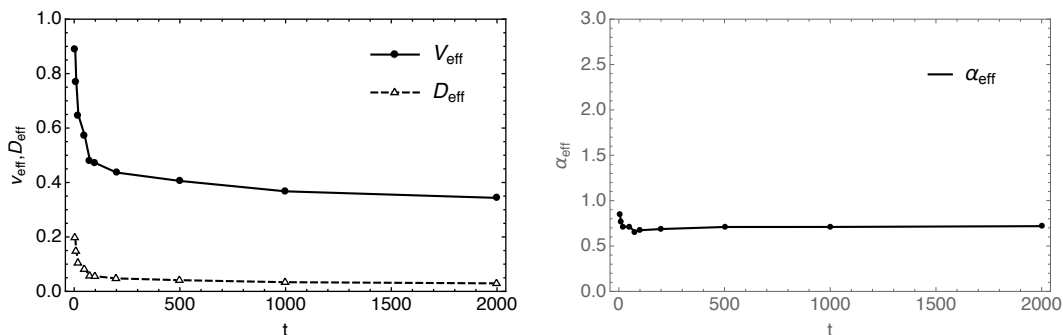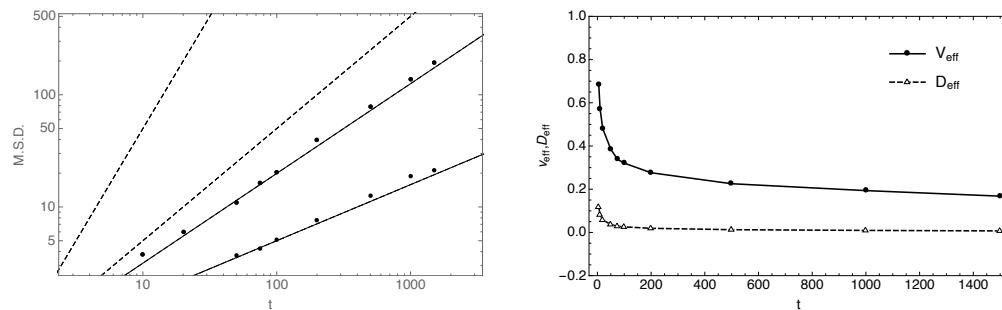

Figure 5.11: Case $\alpha = 0.7$. Left: The effective parameters vary with respect to the diffusive time scale. The effective velocity starts at $v_{eff} = 1$ but slows down as the simulation runs. The mean for $D_{eff} = 0.08, v_{eff} = 0.54, \alpha = 0.72$

More generally given that the case of anomalous diffusion is likely the *typical* case in any system with trapping regions or a percolation-like structure of random obstacles like the organelles and actin/microtubule scaffolding found inside cells, it behooves us to carefully consider how we implement diffusion models or processes inherently based on diffusive principles especially if we are concerned about short-time scales or confined spaces. Of course this obstacle can be overcome by implementing a time-dependent diffusion term in the model of interest but this still begs the question on how one is to measure or estimate such a function from experimental data not to mention the probably analytical complication of adding a time-dependent term to a differential equation. In stark comparison to this situation we can see on the right panel of Fig.(5.11) that the effective α is constant. In essense α is a constant measure of the diffusivity of the process on the diffusive $< X^2 >\sim t$ time-scale. And the fractional diffusion equations related to it are in that sense the "natural" equations to use because they are appropriately scaled for subdiffusion with parameter α in the very definition of the fractional operator. Consider in fact it can be shown that the Riemann-Liouville fractional integral [16] given by

$$_0I_t^\alpha f(t) = \frac{1}{\Gamma(\alpha)} \int_0^t f(t')(t-t')^{\alpha-1}dt', \qquad t > 0$$

can be recast as a Riemann-Stieltjies integral for some fixed t.

$$_0I_t^\alpha f(t) = \int_0^t f(t')d(g_t(t'))$$

where

$$g_t(t') = \frac{1}{\Gamma(\alpha+1)}(t^\alpha - (t-t')^\alpha)$$

has an inherent power-law type scaling property. Indeed for some $k > 0$ we have

$$g_{kt}(kt') = \frac{1}{\Gamma(\alpha+1)}(kt)^\alpha - (kt-kt')^\alpha \qquad (5.43)$$

$$= \frac{1}{\Gamma(\alpha+1)}k^\alpha(t^\alpha - (t-t')^\alpha) \qquad (5.44)$$

$$= k^\alpha g_t(t') \qquad (5.45)$$

5.1.6 Additional Cases

As a conclusion to this section on the Monte-Carlo simulation we briefly consider two additional cases that do not lead to classical anomalous diffusion characterised by a invariant power-law scale. In the first case we vary the spatial density of the traps along the channel. Recall that a channel with no traps behaves in a pure ballistic manner. If we add traps uniformly spaced along the length of the channel at a certain finite density then the ballistic trajectory of the particles will be only occasionally interrupted by a trapping event on the ballistic time scale rather than on the infinitesimal time scale. We can predict that the random walk will ostensibly have a "mountain range" look similar to diffusion random walks on the *ballistic time scale* but will of course not exhibit the scale-invariance property of a Wiener process since the particles are not scattered with infinite frequency. Instead we have something of a pre-limit scenario with a finite scattering frequency. Since the number of scattering

events increases as a function of time we can expect the simulation to exhibit ballistic type behavior on the short time scale $\langle X^2 \rangle \sim t^2$ with increasingly diffusive $\langle X^2 \rangle \sim t$ behavior on the long time scale. Refering to Fig. (5.12) (left) we see the non-
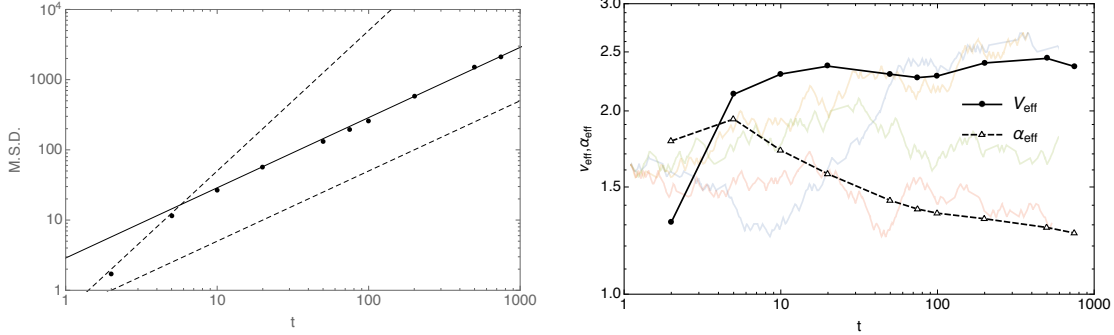
Figure 5.12: Case $\alpha = 1.0$ with trap spacing parameter $= 5$. Right: The MSD profile exhibits ballistic scaling on the short time scale ($t < 10$) transitioning to diffusive behavior on the long time scale ($t > 10$). The dark curve is fitted to a diffusive scaling with an effective velocity of $v_{eff} = 2.32$ computed from the mean v_{eff} in the right figure. Right: v_{eff} and α_{eff} with sample trajectories in the background.

linear behavior of the M.S.D. On the short time-scale the M.S.D. behaves ballistically with $\langle X^2 \rangle \sim t^2$ scaling. As the ensemble of particles encounter more traps their behavior transitions to a diffusive scaling regime with $\langle X^2 \rangle \sim t$ scaling. The offset of the line from the normal diffusive profile (lower dashed line) indicates a greater effective velocity on this log-log plot. The mean effective velocity was computed (mean v_{eff}=2.32) from the simulation run displayed on the right panel dropping the first two points which clearly belong to the ballistic regime. The traps with exponential trapping times have slowed the ballistic trajectories to a *fast diffusion* ($v > 1$) relative to the normal diffusive time scale. We also note that for this non-linear M.S.D. profile the effective α has now become a function of time. We can see from the graph that it indicates a ballistic process transitioning to a diffusive process as α goes from $\alpha = 2$ to $\alpha = 1$ in a linear fashion after the particles enter the trapping region. Several sample trajectories are displaced in the background. On the time scale of the ballistic

flights they resemble a normal diffusion random walk. However it is important to note that they do not exhibit scale invariance. Blowing up the graph on a smaller time would show trajectories with ballistic flights. In Fig.(5.13) we compare two trap spacings. The more widedly spaced traps are not as effective in reducing the overall effective velocity of the ensemble. As a result the mean effective velocity is higher. The transition from ballistic to diffusive regimes is reflected in the inflection points on the right hand graphs at roughtly $t = 10$. More interestingly this is predicted by the intersection of the ensembles M.S.D. with the ballistic M.S.D. Since we are only considering a constant velocity we can predict the critical transition time $\hat{t}$ by solving for when the ballistic curve hits the diffusive limit curve. This corresponds to when the ensemble of particles first encounters the trapping region.

$$\frac{1}{2}(v_{eff})^2 t = \frac{1}{2}v^2 t^2 \tag{5.46}$$

$$\hat{t} = \left(\frac{v_{eff}}{v}\right)^2 \tag{5.47}$$
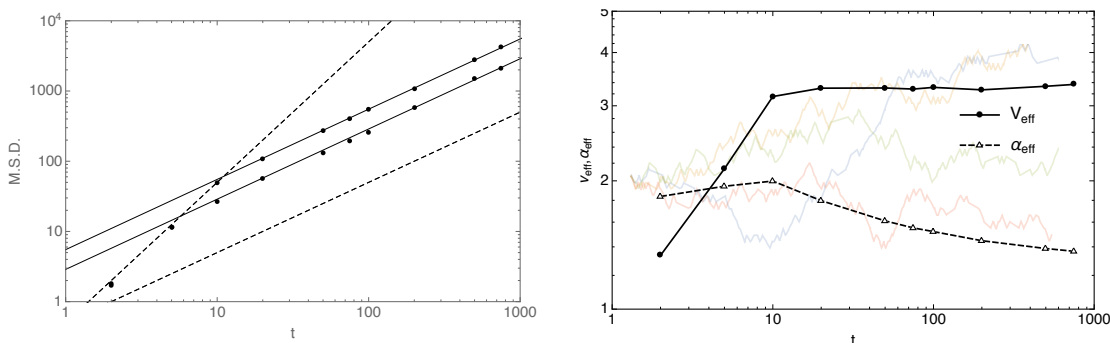
Figure 5.13: Case $\alpha = 1.0$ with trap spacing $= 5$ (lower) and 10 (upper). The wider-spaced traps are not as effective in reducing the effective velocity of the particles. $v_{eff} = 2.32$ for spacing $= 5$ and $v_{eff} = 3.32$ for spacing $= 10$.

Lastly we add the long-tailed trapping time distribution to the spacing $= 10$ trap in Figs. (5.14) and (5.15). In this case we get a slight sub-diffusive behavior in the
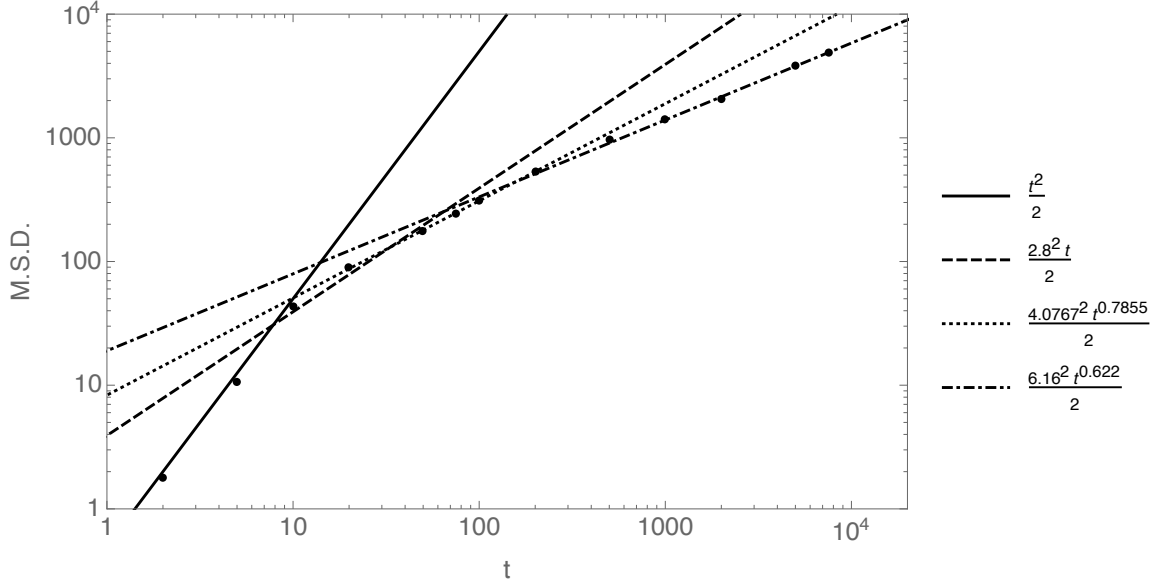
Figure 5.14: Case $\alpha = 0.5$ with trap spacing $= 10$ and a collection of bounding curves fitted to functions of the form $\frac{1}{2}v_e^2 t^\alpha$. Note as α decreases v_e increases.

longer time scale. We calculated a hull of linear curves fitted to the M.S.D. rescaled to the anomalous time scale, namely

$$\langle X^2 \rangle = \frac{1}{2}(v_{\text{eff}})^2 t^\alpha$$

. At the small time scale the behavior of the model is again ballistic – the ensemble of particles have not have sufficient time to encounter traps. As time increases the long-tailed trapping time distribution increases the effective velocity of the particles (measured relative to the diffusive $O(\Delta t)$ time scale) while decreasing the fractional order α.
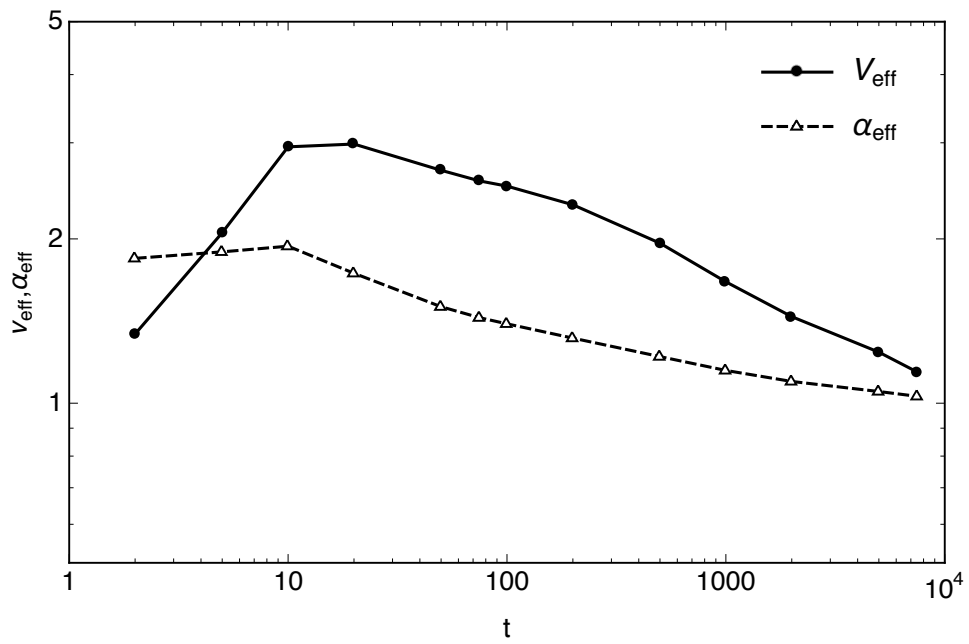
Figure 5.15: For $\alpha = 0.5$ the effective velocity approaches the simulation $v = 1$ velocity.

Chapter 6

THE OPTIMAL HEIGHT OF THE SYNAPTIC CLEFT

One of the general underlying motivations of the current work was to explore ways that the fractional calculus could be used to further develop the types of models available in the neurosciences in particular. Fractional calculus has many interesting mathematical properties for the modeler such as ways to incorporate memory effects, boundary conditions, or non-trivial geometries directly into the formalism of a linear differential equation. In particular it is interesting to consider how the fractional index could be used either as an explicit stand-in for a complicated geometry such as how the fractional cable equation analytically models a spiny dendrite [55] or alternatively how experimental measurements of either the effective diffusion rate or fractional exponent itself can reflect the underlying heterogeneity of the cellular environment. Experimenters who have measured anomalous diffusion both in vivo and in vitro have found a dramatic range of $\alpha \in [0, 1]$ but with typical values in the surveyed literature $\alpha \in [0.5, 1]$. Of particular interest are the in-vitro experiments in [52] who show in controlled in vitro conditions that anomalous diffusion of a tracer particle correlates with the cytoplasmic crowding of macromolecules and in fact decreases monotonically as the concentration of crowding molecules increases.

6.1   Savtchenko and Rusakov Paper

In [64] Savtchenko and Rusakov proposed an interesting optimization problem regarding a elctrophysiological "optimal" height for the synaptic cleft. They report that quite interestingly measurements of the height of the synaptic cleft seems to be remarkably similar varying within the tight range of 15-25nm across a wide variety

94

of species and neuronal morphologies. Moreover the strong structual integrity of the cleft seems to be held stable by a network of intercleft scaffolding. Savtchenko and Rusakov propose the reason for this tight biological constraint is due to an optimal balance between two opposing forces acting on the peak post synaptic current. In the model studied a positive effect on the fast excitatory post-synaptic current (EPSC) is generated by a high rate of activation of the AMPA receptors in the cleft which is considered to be the main contributor to the peak amplitude. When the height of the synaptic cleft δ in the model is decreased the concentration profile of glutamte in the cleft is increased which thereby activates the AMPA receptors more frequently. Contrary to this decreasing the height of the cleft increases the longitudinal resistance of the intercellular medium inside the synaptic cleft. It has been shown that increasing the intracleft resistance effects the local membrane potential of the cell $V(r)$ by causing a significant voltage drop radially across the cleft. In turn this altered voltage profile can effect the receptor current depending on the radial distance of the receptor in the active disk.

The four main equations in the paper involve an expression for the average concentration profile of glutamate in the active zone:

$$C^*(r_a, \delta, t) = \frac{Q}{\pi \delta r_a^2}(1 - exp(-r_a^2/4Dt)) \tag{6.1}$$

the kinetic equations for glutamate activation

$$\frac{\partial [AR]}{\partial t} = -2k_{on}C[AR] + k_{off}[Glu_2AR] \tag{6.2}$$

$$\frac{\partial [Glu_2AR]}{\partial t} = 2k_{on}C[AR] - (k_{off} + \alpha)[Glu_2AR] \tag{6.3}$$

$$+ \beta(1 - [AR] - [Glu_2AR]) \tag{6.4}$$

where C is the average concentration profile in the previous equation. An expression for the radial voltage profile across the cleft

$$V(r) = V_0 \frac{I_0(r/\lambda)}{I_0(L) + L I_1(L) \ln(R/r_a)} \tag{6.5}$$

where L is an expression that depends on the cleft width δ and I_0 and I_1 are modified Bessel functions.

Finally the expression for the synaptic current

$$I_{syn}(t) = V_0 \frac{2\pi\delta}{R_e x} \frac{L(t)}{L(t) ln(R/r_a) + J_0(L(t))/J_1(L(t))} \tag{6.6}$$

where here $L \propto \sqrt{\frac{P_0(t)}{\delta}}$ where $P_0(t)$ is a concentration profile computed from the solution of the kinetic equation which in turn depends on $C^*(t)$. The conclusion of the analyis and also a simulation of the above model paper was that the peak values of I_{syn} are optimized in a range of the cleft height $\delta \approx 12 - 20$ nm for various biologically realistic combinations of parameters in the models such as the size of the apposition zone, the number of AMPA receptors, the number of diffusing glumatate molecules, etc. However the size of the cleft in experimental measurements is reported as $\approx 15 - 25$ nm. The authors conclude that is is likely that the intercleft scaffolding is responsible for the error and that an effective reduced volume does not allow the free diffusion of glutamate.

6.2   Extension with Anomalous Diffusion

We propose to amend the model by introducting a new average concentration based on fractional diffusion in a cylinder. In a way this introduces into the model a new natural parameter α, the index of the fractional-time differential operator. As the fractional index is connected to measures of macromolecular crowding we

propose that a sub-diffusive concentration profile (which will tend to increase the local concentration in the active zone on the short-time scale) offers a natural and physically relevant way to correct the model and additionally offers an interpretation of the extent of the "crowding" in the cleft. Although the one-dimensional diffusion equation is well studied in the literature evident by the review in this thesis extensions to higher dimensional spaces or alternative coordinate systems are less represented. A derivation of inward cylindrical diffusion was considered in [65][66] but we derive the simpler 1-D radially symmetric diffusion needed for the modification of (Eq.6.1).

We consider only diffusion along the radial direction as the height of the synaptic cleft is an order of magnitude smaller compared to the radius. The well-known classical cylindrical diffusion equation is given by

$$\frac{\partial u(r,t)}{\partial t} = D\frac{1}{r}\frac{\partial}{\partial r}\left(r\frac{\partial u}{\partial r}\right) \tag{6.7}$$

and in integral form we have

$$u(r,t) - u(r,0) = D\int_0^t \frac{1}{r}\frac{\partial}{\partial r}\left(r\frac{\partial u(r,\tau)}{\partial r}\right)d\tau \tag{6.8}$$

Following the formalism given in [65] we extend the equation by replacing the integral with the fractional Riemann-Liouville integral. We reviewed the RL-derivative in Section 2.1. In particular we are only interested in considering subdiffusive regimes so we restrict the parameter $\alpha \in (0,1)$ which makes the bounding integer n in the definition to be $n = 1$. Similarly we consider the base-point $a = 0$.

$$_0I_t^\alpha f(t) = \frac{1}{\Gamma(\alpha)}\int_a^t \frac{f(s)ds}{(t-s)^{1-\alpha}} \tag{6.9}$$

Then our modified fractional-diffusion cylindrical equation is

$$u(r,t) - u(r,0) = \frac{D}{\Gamma(\alpha)}\int_0^t \frac{1}{(t-\tau)^{1-\alpha}}\frac{1}{r}\frac{\partial}{\partial r}\left(r\frac{\partial u(r,\tau)}{\partial r}\right)d\tau \tag{6.10}$$

Using the approach employed in the development in Section (3.3) we introduce Fourier-Laplace transform variables

$$\widehat{\eta}(k) = \int_0^{2\pi} d\theta \int_{-\infty}^{\infty} \eta(r) J_0(kr) k \ dk \qquad\qquad \widetilde{\psi}(s) = \int_0^{\infty} e^{st} \psi(t) \ dt \qquad (6.11)$$

where the Fourier transform is the appropriate transform for radially symmetric functions and J_0 is a Bessel function.

Applying the Laplace transform we have

$$\widehat{u(r,s)} - \frac{\widehat{u(r,0)}}{s} = Ds^{-\alpha} \left(\frac{1}{r} \frac{\partial}{\partial r} \left(r \frac{\partial \widehat{u(r,\tau)}}{\partial r} \right) \right) \qquad (6.12)$$

Applying the Fourier transform using the fact given in (??) that

$$\int_0^{2\pi} d\theta \int_{-\infty}^{\infty} \frac{1}{r} \frac{\partial}{\partial r} \left(r \frac{\partial u(r,\tau)}{\partial r} \right) J_0(kr) k \ dk \qquad (6.13)$$

reduces to

$$-2\pi k^2 \widetilde{\widehat{u(k,s)}}$$

we have

$$\widetilde{\widehat{u(r,s)}} - \frac{\widetilde{\widehat{u(r,0)}}}{s} = Ds^{-\alpha} \left(-2\pi \widetilde{\widehat{u(k,s)}} \right) \qquad (6.14)$$

Solving for $\widetilde{\widehat{u(k,s)}}$ we have

$$\widetilde{\widehat{u(k,s)}} = \frac{u_0 s^{-1}}{1 + 2\pi Dk^2 s^{-\alpha}} \qquad (6.15)$$

$$= \frac{u_0 s^{\alpha}}{s(s^{\alpha} + 2\pi Dk^2)} \qquad (6.16)$$

As we saw in Section(3.3) this type of transform has the structure of a Wright function under inversion. Indeed in this particular case using the Laplace transform of the Mittag-Leffler function

$$\frac{s^{\alpha}}{s(s^{\alpha} + a)} = E_{\alpha}(-at^{\alpha})$$

98

we have

$$\widetilde{u(k,t)} = u_0 E_\alpha(-2\pi D k^2 t^\alpha) \tag{6.17}$$

Finally applying the inverse Fourier transform and the delta function initial condition we obtain an expression for the concentration.

$$u(r,t) = \frac{u_0}{\sqrt{2\pi}} \int_0^\infty E_\alpha(-2\pi k^2 t^\alpha) J_0(kr) k \, dk \tag{6.18}$$
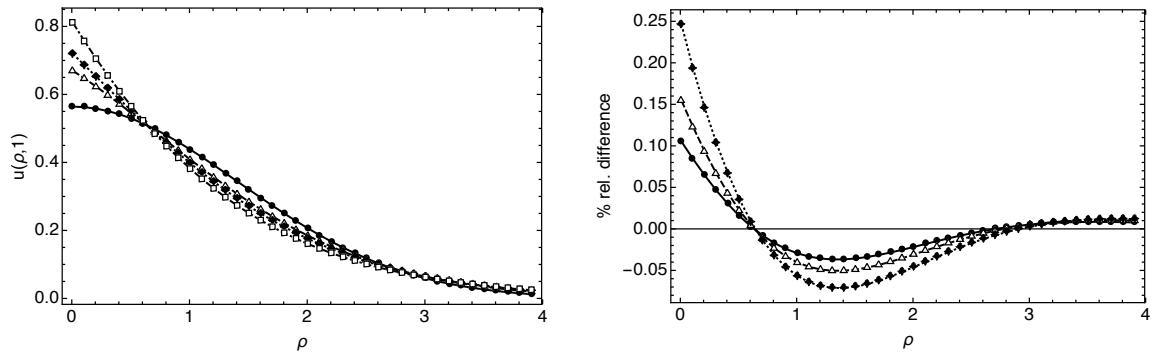
Figure 6.1: Right: $t = 1.0$ diffusive profiles for $\alpha = 0.5, 0.7, 0.8$ and 1.0 Left: relative percent difference between anomalous profiles and normal diffusion.

In Fig (6.1) we compute diffusion profiles for an instantaneous release of particles at the origin plotted at $t = 1.0$ ms to highlight the increased concentration in the vicinity of the origin. Even for a moderatly subdiffusive profile with $a = 0.9$ shows a 5% difference in concentration at the origin and more moderately subdiffusive profiles have significant differences on the order of $10 - 20\%$. As we move radially away from the origin (on the short time scale) the diffusion profile is more strongly dominated by normal diffusion but in the scales of the model and dimension considered by the authors the active zone is concentrated within roughly 25% of the total radius of the synaptic cleft.

Finally we compute the effects the modified diffusion profile has on the model for some various $\alpha's$. The In Fig (6.2) we reproduce curves from the paper. The modified

average concentration profile was numerically integrated and interpolated from

$$u^*(r,t) = \frac{Q}{\pi r_a^2 \delta} \int_0^{r_a} u(r,t) r \, dr \tag{6.19}$$

The response of the model to the modified diffusive profile is shown below.
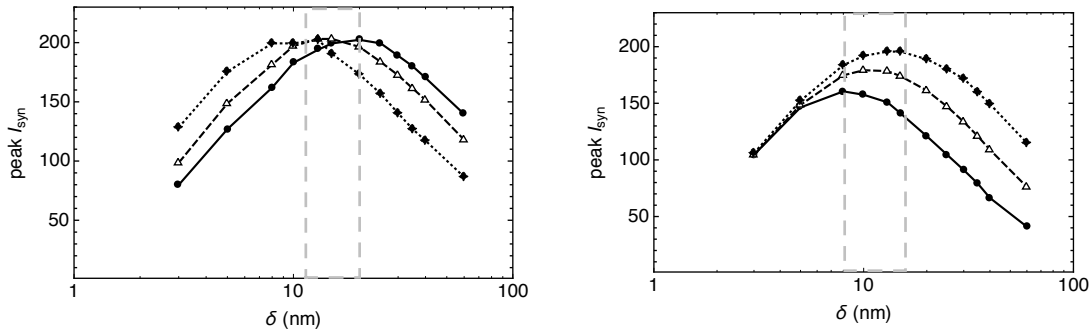
Figure 6.2: Left: peak current for $Q = 3000, 5000, 8000$. Right:$D = 0.2, 0.3, 0.5$. Dashed lines highlight range of cleft heights that contain peak current.

As the anomalous exponent was decreased the peak current tended to shift upward which is consistent with the higher initial concentration in the short time scale shown in the diffusion profiles in Fig(6.1). The rightward shift is consistent with a slower effective diffusion. Overall this shifts the peak EPSC into the physiological region reported in the literature. Given the somewhat arbitrary and ad-hoc way the diffusion profile was added to the model and the linearizations and assumptions of the model

100
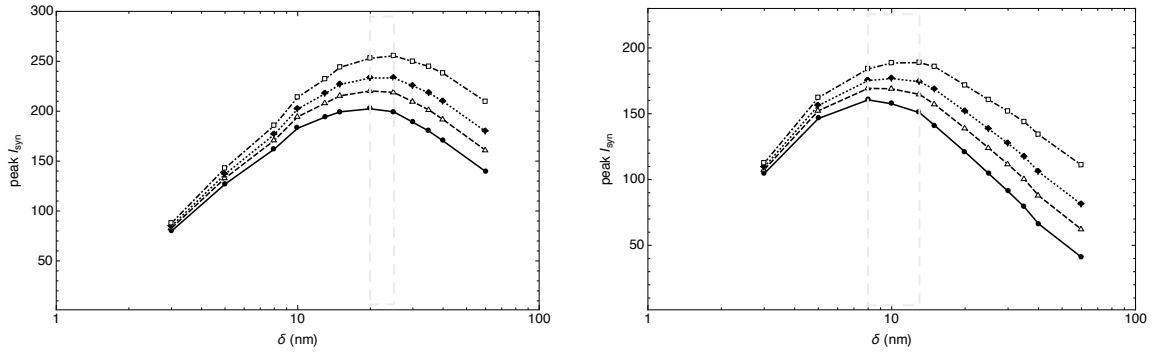
Figure 6.3: Left: peak current for $Q = 3000$ and $\alpha = 1.0, 0.8, 0.7, 0.5$. Right:$D = 0.2$ and $alpha = 1.0, 0.8, 0.7, 0.5$ Dashed lines highlight range of cleft heights that contain peak current.

itself, it is somewhat difficult to interpret exactly what the α stands for physiologically in the sense that $\alpha = 0.5$ is somehow more phyisologically relevant than $\alpha = 0.6$. In a crude sense it is acting as a tuning parameter which adjusts the concentration profile in the desired way. Nevertheless the connection that α has to macromolecular crowding suggests that a more careful model that more directly incorporates the anomalous diffusion profile into the cable equation (or perhaps a stochastic model of the AMPA receptors which could more redily be tied to the probabilistic interpretation of the anomalous exponent) could offer relevant biological predictons such as α gauging the "crowding" or density of cytoskeletal componenets in the cleft.

Chapter 7

OVERVIEW AND FUTURE WORK

Anomalous diffusion and fractional differential equations represent a large and rapidly growing area of research which are at the cross-roads of many different branches of mathematics, physics and biology. In particular much has been written about the mathematical foundations of the fractional calculus or one should say fractional calculi given the multitude of definitions of fractional operators which have been proposed. The Riemann-Liouville, Caputo and Gruenwald-Letnikov definitions are merely the most commonly encountered. Moreover various types of anomalous diffusion equations have been proposed based on these definitions with varying degrees of generality. In somecases the one-dimensional equations have analytically (or computationally) tractable forms in terms of generalizations of the exponential function such as the Mittag-Leffler function and its related Fourier transforms. This allows for insights into the space-time scaling relationships of the fractional exponent and moreover provide forms of the equation which look similar to the well-known diffusion equation. Generally speaking these derivations start from certain assumptions about the underlying probability distributions. In the Montroll-Weiss formulation it is particularly evident how one requires algebraic decay of the time and space probability distributions for the inverse Laplace and Fourier transforms to give a formal operator with the expected characterists of a generalized diffusion equation. One of the points of the thesis was to examine some of the underlying physical assumptions about those probability distributions by modeling various types of trapping geometries and in particular investigating "spine-like" traps in order to show that long-tailed distributions with infinite variance arise naturally from considering ballistic trajectories in these

102

traps. This provides the foundation for an analogous derivation of anomalous diffusion from the kinetic perspective of the Boltzmann equation. Moreover our analysis suggest that α is a more indicitive measure of the underlying kinetics because it does not depend on the scale of measurement. In fact measuring

$$\alpha = \frac{\log(\langle X^2(t) \rangle)}{\log(t)}$$

bears a resemblance to measures of dimensionality such as the Hurst exponent used to measure fractal dimension.

Secondarily we wanted to show a natural example of using fractional differential equations in modeling in the neurosciences. We extended a paper deriving an optimal height for the synaptic cleft and showed how adding the fractional exponent of the anomalous diffusion equation is a natural consideration given that it correlates to a certain density of trapping regions and obstacles in the subcellular environment.

As with any long work especially one at the cross-roads of many diverse fields this thesis has fomented far more questions than answers. In particular it would be interesting to reformulate the model of the synaptic cleft in a form that integrates the fractional kinetics directly into both the receptor kinematic model and also the longitudinal voltage profile. Moreover it would be interesting to incorporate α such that it also had a computable correlation with the density of crowding in the synaptic cleft. In particular it would be beneficial to pursure models where α could be used as a predictor of behavior rather than merely another adjustible parameter. Since diffusion in crowded spaces is the typical case in the cellular environment it would seem this would be a fruitful avenue to pursue generally speaking.

BIBLIOGRAPHY

[1] P. Waage, "Experiments for Determining the Affinity Law", Forhandlinger i Videnskabs-Selskabet i Christiania, (1864) 92.

[2] C.M. Guldberg and P. Waage, "Experiments concerning Chemical Affinity"; German translation by Abegg in Ostwald's Klassiker der Exacten Wissenschaften, no. 104, Wilhelm Engleman, Leipzig, 1899, pp 10-125

[3] Lippincott-Schwartz, Jennifer, and George H. Patterson. "Development and use of fluorescent protein markers in living cells." Science 300.5616 (2003): 87-91.

[4] Massoud, Tarik F., and Sanjiv S. Gambhir. "Molecular imaging in living subjects: seeing fundamental biological processes in a new light." Genes and development 17.5 (2003): 545-580.

[5] Xu, Chris, et al. "Multiphoton fluorescence excitation: new spectral windows for biological nonlinear microscopy." Proceedings of the National Academy of Sciences 93.20 (1996): 10763-10768.

[6] Composition of isolated synaptic boutons reveals the amounts of vesicle trafficking proteins. Benjamin G. Wilhelm, Sunit Mandad, Sven Truckenbrodt, Katharina Krhnert, Christina Schfer, Burkhard Rammner, Seong Joo Koo, Gala A. Claen, Michael Krauss, Volker Haucke, Henning Urlaub, and Silvio O. Rizzoli Science 30 May 2014: 344 (6187), 1023-1028

[7] Weiss, Matthias, et al. "Anomalous subdiffusion is a measure for cytoplasmic crowding in living cells." Biophysical journal 87.5 (2004): 3518-3524.

[8] Banks, Daniel S., and Ccile Fradin. "Anomalous diffusion of proteins due to molecular crowding." Biophysical journal 89.5 (2005): 2960-2971.

[9] Singer SJ, Nicolson GL (Feb 1972). "The fluid mosaic model of the structure of cell membranes". Science 175 (23): 72031

[10] Goldbeter A, Koshland DE (November 1981). "An amplified sensitivity arising from covalent modification in biological systems". Proc. Natl. Acad. Sci. U.S.A. 78 (11): 68404

[11] H.X. Zhou, G. Rivas, and A. P. Minton, "Macromolecular crowding and confinement: biochemical, biophysical, and potential physiological consequences",Annu Rev Biophys. 2008 ; 37: 375397

[12] Heiner, Monika, David Gilbert, and Robin Donaldson. "Petri nets for systems and synthetic biology." Formal methods for computational systems biology. Springer Berlin Heidelberg, 2008. 215-264.

[13] Oldham, Keith B. The fractional calculus. Elsevier, 1974.

[14] Sun, Zhi-zhong, and Xiaonan Wu. "A fully discrete difference scheme for a diffusion-wave system." Applied Numerical Mathematics 56.2 (2006): 193-209.

[15] Hilfer, Rudolf, ed. Applications of fractional calculus in physics. Vol. 5. Singapore: World Scientific, 2000.

[16] Podlubny, Igor. "Geometric and physical interpretation of fractional integration and fractional differentiation." arXiv preprint math/0110241 (2001).

[17] Magin, Richard L. Fractional calculus in bioengineering. Redding: Begell House, 2006.

[18] Allen, Linda JS. An introduction to stochastic processes with applications to biology. Upper Saddle River, NJ: Pearson Education, 2003.

[19] Edelstein-Keshet, Leah. Mathematical Modelling in Biology, McGraw-Hill,1988.

[20] Grima R., Schnell S. (2007). "A systematic investigation of the rate laws valid in intracellular environments.". Biophys. Chem. 124 (1): 110.

[21] Kopelman R. (1988). "Fractal reaction kinetics.". Science 241 (4873): 16201626.

[22] Savageau M.A. (1995). "MichaelisMenten mechanism reconsidered: Implications of fractal kinetics.". J. Theor. Biol. 176 (1): 115124.

[23] Schnell S. and Turner T.E. (2004). "Reaction kinetics in intracellular environments with macromolecular crowding: simulations and rate laws.". Prog. Biophys. Mol. Biol. 85 (2-3): 235260

[24] Kou, S. C., Cherayil, B., Min, W., English, B., and Xie, X. S. (2005a), Single-Molecule MichaelisMenten Equations, Journal of Physical Chemistry B,109, 1906819081.

[25] Tamarat, P., Maali, A., Lounis, B., and Orrit, M. (2000), Ten Years of Single-Molecule Spectroscopy, Journal of Physical Chemistry A, 104, 116.

[26] Stier A, Sackmann E (July 1973). "Spin labels as enzyme substrates. Heterogeneous lipid distribution in liver microsomal membranes". Biochim. Biophys. Acta 311 (3): 4008

[27] Karnovsky MJ, Kleinfeld AM, Hoover RL, Klausner RD (July 1982). "The concept of lipid domains in membranes". J. Cell Biol. 94 (1): 16.

[28] Akihiro Kusumi, Chieko Nakada, Ken Ritchie, Kotono Murase, Kenichi Suzuki, Hideji Murakoshi, Rinshi S. Kasai, Junko Kondo, and Takahiro Fujiwara,Paradigm Shift Of The Plasma Membrane Concept From The Two-Dimensional Continuum Fluid To The Partitioned Fluid: High-Speed Single-Molecule Tracking of Membrane Molecules,Annual Review of Biophysics and Biomolecular StructureVol. 34: 351-378

[29] Xinjian Zhou, Jose M. Moran-Mirabal, Harold G. Craighead and Paul L. McEuen, Supported lipid bilayer/carbon nanotube hybrids.,Nature Nanotechnology 2, 185 - 190 (2007)

[30] Hellriegel, C., Gratton, E. Real-time multi-parameter spectroscopy and localization in three-dimensional single-particle tracking. J R Soc Interface (2009) 6:S3-14.

[31] Brad J. Marsh, David N. Mastronarde, Karolyn F. Buttle, Kathryn E. Howell, and J. Richard McIntosh, Organellar relationships in the Golgi region of the pancreatic beta cell line, HIT-T15, visualized byhigh resolution electron tomography.

[32] Weiss, M., Elsner, M., Kartberg, F. and Nilsson, T. Anomalous subdiffusion is a measure for cytoplasmic crowding in living cells. Biophysical journal (2004).

[33] Fidel Santamaria, Stefan Wils, Erik De Schutter, and George J. Augustine, Anomalous Diffusion in Purkinje Cell Dendrites Caused by Spines, Neuron 52, 635-648, November 22, 2006

[34] J. M. Chambers, C. L. Mallows, and B. W. Stuck, J. Am. Stat. Assoc. 71, 340 (1976).

[35] Sprague, B., R. Pego, et al. Analysis of Binding Reactions by Fluorescence Recovery after Photobleaching. Biophys. J. 2004 Jun; 86(6):3473-3495

[36] Geerts H, de Brabander M, Nuydens R., Nanovid microscopy, Nature. 1991 Jun 27;351(6329):765-6.

[37] Alberts B, Johnson A, Lewis J, et al. (2002). Molecular Biology of the Cell (4th ed.). New York: Garland Science

[38] Kusumi,A., Suzuki,K. and Koyasako,K. Curr. Opin.Cell Biol. 1999,11,582-90

[39] Peters,R. and Cherry, R.J. Proc.Natl.Acad Sci. U.S.A. 1982, 79,4317-21.

[40] Dietrich,C Volonyk,Z.N.Levi,M,et al, Proc.Natl.Acad Sci. U.S.A. 2001, 98, 10642-7

[41] Hegener,O, Prenner, L, et al. Biochemistry 2004, 43, 6190-9

[42] Saffman, P.G. and Delbrueck, M. Proc.Natl.Acad Sci. U.S.A. 1975, 72, 3111-3,

[43] D. Axelrod, D.E. Koppel, J. Schlessinger, E. Elson, and W.W. Webb. Mobility Measurement by Analysis of Fluorescence Photobleaching Recovery Kinetics. Biophys. J. 1976 Sep; 16(9):1055-1069

[44] D M Soumpasis. Theoretical analysis of fluorescence photobleaching recovery experiments. Biophys J. 1983 January; 41(1): 9597.

[45] Saxton, M. J., Jacobson, K. Single-particle tracking: Applications to membrane dynamics. Annual Review of Biophysics and Biomolecular Structure 1997;26(373-399).

[46] Solomon, T. H., Eric R. Weeks, and Harry L. Swinney. "Chaotic advection in a two-dimensional flow: Lvy flights and anomalous diffusion." Physica D: Nonlinear Phenomena 76.1 (1994): 70-84.

[47] Klages, Rainer, Gnter Radons, and Igor M. Sokolov, eds. Anomalous transport: foundations and applications. John Wiley and Sons, 2008.

[48] (Mosteller, F.; Rourke, R. E. K.; and Thomas, G. B. Probability and Statistics. Reading, MA: Addison-Wesley, 1961.)

[49] (Elliott W. Montroll and George H. Weiss (1965). "Random Walks on Lattices. II". J. Math. Phys. 6: 167. doi:10.1063/1.1704269.)

[50] R. Hilfer and L. Anton, Phys. Rev. E 51, R848 (1995).

[51] T. J. Kozubowski and S. T. Rachev, J. Comput. Anal. Appl. 1, 177 (1999).

[52] M. Weiss, M. Elsner, F. Kartberg, and T. Nilsson, Anomalous subdiffusion is a measure for cytoplasmic crowding in living cells, Biophys. J. 87, 3518 (2004).

[53] Langlands, T.A.M., B.I. Henry, and S. L. Wearne. "Fractional cable equation models for anomalous electrodiffusion in nerve cells: infinite domain solutions." Journal of mathematical biology 59.6 (2009): 761-808.

[54] Roberts, T. F., Tschida, K. A., Klein, M. E. and Mooney, R. Rapid spine stabilization and synaptic enhancement at the onset of behavioural learning. Nature 463, 948-952 (2010).

[55] Santamaria, Fidel, et al. "Anomalous diffusion in Purkinje cell dendrites caused by spines." Neuron 52.4 (2006)635-648.

[56] Fujiwara, T. Ritchie, K, Murakoshi, H, Jacobson, K, and Kusumi, A. J. Cell Biol. 2002, 157, 1071-81

[57] Einstein, Albert (1905). ""Über die von der molekularkinetischen Theorie der Wärme geforderte Bewegung von in ruhenden Flüssigkeiten suspendierten Teilchen". Annalen der Physik 17: 549560

[58] R. Klages, G. Radons, and I.M. Sokolov, Anomalous Transport

[59] R. Metzler, J. Klafter, The Random Walker's Guide To Anomalous Diffusion: A Fractional Dynamics Approach, Physics Reports 339 (2000) 1-77

[60] Goenflo R, and Mainardi, F. Cism Lecture Notes

[61] Mainardi F., The fundamental solution of the space-time fractional diffusion equation. Fractional Calculus and Applied Analysis, Vol. 4, No 2 (2001), pp. 153-192

[62] E.W. Montroll and G.H.Weiss, J. Math. Physics, 6,167, (1965)

[63] Brenda L. Bloodgood and Bernardo L. Sabatini, Neuronal Activity Regulates Diffusion Across the Neck of Dendritic Spines, Science 4 November 2005: Vol. 310 no. 5749 pp. 866-869

[64] Savtchenko, Leonid P., and Dmitri A. Rusakov. "The optimal height of the synaptic cleft." Proceedings of the National Academy of Sciences 104.6 (2007): 1823-1828.

[65] Narahari Achar, B. N., and John W. Hanneken. "Fractional radial diffusion in a cylinder." Journal of Molecular Liquids 114.1 (2004): 147-151.

[66] Povstenko, Y. Z. "Fractional radial diffusion in a cylinder." Journal of Molecular Liquids 137.1 (2008): 46-50.